Linear Optical Directional Coupler Modulator

A DISSERTATION

SUBMITTED TO THEFACULTY OF THE GRADUATE SCHOOL

OF THE UNIVERSITY OF MINNESOTA

BY

Jaesang Oh

IN PARTIAL FULFILLMENT OF THE REQUIREMENTS

FOR THE DEGREE OF

DOCTOR OF PHILOSOPHY

Anand Gopinath and James Leger

December, 2010

Acknowledgements

First and foremost, I would like to express my deepest appreciation to my advisor, Dr. Anand Gopinath, for his guidance, constant encouragement and support throughout my Ph.D years. Numerous discussions with him, and his expertise and ideas, have been instrumental in providing proper direction to this study.

It is my pleasure to thank all the members of the MTL staff, especially Mr. Tony Whipple, for their assistance with clean room equipments and useful suggestions during the fabrication of the devices. I would like to thank Dr. Youngseek Cho for his help with and discussion about the designing and simulation of microwave transmission lines. I also would like to thank Dr. Silas Kung for his constant encouragement and support.

I would like to thank my friends, Tahk Yoo, Byeungyeul Ryu, Hongsuk Yang, Kichul Chun, and Hweerin Sohn for all assistance they have given me during my research. My appreciation also goes to my other fellow students in Dr. Gopinath's research group, Dr. Ross Schermer, Dr. Jaewon Kim, Dr. Hyeungsuk Yoo, Dr. Heather Orser, and Sungmin Sohn for their valuable discussion and encouragement.

Finally, I would like to express my deepest gratitude to my parents and parents in low, my brother, my wife, Subin, and my children, Yoonsuh and Yoonsoo, for their love, advice, sacrifice, support, and steadfast faith through the years.

Abstract

The linearization of the response function of the optical directional coupler modulator uses variable coupling along the length of the device, and the coupling function can be synthesized for a desired response function. This synthesis gives rise to coupling functions which have negative coupling regions realized by placing a phase shift in one of the arms of the coupler, and the reversion to the positive coupling requires a second phase shift in one or other arm of the coupler. A linear response modulator was previously designed and fabricated, but obtained large switching voltages, and an alternative trapezoidal response was chosen. A second design using a uniform coupling directional coupler with four π phase shifts to obtain a linear response was considered.

These two linear designs have been investigated, the trapezoidal response's design was synthesized by the Fourier transform technique and the design was refined using the Newton's method. The phase shift design was achieved by four phase shift points, which were chosen very carefully for linear response. The small signal calculations for the second and third order intermediate distortions (IMD2 and IMD3) show Spur Free Dynamic Ranges (SFDR) of the better than 120 dB/Hz$^{2/3}$ for the IMD3 for both designs, and the IMD2 of the order of 105 dB/Hz$^{1/2}$ for the trapezoidal response and better than 120 dB/Hz$^{1/2}$ for the phase shift design. The switching voltage–length product of the trapezoidal response is lower than the phase shift design.

Since the electrical phase velocity in III-V semiconductor coplanar strip electrode structures is higher than the optical phase velocity, a slow-wave electrode structure is required for velocity-matching, and the T-rail shunt capacitive and series inductive loaded coplanar strip was chosen.

These optical directional modulator designs have been fabricated and tested. The intensity responses are different from the design because of fabrication problems including uneven waveguide etching along the device. The linearity measurement was not performed because of the weak optical output from the modulator due to high insertion loss of the modulator. The velocity matched designs cover up to 20 GHz and is limited by the measurement equipment.

Table of Contents

CHAPTER 1 Introduction 1
1.1 Optical Modulators in Analog Optical Link 1
1.2 Overview of the Thesis 3
1.3 References 5
CHAPTER 2 Theory of Directional Coupler Modulators 9
2.1 Coupled Mode Theory 9
2.1.1 Planar step index waveguide structure 9
2.1.2 Perturbation Theory 15
2.1.3 Waveguides in a Directional Coupler 17
2.2 Electrooptic Effect 23
2.2.1 Introduction 23
2.2.2 Index Ellipsoid 23
2.2.3 Pockel's Effect 26
2.2.4 Switching Voltage Calculation 29
2.2.5 Switching Voltage Calculation 30
2.3 Distortion in Nonlinear Optical Modulators 33
2.3.1 Distortion Calculation 34
2.4 Optical Link Model 36
2.4.1 Link Gain and Noise 36
2.5 References 40
CHAPTER 3 Linear Directional Coupler Modulator Design 42
3.1 Introduction 42
3.2 Variable Directional Coupler Modulator 44
3.2.1 Design Theory 45
3.3 Uniform Coupler Modulator with Negative Coupling Regions 59
3.3.1 Proposed Design 59
3.3.2 Design optimization 61
3.4 Linearity Analysis 64
3.4.1 Trapezoidal Response case 67
3.4.2 Uniform directional coupler with negative coupling 68
3.4.3 Triangular Response case 69
3.5 Switching Voltage 71
3.6 Designs for the Variable Phase shifts at Different Locations in the Uniform Coupler Modulator 71
3.6.1 One phase shift in center of the device 72
3.7 References 74
CHAPTER 4 Velocity and Impedance Matching Electrode Structure 76
4.1 Introduction 76
4.2 Theory of Periodic Structure 78
4.3 Calculating Z_c and β of the Periodic Structure from Simulation and Measurement Results 85
4.4 Slow-wave Electrode Structure 87
4.5 References 93

CHAPTER 5 Fabrication of the Linear Directional Coupler Modulators 95
5.1 Introduction 95
5.2 Waveguide Fabrication 96
5.3 Electrode Fabrication 101
5.4 Thinning Wafer 107
5.5 Background Metalization 108
CHAPTER 6 Experiment 110
6.1 Basic Measurement 110
6.1.1 Breakdown Voltage Measurement 110
6.1.2 Loss measurement 112
6.2 RF and DC Measurement 113
6.2.1 Characteristics of the Slow-wave electrode structure Measurement 113
6.2.2 DC Measurement 116
CHAPTER 7 Conclusion and Future Work 124
7.1 Conclusion 124
7.2 Future Work 125
CHAPTER 8 References 127

List of Figures

Figure 2-1: An asymmetric optical slab waveguide. 2-10
Figure 2-2: The geometrical relation between β, κ, and k..... 2-12
Figure 2-3: A symmetric optical slab waveguide 2-14
Figure 2-4: (a) and (b) The refractive index profiles for two individual step index planar waveguides and (c) The refractive index profile for a directional coupler waveguides. 2-17
Figure 2-5: Index ellipsoid which is a three-dimensional ellipse. 2-25
Figure 2-6: x and y axes are the principal axes without applied electric field and x' and y' axes with applied electric field. 2-28
Figure 2-7: The setup of the directional coupler modulator to describe the relation of the principal axes, applied electric field, and polarization of the light. 2-30
Figure 2-8: Fundamental and intermodulation distortion components for two-tone signal 2-33
Figure 2-9: Common form of a fiber optical link 2-35
Figure 3-1: (a) a coupling coefficient and (b) a response function of the conventional uniform directional coupler modulator. The black line is for S(z) and red dashed line is for $|S(z)|^2$ 3-42
Figure 3-1-1: (a) Coupling Coefficient (b) Full Response for the Triangular case. 3-42
Figure 3-2: Schematic diagram of the variable coupling directional coupler electrooptic modulator. Electrodes on each waveguide (not shown) modulate the power output..... 3-44
Figure 3-3: (a) a desired modulator response and (b) its corresponding coupling function obtained through the Fourier transform of the response. The desired response is perfectly linear in the sloped regions, and perfectly flat otherwise..... 3-49
Figure 3-4: The red lines of (a) and (b) are the ideal intensity response function and coupling coefficient and the blue dash lines of (a) and (b) are the initial intensity response function and coupling coefficient 3-53
Figure 3-5: The (a) coupling function and (b) corresponding response function for 100 steps of the iterative Newton's method. Each step improves the fit of the response (solid lines) to the desired response (dotted line) 3-54
Figure 3-6: The perturbation term of the coupling function, *p*, during the iteration 3-54
Figure 3-7: The response functions (a) after 100 iteration (B) of the best fit at slop region..... 3-55
Figure 3-8: The enlarged response functions of 100 iterated response and best fitted response functions 3-55
Figure 3-9: The best fitted version of (a) the variable coupling coefficient (b) the intensity response function..... 3-56
Figure 3-10: (a) Coupling function for the improved modulator design. (b) Response function for the improved modulator design (solid line) and the target response (dotted line) 3-57
Figure 3-11: π phase shift with (a) different length and (b) different width..... 3-58
Figure 3-12: The variable coupling directional coupler with 8 π phase shifts..... 3-59

Figure 3-13: The Coupling coefficient of the directional coupler modulator with four π phase shifts 3-60
Figure 3-14: The directional coupler with four π phase shifts 3-60
Figure 3-15: Intensity response of the phase-shifted directional coupler modulator (solid line), and intensity response of the conventional directional coupler modulator (dashed line) 3-63
Figure 3-16: The two tones SFDR calculation of Mach-Zehnder modulator. P_1 and P_2 are $P_{Input}\big|_{P_{FundamentalSignal}=P_{Noise}}$ and $P_{Input}\big|_{P_{Distortion}=P_{Noise}}$ in equation (3.36) , respectively 3-66
Figure 3-17: (a) Coupling Coefficient (b) Full Response for the Original Trapezoidal case 3-67
Figure 3-18: (a) SFDR for IMD2 and IMD3 (b) SFDR for the Second Harmonic and the Third Harmonic for Trapezoidal Response 3-67
Figure 3-19: (a) Coupling coefficient which changes sign at each pi-phase shifter, otherwise coupling is uniform (b) response for a constant directional coupler with pi-phase shifters along the optical waveguides 3-68
Figure 3-20: (a) SFDR for the harmonics and IMDs along the varied bias voltages and (b) overall SFDR of harmonics and IMDs as functions of the RF input power 3-68
Figure 3-21: (a) Coupling Coefficient (b) Full Response for the Original Trapezoidal case 3-69
Figure 3-22: (a) SFDR for IMD2 and IMD3 (b) SFDR for the Second Harmonic and the Third Harmonic for Triangular Response 3-69
Figure 3-23: The schematic design of the uniform directional coupler modulator with one phase shift section 372
Figure 3-24: (a) Intensity response and (b) the second harmonic, IMD3, and IMD2 with varying the phase from 0° to 45° 3-72
Figure 4-1: The equivalent circuit of a segment of a transmission line with length ΔZ. note that all of R, L, G, and C are distributed components of the line 4-77
Figure 4-2: (a) Equivalent circuit of the transmission line with shunt capacitive loads and (b) its normalized form by Z_0 4-78
Figure 4-3: (a) The equivalent circuit of the unit cell of series inductive and shunt capacitive loads periodic electrode structure and (b) its normalized circuit form 4-82
Figure 4-4: The two port network of the slow-wave electrode structure terminated with input and output impedance 4-85
Figure 4-5: The structure of the electrode with shunt capacitive loads 4-87
Figure 4-6: The equivalent circuit for unit cell of periodic structure 4-88
Figure 4-7: Schematic of CPS with the series inductive load 4-90
Figure 4-8: (a) The slow wave electrode structure with inductive and capacitive loads (b)an enlarged view of a unit cell 4-90
Figure 4-9: An equivalent circuit of the unit cell 4-91
Figure 4-10: The dimension of the designed slow-wave structure 4-92
Figure 5-1: Epitaxial layers used for the fabrication of the optical modulator 5-96

Figure 5-2: Dimension of the Coupler waveguides and coupling gap is about 6μm for the uniform coupler and varied from 2 μm to 10 μm for the variable gap coupler 5-97
Figure 5-3: The steps of the waveguide fabrication 5-98
Figure 5-4: The step after short time wet etching 5-99
Figure 5-5: Rotation of the etching sample during etching 5-100
Figure 5-6: The side view of the waveguide after etching 5-101
Figure 5-7: The seed layer which is not covered entire surface of sample 5-102
Figure 5-8: The liftoff process step of chlorobenzene method and LOR method 5-105
Figure 5-9: The fabrication procedure of the transmission line 5-106
Figure 5-10: The sample wafer attached on the slide glass for thinning 5-108
Figure 5-11: The sample attached on the glass and wrapped by aluminum foil 5-108
Figure 5-12: Fabricated optical directional coupler modulator with slow wave electrode structure 5-109
Figure 6-1: I-V characteristic of Schottky contact for real devices 6-111
Figure 6-2: Cut-back loss measurement 6-112
Figure 6-3: Power loss of waveguide 6-113
Figure 6-4: The schematic diagram of the RF measurement 6-113
Figure 6-5: The RF measurement setting 6-114
Figure 6-6: S-parameters of (a) uniform coupler with phase shifts modulator (b) variable coupling coupler modulator. (1) lines are S11 and (2) lines are S21 6-114
Figure 6-7: (a) Three lines of the calculation, simulation, and measurement for the effective refractive index of the slow wave electrode structure and (b) three lines of the calculation, simulation, and measurement for the characteristic impedance of the slow wave electrode structure for the uniform coupling with phase shifts case 6-115
Figure 6-8: (a) Three lines of the calculation, simulation, and measurement for the effective refractive index of the slow wave electrode structure and (b) three lines of the calculation, simulation, and measurement for the characteristic impedance of the slow wave electrode structure for the variable coupling case 6-115
Figure 6-9: Schematic diagram of the DC measurement of the modulator 6-116
Figure 6-10: DC measurement setting with light source 6-116
Figure 6-11: (a) Two spots represents the mode of input and output waveguides and (b) Output, with the input guide blocked using an iris 6-117
Figure 6-12: The intensity responses of the directional coupler modulators 6-118
Figure 6-13: The frequency response of the uniform coupling with phase shifts modulator 6-119
Figure 6-14: The schematic diagram of the modulation and two-tone test 6-120
Figure 6-15: Measurement setting for the Modulation test 6-121
Figure 6-16: (a) Two signal generator and optical spectrum analyzer, (b) 3dB power combiner 6-121
Figure 6-17: (a) ZRL-2400LN+ LNA and (b) D-30ir Detector receiver 6-122
Figure 6-18: RF spectrum analyzer and the connection with LNA and Receiver 6-122
Figure 6-19: The measured two-tone modulated signal 6-122

List of Tables

Table 2-1: Parameters for calculating voltage and coupler length products. 2-32
Table 2-2: Voltage and coupler length products 2-32
Table 2-3: The frequency components of fundamental signal and distortions using 2D FFT code in Matlab. 2-35
Table 2-4: Fiber-Optic Link Parameters. 2-37
Table 3-1: The fundamental signal and distortion components. 3-64
Table 3-2: Fiber-optic link parameters. 3-66
Table 3-3: Performance of fiber-optic links with parameters of Table 3-1. 3-70
Table 3-4: Voltage and coupler length products. 3-71
Table 5-1: The liftoff procedure of Chlorobenzene method and LOR method. 5-106

CHAPTER 1 Introduction

1.1 Optical Modulators in Analog Optical Link

Fiber optic communication systems comprise of transmitters, optical fiber channel, and receivers. The electrical signal is converted to an optical signal in the transmitter. This converted optical signal is transmitted through optical fiber and converted back to electrical signal at the receiver.

In the transmitter, for the signal conversion, direct modulation of the laser source may be used. Although it is the simplest method to modulate the optical signal, there are several drawbacks when used at high frequency. Direct modulation operates below a few GHz and suffers from spectral broadening. In addition, its bandwidth is limited by laser relaxation oscillation frequency [1-1].

Analog fiber optical links, such as those used in cable television systems, require modulation linearity. In high frequency analog optical systems, external modulators are used, and their linearity is required because nonlinearities in the link lead to signal distortion and limit the dynamic range. The traditional electro-absorption modulator has high insertion loss and spectral broadening [1-2]. The electro-optic Mach-Zehnder modulators [1-3~1-12] have nonlinear responses, which mean that modulation depth has to be kept small, typically in 2 to 5% range. To obtain low insertion loss in the link with this low depth of modulation, optical power needs to be high, 100mW or higher. The electro-absorption modulator may not be able to handle this power level, whereas, the Mach-Zehnder device in lithium niobate, $LiNbO_3$, and III-V semiconductor material could. The electro-optic directional coupler modulator in the same materials should be able to handle this power.

In the last two decades several papers have attempted to improve the linearity of these modulators [1-13~1-19]. However, it is difficult to improve the linearity of the response and increase modulator efficiency simultaneously [1-4].

Recent work has shown that it is possible to implement certain properties of the directional coupler modulator to yield linear response [1-21-1-24]. This has resulted in the development of modulators that are not only considerably more linear than the Mach-Zehnder, but also simple to implement and tolerant to fabrication error [1-13].

The intensity response of the directional coupler modulator is a $(\text{sinc})^2$ function, is also nonlinear [1-20], and is given by

$$\eta(\delta) = \frac{\sin^2(L\kappa\sqrt{1+(\delta/\kappa)^2})}{1+(\delta/\kappa)^2} \ . \qquad (1.1)$$

where η is the intensity of the light from the output waveguide of the coupler, δ is the difference between optical propagation constants of the waveguides, L is the length of the coupling region, and κ is the coupling coefficient.

Traveling-wave type electrodes are required for high frequency operation of external optical modulators to increase the modulation efficiency and bandwidth. It is well known that efficiency and bandwidth of traveling wave electro-optic devices are limited by mismatch of the optical and the electrical phase velocities. The optical phase velocity is constrained by the material indices and the waveguide dimension, which may not be changed. However, the electrical phase velocity may be adjusted for velocity matching. Since the electrical phase velocity of the coplanar strip (CPS) line is larger than the optical phase velocity of optical waveguides in III-V semiconductor structures, a slow wave electrode structure is required for velocity matching.

There are several studies for the slow wave structures, and most of them use the coplanar waveguide(CPW) [1-6] and [1-25~1-28] and all of them use shunt capacitor loading. The paper[1-29] has reported using only series inductive sections in CPW. For the CPS case, there are a few studies for shunt capacitive loaded electrodes [1-30].

There are two methods of designing the slow wave electrode structure: one is to add only extra shunt capacitive loads periodically and the other is to add extra series inductive and shunt capacitive loads simultaneously. In the first case, CPS with higher characteristic impedance greater than 50 Ω should be used because the extra capacitances decrease the characteristic impedance. However, in the second case, the characteristic impedance of the unloaded line in CPS is maintained at 50 Ω, while adding series inductances and shunt capacitances. When inductance and capacitance values are increased by the same ratio, the characteristic impedance of the slow wave structure does not change, but the phase velocity of the electrical signals in the structures reduces. Slow wave electrode structure have been designed and tested with directional coupler modulator.

1.2 Overview of the Thesis

This thesis is organized in four sections: theory, design, fabrication, and measurement of the linear directional coupler modulator.

Chapter 2 begins with basic theory of the directional coupler modulator, which describe the electrooptic effect and coupled mode theory. The optical link model overview which includes link gain and noise is introduced to estimate the linearity of the modulator by calculating the distortion of the intensity response.

Chapter 3 introduces the design methodology of the linear directional coupler modulator. One design is the variable coupling directional coupler modulator which uses inverse Fourier transform technique and Newton's method. The other design is the uniform coupler modulator with negative coupling which is realized by inserting π phase shift sections. The performance of these designed modulators is next compared with other modulators. The magnitude of phase shift may be varied and these are placed at different locations along the uniform directional coupler modulator and the optimum position for linear intensity response are chosen.

Chapter 4 discusses the design of the velocity and impedance matched electrode structure for the III-V directional coupler modulators, for which series inductive and shunt capacitive loads are periodically inserted in the coplanar stripline (CPS).

Chapter 5 describes fabrication procedure of the linear directional coupler modulator with the slow-wave electrode structure. The first two sections discuss the fabrication of the directional coupler waveguides and the last sections for the metallization.

Chapter 6 shows the DC and RF measurement of the optical directional coupler modulator.

Chapter 7 concludes with a summary of the measurement results, and suggestions for future study.

1.3 References

[1-1] K. Kishino, S. Aoki, and Y. Suematsu, "Wavelength variation of 1.6 μm wavelength buried heterostructure GaInAdP/InP lasers due to direct modulation," IEEE J. of Quantum Electronics, vol. QE-18, pp. 343-351, 1982

[1-2] M. Suzuki, H. Tanaka, and S. Akiba, "Effect of hole pile-up at heterointerface on modulation voltage in GaInAsP electroabsorption modulators," Electronics letter, vol.25, no. 2, pp. 88-89, Jan 1989

[1-3] E. I. Ackerman and C. H. Cox, "RF Fiber-Optic Link Performance," *IEEE Microwave Magazine*, vol. 2, pp. 50-58, Dec. 2001.

[1-4] W. B. Bridges and J. H. Schaffner, "Distortion in Linearized Electrooptic Modulators," *IEEE Transactions on Microwave Theory and Techniques*, vol. 43, pp. 2184-2197, Sept. 1995.

[1-5] E. L. Wooten et al, "A Review of Lithium Niobate Modulators for Fiber-Optic Communications Systems," *IEEE Journal of Selected Topics in Quantum Electronics*, vol. 2, pp. 69-82, Jan./Feb. 2000.

[1-6] R. Spickermann and N. Dagli, "Experimental Analysis of Millimeter wave coplanar waveguide slow wave structure on GaAs," IEEE Trans. On Microwave Theory and Techniques, vol. 42, no. 10, pp. 1918-1924, Oct. 1994

[1-7] R. Spickermann, N. Dagli, and M.G. Peters, "GaAs/AlGaAs electrooptic modulator with bandwidth > 40 GHz," Electronics Letters, vol. 31, no. II, pp. 915-916, May 1995

[1-8] N. Dagli, R. Spickermann, S. Sakamoto, and M. Peters, "Ultra wide bandwidth GaAs/AlGaAs electrooptic modulators," 1995 IEEE International Microwave Symposium Digest, pp 251-254, 1995

[1-9] J. C. Cartledge and V. Bouder, "Measurement of alpha-parameter for push-pull operation of π phase shift MQW Mach-Zehnder modulator," Electronics Letters, vol. 37, no. 7, pp. 452-444, May 2001

[1-10] N. Miyazaki, K. Ooizumi, T. Hara, M. Yamada, H. Nagata, T. Sakane, "LiNbO3 optical intensity modulator packaged with monitor photodiode," IEEE photonics Technology Letters, vol. 13, no. 5, pp. 442-444, May 2001

[1-11] B. Enning, "Simple approach to the simulation of the polarization dependence of a LiNbo3 Mach-Zehnder modulator," Journal of Optical Communications, vol.21, no. 5, pp. 162-164, Oct 2000

[1-12] Y. H. Min, J. Mun, C.S. Yoo, K. H. Kim, K. S. Lee, "Mach-Zehnder eletro-optic modulator based on organic-silica sol-gel hybrid films," Electronics Letters, vol. 35, no. 20, pp. 1770-1771, 1999

[1-13] L. M. Johnson and H. V. Roussell, "Reduction of Intermodulation Distortion in Interferometric Optical Modulators," *Optics Letters*, vol. 13, pp. 928-930, 1998.

[1-14] P.-L. Liu, J. Li and Y. S. Trisno, "In Search of a Linear Electrooptic Amplitude Modulator," *IEEE Photonics Technology Letters*, vol. 3pp. 144-146, Feb. 1991.

[1-15] A. Djupsjobacka, "A Linearization Concept for Integrated-Optic Modulators," *IEEE Photonics Technology Letters*, vol. 9, pp. 869-879, Aug. 1992.

[1-16] J. H. Schaffner and W. B. Bridges, " Intermodulation Distortion in High Dynamic Range Microwave Fiber-Optic Links with Linearized Modulators," *IEEE Journal of Lightwave Technology*, vol. 11, pp. 3-6, Jan. 1993.

[1-17] M. L. Farwell, W. S. C. Chang and D. R. Huber, "Increased Linear Dynamic Range by Low-Biasing the Mach-Zehnder Modulator," *IEEE Photonics Technology Letters*, vol. 5, pp. 779-782, July 1993.

[1-18] G. E. Betts, "Linearized Modulator for Suboctave-Bandpass Optical Links," *IEEE Transactions on Microwave Theory and Techniques*, vol. 42, pp. 2642-2649, Dec. 1994.

[1-19] W. K. Burns, "Linearized Optical Modulator with Fifth-Order Correction," *IEEE Journal of Lightwave Technology*, vol. 13, pp. 1724-1727, Aug. 1995.

[1-20] C. Laliew et al, "A Linearized Optical Directional Coupler Modulator at 1.3 μm," *IEEE Journal of Lightwave Technology*, vol. 18, pp. 1244-9, Sept. 2000.

[1-21] M. L. Farwell et al, "An Electrooptic Intensity Modulator with Improved Linearity," *IEEE Photonics Technology Letters*, vol. 3, pp. 792-795, Sept. 1991.

[1-22] R. F. Tavlykaev and R. F. Ramaswamay, "Highly Linear Y-Fed Directional Coupler Modulator with Low Intermodulation Distortion," *IEEE Journal of Lightwave Technology*, vol. 17, pp. 282-291, Feb. 1999.

[1.23] S. A. Hamilton et al, "Comparison of an In-Line Asymmetric Directional Coupler Modulator with Distributed Optical Loss to Other Linearized Electrooptic Modulators," *IEEE Transactions on Microwave Theory and Techniques*, vol. 47, pp. 1184-1193, July 1999.

[1-24] C. Laliew, K. H. Baek and A. Gopinath, “A synthesized electrooptic directional-coupler modulator at 1.3 μm with low switching voltage,” *2002 Conference on Lasers and Electro-Optics Technical Digest*, pp. 42, May 2002.

[1-25] A. Gorur, G. Karpus, and M. Alkan, "Characteristics of periodically loaded CPW structure," *IEEE Microwave Guided Wave Lett,* vol. 8, pp. 278-280, Aug. 1998

[1-26] J. Sor, Y. Oian, and T. Itoh, "Miniature low-loss CPW periodic structures for filter applications," *IEEE Trans. Microwave Theory Tech*, vol. 49, pp. 2336-2341, Dec. 2001

[1-27] Xu Feng, Li Lin, Wu Ke, S. Deoprat, M. Chaker, "Application of FDFD Algorithm Combined with Shift-and-Invert Arnoldi Technique in Bilateral Interdigital Coplanar Waveguide Slow wave Structure," *IEEE MTT-S Int.* 11-16, pp.1025-1028, June, 2006

[1-28] E.H. Bottcher, H. Pfitzenmaier, E Droge and D Bimberg, "Millimetre-wave coplanar waveguide slow wave transmission lines on InP,*" Electron. Lett.*, Vol.32, No.15, pp1377-1378, July 1996

[1-29] Lei Zhu, "Guided-Wave Characteristics of Periodic Coplanar Waveguides With Inductive Loading-Unit-length Transmission Parameters," *IEEE Trans. Microwave Theory & Tech.,* Vol. 51, pp. 2133-2138, Oct.2003

[1-30] Nicolas A.F. Jaeger, Farnoosh Rahmatian, Hiroshi Kato, Robert James, Ezio Berolo, and Zachary K.F. Lee, "Velocity-Matched Electrodes for Compound Semiconductor Traveling-Wave Electrooptic Modulators: Experimental Results," *IEEE Microwave Guided Wave Lett.*, vol. 6, pp. 82-84, Feb.1996

CHAPTER 2 Theory of Directional Coupler Modulators

2.1 Coupled Mode Theory

An optical waveguide coupler has two waveguides in proximity to each other, and experience evanescent optical coupling, which implies that optical energy transfer occurs between the guides [2-5]. The device that uses this property is a directional coupler, and to analyze this structure, coupled mode theory is commonly used.

In coupled mode theory, two parallel waveguides are considered separately [2-1], and optical modes exist independently in each of the waveguides for the incident light of wavelength λ. However, the optical field in one waveguide is affected by that in the other waveguide during propagation and the amplitude and phase of optical field changes along the waveguide length, and this energy transfer is explained by perturbation theory. The coupled mode theory is simple, powerful, and accurate in practical analysis, and is also useful in the analysis of asymmetric directional couplers, and in this chapter, coupled mode theory is discussed.

The coupling phenomenon between optical modes of waveguides in the directional coupler design is essential. Coupled mode theory including perturbation describes the energy exchange, and serves as the primary tool for designing optical couplers, switches and filters.

2.1.1 Planar step index waveguide structure

The simple slab waveguide structure is shown in figure 2-1, where n_g, n_c, and n_s are the refractive indices of the central guiding layer, the upper cladding layer, and the bottom cladding layer, respectively, and h is the guide layer thickness. The waveguide

modes represent the field distributions of the light wave propagation along the guide. The waveguide supports a denumerable number of guided modes, which depend on h and wavelength of the incident light, and an infinite number of radiation modes [2-1].

There are two possible polarizations of the incident light, transverse electric(TE) and transverse magnetic (TM), which depend on the orientation of the electric field. Assume that z axis is the direction of the light propagation, then the orientation of the electric field is y axis for TE case as shown in figure 2-1.

A mode of an optical waveguide is a solution of the wave equations given by[2-1]

$$\nabla^2 E_y + k_0^2 n_i^2 E_y = 0 . \qquad (2.1)$$

where $k_0=\omega^2\mu\varepsilon_0=(2\pi/\lambda)^2$ at a frequency ω and n_i is the refractive index of the guiding or cladding layer depending on the position x. It is assumed that there is no variation of the guide in the y direction, which implies that E_y is independent of y, which gives $dE_y/dy = 0$. The solution of the equation (2.1) assuming that propagation along the z direction is

$$E_y(x,z) = E_y(x)\cdot e^{-j\beta z} . \qquad (2.2)$$

where β is a propagation coefficient along the z direction.

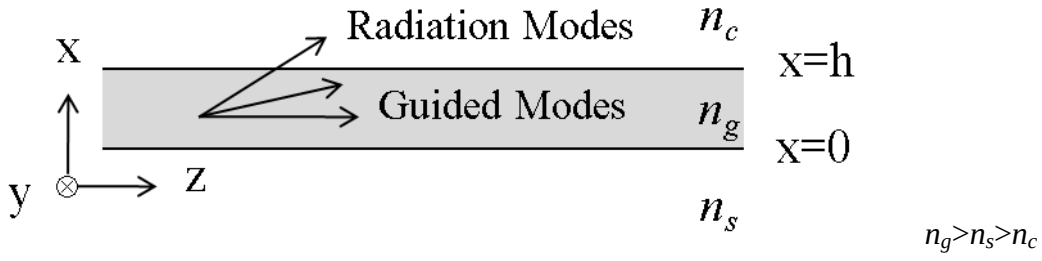

Figure 2-1: An asymmetric optical slab waveguide.

When the equation (2.2) is substituted in the equation (2.1), it becomes;

$$\frac{\partial^2 E_y(x)}{\partial x^2} + \left(k_0^2 n^2 - \beta^2\right) E_y(x) = 0 . \qquad (2.3)$$

The general solutions of equation (2.3) are [2-6]

$$E_y(x) = E_0 \exp\left\{\pm \sqrt{\left(\beta^2 - k_0^2 n_i^2\right)}|x|\right\} \qquad \text{for } \beta > k_0 n_i , \qquad (2.4)$$

$$E_y(x) = E_0 \exp\left\{\pm j\sqrt{\left(k_0^2 n_i^2 - \beta^2\right)}|x|\right\} \qquad \text{for } \beta < k_0 n_i . \qquad (2.5)$$

where E_0 is the amplitude of field at x=0. Equation (2.4) describes the decaying field in the cladding layers. Equation (2.5) describes the propagation form of the light wave in the guide layer. Therefore, the solution can be either propagating or exponentially decaying depending on the value of β.

In case of $\beta > k_0 n_i$, an attenuation coefficient, γ, is defined as

$$\gamma = \sqrt{\beta^2 - k_0^2 n_i^2} . \qquad (2.6)$$

Therefore, equation (2.4) is modified as

$$E_y(x) = E_0 e^{-\gamma x} . \qquad (2.7)$$

In case of $\beta < k_0 n_i$, a transverse wavevector, κ, is defined as

$$\kappa = \sqrt{k_0^2 n_i^2 - \beta^2} . \qquad (2.8)$$

The equation (2.5) is also modified as

$$E_y(x) = E_0 e^{\pm j\kappa x} . \qquad (2.9)$$

From the equation (2.8), the wave-vector, $k = k_0 n_g$, is geometrically related to β and κ as shown in figure 2-2. β and κ are the longitudinal and transverse wave-vectors, respectively, in the guiding layer.

Figure 2-2: The geometrical relation between β, κ, and k.

The longitudinal wave-vector β is defined as the eigenvalue of the mode. For the propagation mode, the value of the β should be between $k_0 n_s$ and $k_0 n_g$. If the value of β is less than $k_0 n_c$, the light radiates because the solutions of the wave equation in all regions are oscillating, or propagating.

To find the values of β, the boundary conditions should be applied to the general solutions calculated from equations (2.4) and (2.5).

$$E_y(x) = Ae^{-\gamma_c(x-h)} \qquad \text{for } x > h, \tag{2.10}$$

$$E_y(x) = B\cos(\kappa_g x) + C\sin(\kappa_g x) \qquad \text{for } 0 < x < h, \tag{2.11}$$

$$E_y(x) = De^{\gamma_s x} \qquad \text{for } x < 0. \tag{2.12}$$

where A, B, C, and D are amplitude coefficients which will be determined by the boundary conditions and continuities, γ_c is the attenuation coefficient in the cladding layer, and κ_g is the transverse wave-vector in the guiding layer.

The equations (2.10~12) are simplified by the boundary condition as follows:

$$E_y(x) = D\left[\cos(\kappa_g h) + \frac{\gamma_s}{\kappa_g}\sin(\kappa_g h)\right]e^{-\gamma_c(x-h)} \quad \text{for } x > h, \tag{2.13}$$

$$E_y(x) = D\left[\cos(\kappa_g x) + \frac{\gamma_s}{\kappa_g}\sin(\kappa_g x)\right] \qquad \text{for } 0 < x < h, \tag{2.14}$$

$$E_y(x) = De^{\gamma_s x} \qquad \text{for } x < 0. \tag{2.15}$$

where D is the amplitude at the $x = 0$. γ_c and κ_g are depend on β, which should be calculated. To find β, the continuity of $\partial E_y / \partial x\big|_{x=h}$ should be applied as follows:

$$\left.\frac{\partial E_y}{\partial x}\right|_{x=h} = -D\left[\cos(\kappa_g h) + \frac{\gamma_s}{\kappa_g}\sin(\kappa_g h)\right]\gamma_c$$

$$= D\left[-\kappa_g \sin(\kappa_g h) + \gamma_s \cos(\kappa_g h)\right]. \tag{2.16}$$

Equation (2.16) is simplified as follows:

$$\tan(\kappa_g h) = \frac{\gamma_s + \gamma_c}{\kappa_g\left[1 - \frac{\gamma_s \gamma_c}{\kappa_g^2}\right]}. \tag{2.17}$$

The equation (2.17) is the eigenvalue equation for β or characteristic equation for the TE modes of a slab waveguide.

The characteristic equation for the TM modes is

$$\tan(\kappa_g h) = \frac{\kappa_g\left[\left(\frac{n_g^2}{n_c^2}\right)\gamma_c + \left(\frac{n_g^2}{n_s^2}\right)\gamma_s\right]}{\kappa_g^2 - \frac{n_g^4}{n_s^2 n_c^2}\gamma_s \gamma_c}. \tag{2.18}$$

To obtain the amplitude coefficient, D, the power carried in the waveguide should be calculated by integrating the z component of the Poynting vector over the cross-sectional area of the guide because A is related to the power.

$$S_z = \frac{1}{2}\mathrm{Re}(E \times H \cdot \hat{z}). \tag{2.19}$$

The average power in a TE modes is

$$P_z = \frac{1}{2}\int_{-\infty}^{\infty} E_y H_x dx = \left(\frac{\beta}{2\omega\mu_0}\right)\int_{-\infty}^{\infty} \left|E_y\right|^2 dx. \tag{2.20}$$

Figure 2-3: A symmetric optical slab waveguide.

The integral has units of power per unit length in the y direction.

For the symmetric case shown in figure 2-3, the general solutions of the field are

$$E_y(x) = A\exp\{-\gamma(x-h/2)\} \qquad \text{for } x \geq h/2, \tag{2.21}$$

$$E_y(x) = A\frac{\cos(\kappa x)}{\cos(\kappa h/2)} \text{ or } A\frac{\sin(\kappa x)}{\sin(\kappa h/2)} \qquad \text{for } -h/2 < x < h/2, \tag{2.22}$$

$$E_y(x) = \pm A\exp\{\gamma(x+h/2)\} \qquad \text{for } -h/2 \geq x. \tag{2.23}$$

where the cosine and sine equations in equation (2.22) are for the even modes and odd modes, respectively.

The characteristic eigenvalue equation for TE modes are

$$\tan(\kappa h/2) = \frac{\gamma}{\kappa} \qquad \text{for even modes,} \tag{2.24}$$

$$= \frac{\kappa}{\gamma} \qquad \text{for odd modes.} \tag{2.25}$$

The characteristic eigenvalue equation for TM modes are

$$\tan(\kappa h/2) = \left(\frac{n_f}{n_s}\right)^2 \frac{\gamma}{\kappa} \qquad \text{for even modes,} \tag{2.26}$$

$$= -\left(\frac{n_s}{n_f}\right)^2 \frac{\kappa}{\gamma} \qquad \text{for odd modes.} \tag{2.27}$$

2.1.2 Perturbation Theory

Perturbation theory is the basic concept of the coupled mode theory [2-1]. If there are no perturbations in the waveguide, the modes will be orthogonal to each other. However, any deviation in waveguide structure perturbs the modes and couples energy between them. The perturbation is described in terms of a distributed polarization source, P_{per}, which represents the deviation of the dielectric polarization .

The electric flux is

$$D = \varepsilon E = \varepsilon_0 E + P \,. \tag{2.28}$$

Any deviation from the normal dielectric constant of a guided wave structure changes P. Therefore, P can be replaced by P_{per}, and equation (2.28) is modified as

$$D = \varepsilon_0 E + P_{per} \,. \tag{2.29}$$

Equation (2.29) is substituted in the wave equation

$$\nabla^2 E_y = \mu\varepsilon \frac{\partial^2 E_y}{\partial t^2} + \mu \frac{\partial^2 P_{per}}{\partial t^2} \,. \tag{2.30}$$

The polarization perturbation now is one of the driving forces. When the possibility of coupling to the continuum of radiation modes is ignored, the total field in the perturbed waveguides are considered as a superposition of confined modes.

$$E(x) = \frac{1}{2}\sum_m A_m^+(z) E_m(x) \exp\{-j(\beta_m z - \omega t)\} + c.c.$$

$$+ \frac{1}{2}\sum_m A_m^-(z) E_m(x) \exp\{j(\beta_m z + \omega t)\} + c.c \,. \tag{2.31}$$

where m indicates the m-th discrete mode, $E_m(x)$ are the spatial amplitude distributions for each mode, and A^+ and A^- are the amplitudes of the forward and backward traveling wave, respectively. Equation (2.31) is substituted into the equation (2.30)

$$\frac{1}{2}\sum_m\left(\frac{\partial^2 A_m^+}{\partial z^2}-2j\beta_m\frac{\partial A_m^+}{\partial z}\right)E_m(x)\exp\{-j(\beta_m z-\omega t)\}+c.c.$$

$$+\frac{1}{2}\sum_m\left(\frac{\partial^2 A_m^-}{\partial z^2}+2j\beta_m\frac{\partial A_m^-}{\partial z}\right)E_m(x)\exp\{j(\beta_m z+\omega t)\}+c.c.$$

$$=\mu\frac{\partial^2}{\partial t^2}P_{per}. \tag{2.32}$$

The effect of the perturbation is to change the amplitudes of the modes in the superposition. If the amplitude is varied slowly by the perturbation, the second derivatives terms are much smaller than the first derivatives terms, $\left|\partial^2 A_m^{\pm}/\partial z^2\right| << \beta_m\left|\partial A_m^{\pm}/\partial z\right|$, and therefore, $\partial^2 A_m^{\pm}/\partial z^2$ is neglected.

The equation (2.32) is simplified as

$$\frac{1}{2}\sum_m\left(-2j\beta_m\frac{\partial A_m^+}{\partial z}\right)E_m(x)\exp\{-j(\beta_m z-\omega t)\}+c.c.$$

$$+\frac{1}{2}\sum_m\left(2j\beta_m\frac{\partial A_m^-}{\partial z}\right)E_m(x)\exp\{j(\beta_m z+\omega t)\}+c.c.$$

$$=\mu\frac{\partial^2}{\partial t^2}P_{per}. \tag{2.33}$$

When $E_n(x)$ multiplies both side of equation (2.33) and integrated over x, the equation (2.33) is simplified by mode orthogonality to obtain:

$$\frac{\partial A_n^-}{\partial z}\exp\{j(\beta_n z+\omega t)\}-\frac{\partial A_n^+}{\partial z}\exp\{-j(\beta_n z-\omega t)\}+c.c.$$

$$=\frac{-j}{2\omega}\frac{\partial^2}{\partial t^2}\int_{-\infty}^{\infty}P_{per}(x,t)\cdot E_n(x)dx. \tag{2.34}$$

where the mode orthogonality is

$$\int_{-\infty}^{\infty} E_i(x)E_j(x)dx = \frac{2\omega\mu}{\beta_i}\delta_{ij}. \qquad (2.35)$$

where δ_{ij} is the Kronecker delta function, which is unity or if $i = j$ or and zero if $i \neq j$.

2.1.3 Waveguides in a Directional Coupler

In the previous section, single waveguide analysis and perturbation theory were introduced. Using these theories, the directional coupler is discussed in this section.

Figure 2-4 shows the refractive indices for each waveguide and the coupled directional waveguides. In the figure 2-4, $n_1(x)$ and $n_2(x)$ are the refractive index profiles of waveguides 1 and 2 in the absence of the other, and $n(x)$ is the refractive index profile of a coupler waveguides. If there is no interaction between two waveguides and the propagation constants of the waveguides 1 and 2 are β_1 and β_2, respectively, each waveguide satisfies equation (2.36) and (2.37), respectively [2-1].

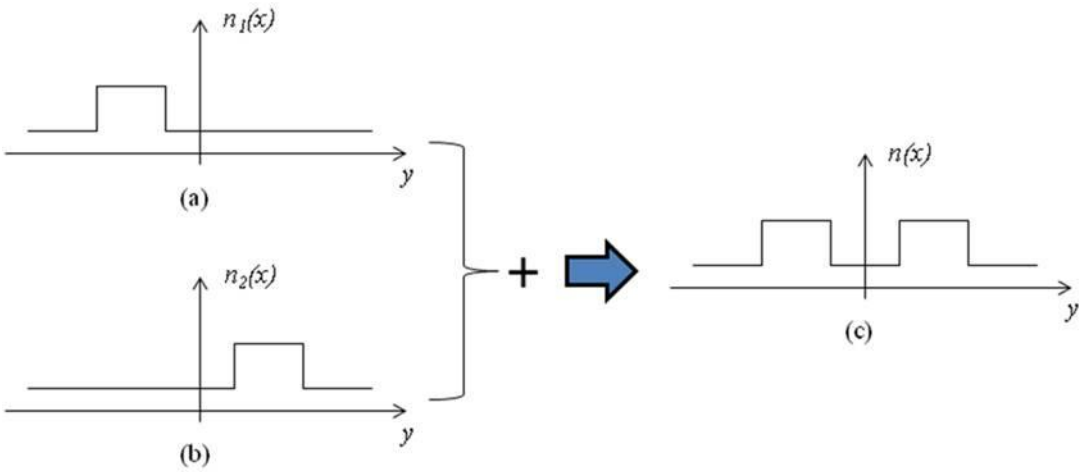

Figure 2-4: (a) and (b) The refractive index profiles for two individual step index planar waveguides and (c) The refractive index profile for a directional coupler waveguides.

$$\nabla_t^2 E_y^{(1)} + [k_0^2 n_1^2(x,y) - \beta_1^2] E_y^{(1)} = 0\,, \tag{2.36}$$

$$\nabla_t^2 E_y^{(2)} + [k_0^2 n_2^2(x,y) - \beta_2^2] E_y^{(2)} = 0\,. \tag{2.37}$$

where

$$\nabla_t^2 = \frac{\partial^2}{\partial x^2} + \frac{\partial^2}{\partial y^2}\,. \tag{2.38}$$

The total transverse electric field in the directional coupler structure is

$$E_y = A(z)E_y^{(1)}(x,y)e^{-j(\beta_1 z - \omega t)} + B(z)E_y^{(2)}(x,y)e^{-j(\beta_2 z - \omega t)}\,. \tag{2.39}$$

where *A(z)* and *B(z)* are the amplitudes of the fields in the waveguides 1 and 2, respectively. If the separation of the waveguides 1 and 2 is infinite, *A(z)* and *B(z)* are constants and the total field in the coupler waveguides is approximated by the sum of the unperturbed fields. However, if the gap between the waveguides is close to obtain a coupling effect, the perturbation polarization is

$$P_{per}(x,y,z) = e^{j\omega t}\varepsilon_0[A(z)E_y^{(1)}(x,y)\Delta n_1^2 e^{-j\beta_1 z} + B(z)E_y^{(2)}(x,y)\Delta n_2^2 e^{-j\beta_2 z}]\,. \tag{2.40}$$

where, $\Delta n_1^2 = n^2(x) - n_1^2(x)$ and $\Delta n_2^2 = n^2(x) - n_2^2(x)$.

Substituting equations (2.39) and (2.40) into the equation (2.30), neglecting the reverse propagation terms, and using equations (2.36) to (2.38).

$$\frac{\partial^2 A(z)}{\partial z^2} E_y^{(1)}(x,y)e^{-j\beta_1 z} + \frac{\partial^2 B(z)}{\partial z^2} E_y^{(2)}(x,y)e^{-j\beta_2 z}$$

$$- j2\beta_1 \frac{\partial A(z)}{\partial z} E_y^{(1)}(x,y)e^{-j\beta_1 z} + - j2\beta_2 \frac{\partial B(z)}{\partial z} E_y^{(2)}(x,y)e^{-j\beta_2 z}$$

$$= -\mu\varepsilon_0\omega^2[A(z)E_y^{(1)}(x,y)\Delta n_1 e^{-j\beta_1 z} + B(z)E_y^{(2)}(x,y)\Delta n_2 e^{-j\beta_2 z}]\,. \tag{2.41}$$

As in the previous section, if the amplitude A(z) and B(z) vary slowly by the perturbation, the second derivatives terms are much smaller than the first derivatives terms,

$\left|\partial^2 A/\partial z^2\right| << \beta_m \left|\partial A/\partial z\right|$ and $\left|\partial^2 B/\partial z^2\right| << \beta_m \left|\partial B/\partial z\right|$. Therefore, $\partial^2 A/\partial z^2$ and $\partial^2 B/\partial z^2$ are neglected.

Multiplying $E_y^{(1)*}$, which is a conjugation of $E_y^{(1)}$, on both sides of the equation (2.41) and integrating over x, then this equation becomes

$$\frac{\partial A(z)}{\partial z}\iint E_y^{(1)*}E_y^{(1)}dxdy\cdot e^{-j\beta_1 z}+\frac{\beta_2}{\beta_1}\frac{\partial B(z)}{\partial z}\iint E_y^{(1)*}E_y^{(2)}dxdy\cdot e^{-j\beta_2 z}$$

$$=-j\frac{k_0^2}{2\beta_1}\left\{A(z)\iint E_y^{(1)*}\Delta n_1 E_y^{(1)}dxdy\cdot e^{-j\beta_1 z}+B(z)\iint E_y^{(1)*}\Delta n_2 E_y^{(2)}dxdy\cdot e^{-j\beta_2 z}\right\}. \quad (2.42)$$

The second term on the left side of the equation (2.42) is omitted because of the orthogonality between $E_y^{(1)}$ and $E_y^{(2)}$.

The equations (2.41) is simplified to

$$\frac{dA}{dz}=-j\kappa_{11}A(z)-j\kappa_{12}Be^{-j2\delta z}. \quad (2.43)$$

where

$$2\delta=\beta_2-\beta_1=\Delta\beta, \quad (2.43\text{-}1)$$

$$\kappa_{11}=\frac{k_0^2}{2\beta_1}\frac{\int\int_{-\infty}^{\infty}E_y^{(1)^*}\Delta n_1^2 E_y^{(1)}dxdy}{\int\int_{-\infty}^{\infty}E_y^{(1)^*}E_y^{(1)}dxdy}, \text{ and } \kappa_{12}=\frac{k_0^2}{2\beta_1}\frac{\int\int_{-\infty}^{\infty}E_y^{(1)^*}\Delta n_2^2 E_y^{(2)}dxdy}{\int\int_{-\infty}^{\infty}E_y^{(1)^*}E_y^{(1)}dxdy}. \quad (2.43\text{-}2)$$

Multiplying $E_y^{(2)*}$, which is a conjugation of $E_y^{(1)}$, on both sides of the equation (2.41) and integrating over x, then the equations (2.41) is simplified as

$$\frac{dB}{dz}=-j\kappa_{22}B(z)-j\kappa_{21}Ae^{j2\delta z}. \quad (2.44)$$

where

$$\kappa_{22} = \frac{k_0^2}{2\beta_2} \frac{\int\int_{-\infty}^{\infty} E_y^{(2)^*} \Delta n_1^2 E_y^{(2)} dxdy}{\int\int_{-\infty}^{\infty} E_y^{(2)^*} E_y^{(2)} dxdy}, \text{ and } \kappa_{21} = \frac{k_0^2}{2\beta_2} \frac{\int\int_{-\infty}^{\infty} E_y^{(2)^*} \Delta n_2^2 E_y^{(1)} dxdy}{\int\int_{-\infty}^{\infty} E_y^{(1)^*} E_y^{(1)} dxdy} \quad (2.44\text{-}1)$$

There are the alternative expression of Equation (2.43) and (2.44) and to obtain these, let

$$R(z) = A(z)e^{-j\delta z}, \quad (2.45)$$

$$S(z) = B(z)e^{j\delta z}. \quad (2.46)$$

where *R(z)* and *S(z)* are the amplitudes of the fields in the waveguides 1 and 2, respectively. Substitute equations (2.45) and (2.46) into equation (2.43) and (2.44)

$$\frac{dR(z)}{dz} = j(\delta - \kappa_{11})R(z) - j\kappa_{12}S(z), \quad (2.47)$$

$$\frac{dS(z)}{dz} = -j(\delta + \kappa_{22})S(z) - j\kappa_{21}R(z). \quad (2.48)$$

In the equations (2.47) and (2.48), κ_{11} and κ_{22} are the corrections of the propagation constants of each individual waveguide mode by presence of the other waveguide, and these correction factors are normally neglected. The final form is, therefore,

$$\frac{dR(z)}{dz} = j\delta R(z) - j\kappa_{12}S(z), \quad (2.49)$$

$$\frac{dR(z)}{dz} = -j\delta S(z) - j\kappa_{21}R(z), \quad (2.50)$$

$$|R(z)|^2 + |S(z)|^2 = 1. \quad (2.51)$$

Equation (2.49) and (2.50) is written in matrix form [2-7] as:

$$\frac{d}{dz}\begin{bmatrix} R(z) \\ S(z) \end{bmatrix} = j\begin{bmatrix} \delta & -\kappa_{12} \\ -\kappa_{21} & -\delta \end{bmatrix}\begin{bmatrix} R(z) \\ S(z) \end{bmatrix}. \quad (2.52)$$

The solution of equation (2.52) is

$$\begin{bmatrix} R(z) \\ S(z) \end{bmatrix} = \begin{bmatrix} \cos sz + j\frac{\delta}{s}\sin sz & -j\frac{\kappa_{12}}{s}\sin sz \\ -j\frac{\kappa_{21}}{s}\sin sz & \cos sz - j\frac{\delta}{s}\sin sz \end{bmatrix} \begin{bmatrix} R(0) \\ S(0) \end{bmatrix}, \tag{2.53}$$

$$\kappa = \sqrt{\kappa_{12}\kappa_{21}}\,. \tag{2.54}$$

where

$$s = \sqrt{\kappa^2 + \delta^2}\,. \tag{2.55}$$

The equation (2.53) is the transfer matrix for the directional coupler modulator.

In case of symmetric coupler (κ_{12}= κ_{21}) with δ=0, matrix (2.53) is simplified as

$$\begin{bmatrix} R(z) \\ S(z) \end{bmatrix} = \begin{bmatrix} \cos \kappa z & -j\sin \kappa z \\ -j\sin \kappa z & \cos \kappa z \end{bmatrix} \begin{bmatrix} R(0) \\ S(0) \end{bmatrix}. \tag{2.56}$$

When the condition of the incident light is R(0)=1 and S(0)=0, the matrix (2.56) is more simplified as

$$\begin{bmatrix} R(z) \\ S(z) \end{bmatrix} = \begin{bmatrix} \cos \kappa z \\ -j\sin \kappa z \end{bmatrix}. \tag{2.57}$$

The power in each waveguide is obtained from:

$$\begin{bmatrix} P_R(z) \\ P_S(z) \end{bmatrix} = \begin{bmatrix} RR^* \\ SS^* \end{bmatrix} = \begin{bmatrix} \cos^2 \kappa z \\ \sin^2 \kappa z \end{bmatrix}. \tag{2.58}$$

If the optical power is completely transferred from one waveguide to the other waveguide after propagating certain length, this is defined as the coupling length, L_c. At that length, $P_R(L_c) = 0$ and $P_S(L_c) = 1$.

$$P_S(L_c) = \sin^2 \kappa L_c = 1. \tag{2.59}$$

Therefore, the coupling length is

$$L_c = \frac{\pi}{2\kappa}. \tag{2.60}$$

If δ is not equal to zero and R(0)=1, S(0)=0, the matrix (2.53) becomes

$$\begin{bmatrix} R(z) \\ S(z) \end{bmatrix} = \begin{bmatrix} \cos sz + j\frac{\delta}{s}\sin sz \\ -j\frac{\kappa_{21}}{s}\sin sz \end{bmatrix}. \tag{2.61}$$

The power in each waveguide is

$$\begin{bmatrix} P_a(z) \\ P_b(z) \end{bmatrix} = \begin{bmatrix} RR^* \\ SS^* \end{bmatrix}. \tag{2.62}$$

The optical power output of the second arm of the directional coupler with δ is

$$P_b(L_c) = \frac{\kappa_{21}^2}{\kappa_{12}\kappa_{21} + \delta^2}\sin^2\left(\sqrt{\kappa_{12}\kappa_{21} + \delta^2}\, z\right). \tag{2.63}$$

Equation (2.63) is for the intensity response function of the directional coupler modulator.

For the switching operation of the coupler modulator with the device length of L_c, δ should be calculated to satisfy $P_b(L_c) = 0$. For the symmetric coupler modulator which has $\kappa = \kappa_{12} = \kappa_{21}$,

$$\sin^2\left(\sqrt{\kappa^2 + \delta_{switch}^2}\, L_c\right) = 0. \tag{2.64}$$

and by using equation 2.78

$$\delta_{switch} L_c = \frac{\sqrt{3}\pi}{2}. \tag{2.65}$$

For the most of the modulator designs, the product $\delta_{switch} L$ is in general a constant.

2.2 Electrooptic Effect

2.2.1 Introduction

The concept of the electooptic effect is that an applied electric field to electro optic materials, such as $LiNbO_3$, KH_2PO_4, and $GaAs$ semiconductors, changes their optical refractive index [2-1]. The relation between refractive index and the electric field is given as

$$n(E) = n_0 + a \cdot E + b \cdot E^2 . \tag{2.66}$$

where $n(E)$ in the left side of the equation is the optical refractive index in the presence of an electric field, the first, second and third terms of this right side in the equation are the initial refractive index, Pockels effect (linear electrooptic effect), and Kerr effect, respectively. John Kerr discovered the quadratic electro optic effect in 1875 and Friedrich Pockels was first to describe the linear electro optic effect in 1893 [2-2]. The linear electrooptic effect is commonly used for electrooptic modulators.

2.2.2 Index Ellipsoid

Index ellipsoid needs to be discussed before describing electooptic effect because it explains how light travels through an isotropic or anisotropic crystal medium. The optical refractive index is determined by the propagation direction and polarization of the optical field in a crystal medium [2-1].

In an anisotropic medium, the electric displacement vector **D** is related to the electric field by dielectric tensor,

$$\mathbf{D} = \varepsilon_o [\varepsilon_r] \mathbf{E} . \tag{2.67}$$

where the **E** is electric field, and $[\varepsilon_r]$ is the dielectric tensor for the medium. The dielectric tensor is expressed as following.

$$[\varepsilon_r] = \begin{bmatrix} \varepsilon_{xx} & \varepsilon_{xy} & \varepsilon_{xz} \\ \varepsilon_{yx} & \varepsilon_{yy} & \varepsilon_{yz} \\ \varepsilon_{zx} & \varepsilon_{zy} & \varepsilon_{zz} \end{bmatrix}. \tag{2.68}$$

This dielectric tensor is simplified to the diagonal matrix form when the principal dielectric axes are determined by the crystal's property. Let the principal axes be along the x, y, and z directions and the off-diagonal elements of dielectric tensor are now equal to "0". Then the dielectric tensor for the principal axes is

$$[\varepsilon_r] = \begin{bmatrix} \varepsilon_x & 0 & 0 \\ 0 & \varepsilon_y & 0 \\ 0 & 0 & \varepsilon_z \end{bmatrix}. \tag{2.69}$$

where $\varepsilon_i = n_i^2$ (i=x, y, and z) and n_i is the optical refractive index of each direction of principal axis.

In terms of the principal axes the stored electric energy in the medium is defined as

$$W = \frac{1}{2}\mathbf{E}\cdot\mathbf{D} = \frac{1}{2\varepsilon_0}\left(\frac{D_x^2}{n_x^2} + \frac{D_y^2}{n_y^2} + \frac{D_z^2}{n_z^2}\right). \tag{2.70}$$

Using following normalization:

$$\begin{pmatrix} D_x \\ D_y \\ D_z \end{pmatrix} = \sqrt{2\varepsilon_0 W}\begin{pmatrix} x \\ y \\ z \end{pmatrix}. \tag{2.71}$$

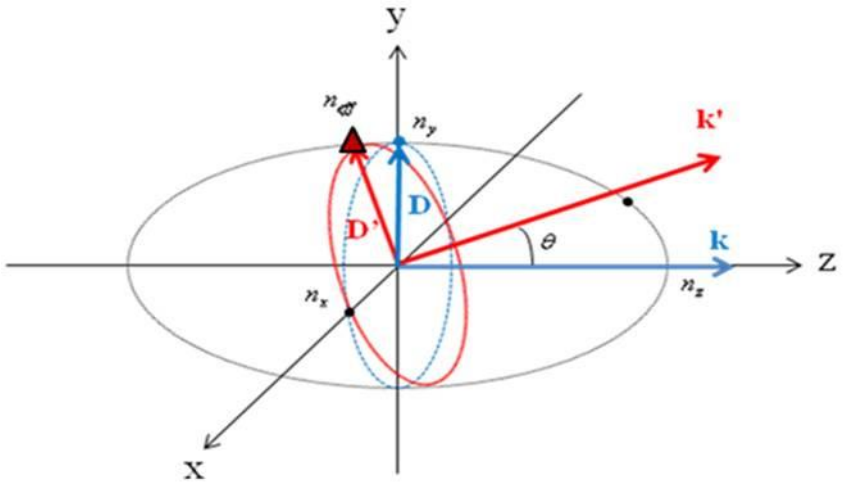

Figure 2-5: Index ellipsoid which is a three-dimensional ellipse.

The equation (2.70) becomes

$$\frac{x^2}{n_x^2}+\frac{y^2}{n_y^2}+\frac{z^2}{n_z^2}=1. \tag{2.72}$$

This is the equation of the index ellipsoid, and figure 2-5 shows index ellipsoid form.

In figure 2-5, D and D' are the electric displacement flux densities of the light waves which have the wavevectors of k and k', respectively. When the light wave propagates along z axis as shown in figure 2-5, the cross point which is indicated by blue point between the index ellipsoid and D is the refractive index n_y seen by the light wave. When the light wave propagates with an angle θ on yz plane, which of the wavevector is k' as shown in figure 2-5, the refractive index seen by the light wave is also the cross point which is indicated by triangle between an ellipsoid and D', which is n_{eff}.

2.2.3 Pockel's Effect

The linear electrooptic effect, or Pockel's effect, is the refractive index changing due to an applied electric field to a crystal. The amount of the refractive index change depends on the orientation of the crystal and the direction of the applied electric field.

When an arbitrarily directed static electric field is applied to the crystal, the index ellipsoid is perturbed, and then the equation (2.72) becomes

$$Ax^2 + By^2 + Cz^2 + 2Pyz + 2Qzx + 2Rxy = 1. \tag{2.73}$$

The perturbation of the dielectric constant terms are obtained by following matrix equation:

$$\begin{bmatrix} A - \frac{1}{n_x^2} \\ B - \frac{1}{n_y^2} \\ C - \frac{1}{n_z^2} \\ P \\ Q \\ R \end{bmatrix} = \begin{bmatrix} r_{11} & r_{12} & r_{13} \\ r_{21} & r_{22} & r_{23} \\ r_{31} & r_{32} & r_{33} \\ r_{41} & r_{42} & r_{43} \\ r_{51} & r_{52} & r_{53} \\ r_{61} & r_{62} & r_{63} \end{bmatrix} \begin{bmatrix} E_x \\ E_y \\ E_z \end{bmatrix}. \tag{2.74}$$

where the 6×3 matrix here r_{ij} (i, j=1,2,3,...,6) is the electrooptic tensor and E_x, E_y, and E_z are applied electric field along these axes.

For example, GaAs is an isotropic crystal medium, and n_x is equal to n_y, n_z, and n_0. The index ellipsoid, therefore, is

$$\frac{x^2}{n_o^2} + \frac{y^2}{n_o^2} + \frac{z^2}{n_o^2} = 1. \tag{2.75}$$

The symmetry group of GaAs is $\bar{4}3m$ [2-1], and the electrooptic tensor is

$$r_{GaAs} = \begin{bmatrix} 0 & 0 & 0 \\ 0 & 0 & 0 \\ 0 & 0 & 0 \\ r_{41} & 0 & 0 \\ 0 & r_{52} & 0 \\ 0 & 0 & r_{63} \end{bmatrix}. \tag{2.76}$$

where coefficients of the tensor are $r_{41} = r_{52} = r_{63}$.

Using equations (2.73)~(2.76), the index ellipsoid in GaAs with applied electric field becomes

$$\frac{x^2}{n_o^2} + \frac{y^2}{n_o^2} + \frac{z^2}{n_o^2} + 2zxr_{41}E_x + 2yzr_{41}E_z + 2xyr_{41}E_y = 1. \tag{2.77}$$

where the first three terms are independent of the applied electric field.

When the electric field in z direction is applied, the perturbed index ellipsoid equation (2.77) changes to

$$\frac{x^2}{n_o^2} + \frac{y^2}{n_o^2} + \frac{z^2}{n_o^2} + 2yzr_{41}E_z = 1. \tag{2.78}$$

In the equation (2.78), there is a mixed term, and because of this mixed term, the major axes of index ellipsoid are no longer parallel to the principal axes. Therefore, new principal axes need to be defined, which is used for new index ellipsoid

$$\frac{x'^2}{n_{x'}^2} + \frac{y'^2}{n_{y'}^2} + \frac{z'^2}{n_{z'}^2} = 1 \tag{2.79}$$

where x', y', and z' are the new principal axes.

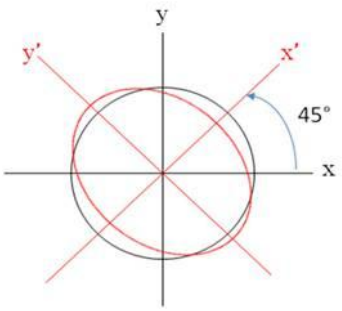

Figure 2-6: x and y axes are the principal axes without applied electric field and x' and y' axes with applied electric field.

The relation between the new principal axes and old principal axes is obtained by:

$$x = x'\cos 45^\circ + y'\sin 45^\circ = \frac{1}{\sqrt{2}}(x'+y'), \tag{2.80}$$

$$y = -x'\sin 45^\circ + y'\cos 45^\circ = \frac{1}{\sqrt{2}}(-x'+y'). \tag{2.81}$$

From equation (2.80) and (2.81), the new principal axes rotated at 45° from the old principal axes and the magnitudes of refractive index are also changed as shown in figure 2-6. The equation (2.78) is modified to equation (2.82) by using equation (2.80) and (2.81).

$$\left(\frac{1}{n_o^2} - r_{41}E_z\right)x'^2 + \left(\frac{1}{n_o^2} + r_{41}E_z\right)y'^2 + \frac{z^2}{n_o^2} = 1. \tag{2.82}$$

Equation (2.82) may rewrite the index ellipsoid equation as

$$\frac{x'^2}{n_{x'}^2} + \frac{y'^2}{n_{y'}^2} + \frac{z^2}{n_o^2} = 1. \tag{2.82-1}$$

From equation (2.82-1) new refractive index of x' and y' axes are obtained as in equation (2.83) and (2.84).

$$n_{x'} = n_o \frac{1}{\left(1 - n_o r_{41}E_z\right)^{1/2}} \cong n_o + \frac{1}{2}n_o^3 r_{41}E_z, \tag{2.83}$$

$$n_{y'} = n_o \frac{1}{\left(1 + n_o r_{41} E_z\right)^{1/2}} \cong n_o - \frac{1}{2} n_o^3 r_{41} E_z \,. \tag{2.84}$$

In the equations (2.83) and (2.84), $n_{x'}$ can be simplified using a simple binomial expansion of the quadratic terms because the magnitude of $r_{41}E_z$ is usually small compared to n_0^2. The refractive index in *x'* and *y'* are increased and decreased, respectively, but is not changed along z axis. From equation (2.83) and (2.84), the polarized light wave along *x'* or *y'* axes experience the refractive index changes, when the electric field is applied along z direction.

The relation of the principal axes, applied electric field and polarization of the propagating light in GaAs is shown in figure 2-7, which illustrates a directional coupler modulator. In this figure, the waveguides are built on GaAs substrate along y' axis, the light propagates along y' axis, the electric field of the light is polarized along x' axis, and the dc electric field is applied along z axis. When the crystal directions are considered, the axes of z, x', and y' are matched to $[001]$, $[1\bar{1}0]$, and $[110]$, respectively [2-3].

As shown above, the refractive indices on the new principal axes are linearly changed by the applied electric field.

2.2.4 Switching Voltage Calculation

From the previous section, an applied electric field changes the refractive index of the electrooptic dielectric medium, and changes the propagation constant. When the equation (2.43-1) is considered, it may be rewritten as

$$\delta = \frac{\Delta\beta}{2} = \frac{\pi \Delta n}{\lambda_0} \,. \tag{2.85}$$

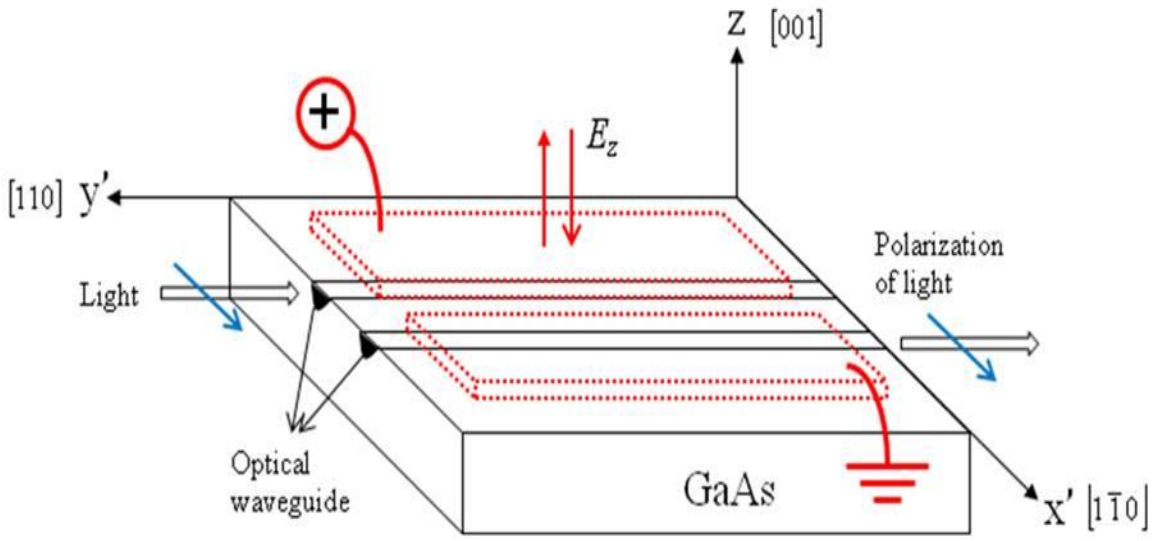

Figure 2-7: The setup of the directional coupler modulator to describe the relation of the principal axes, applied electric field, and polarization of the light.

2.2.5 Switching Voltage Calculation

From the previous section, an applied electric field changes the refractive index of the electrooptic dielectric medium, and changes the propagation constant. When the equation (2.43-1) is considered, it may be rewritten as

$$\delta = \frac{\Delta\beta}{2} = \frac{\pi\Delta n}{\lambda_0}. \tag{2.85}$$

where

$$\Delta n = n_o^3 r_{41}\Gamma E_z = n_o^3 r_{41}\Gamma\frac{V}{d}. \tag{2.86}$$

where

$$\Gamma \equiv \frac{\int\int E_{op}^2 E_{electrode}\,dxdy}{\int\int E_{op}^2\,dxdy}. \tag{2.87}$$

where Γ is the overlap integral. For the directional coupler modulators with equation (2.83), if the positive electric field is applied on one waveguide and negative electric field

is applied on the other waveguide, the optical refractive index difference $\Delta n = n_o^3 r_{41} \Gamma E_z$. If the electric field is applied only on the one waveguide, $\Delta n = (1/2) n_o^3 r_{41} \Gamma E_z$. In this section, the first case is used. When the electric field is applied to the waveguide, it cannot effect to whole optical field because of size mismatch. Therefore, the overlap integral Γ between optical field and the applied electric field should be considered [2-4]. Substitute equation (2.87) into (2.85) and multiply L_c both side

$$\delta L_c = \frac{\left(\pi n^3 r_{41} \Gamma V L_c\right)}{\lambda_0 d}. \tag{2.88}$$

To obtain switching condition, substitute equation (2.88) into equation (2.65). The voltage to satisfy equation (2.89) is called the switching voltage.

$$\frac{\left(\pi n^3 r_{41} \Gamma V_{switch} L_c\right)}{\lambda_0 d} = \frac{\pi\sqrt{3}}{2}. \tag{2.89}$$

The switching voltage and coupling length product from equation(2.89) is

$$V_{switch} L_c = \frac{\sqrt{3}\lambda_0 d}{2 n^3 r_{41} \Gamma}. \tag{2.90}$$

The equation (2.90) is rewritten as equation (2.91) with coupling factor, p.

$$V_{switch} L_c = p \frac{\lambda_0 d}{n^3 r_{41} \Gamma}. \tag{2.91}$$

Coupling factor depends on the modulator type; $p = \sqrt{3}$, $\sqrt{3}/2$, and 0.5 for the normal directional coupler modulator, the directional coupler modulator with push-pull operation, and Mach-Zehnder, respectively.

Table 2-1: Parameters for calculating voltage and coupler length products.

Parameters	**GaAs/$Al_{0.2}Ga_{0.8}As$**	**$LiNBO_3$**
Wavelength	1.3 μm	1.3 μm
Electrode Spacing, d	3 μm	8 μm
Overlap Integral, Γ	0.65	0.55
Electro-optic Coefficient at 1.3mm	1.455×10^{-12} m/V	31.5×10^{-12} m/V
Refractive Index at 1.55 mm	3.41	2.138
Ratio, $(VL_c)/p$	10.39Vcm	6.14 Vcm

Table 2-2: Voltage and coupler length products.

Modulator Design	**GaAs/$Al_{0.2}Ga_{0.8}As$ V_sL(V·cm)**	**$LiNBO_3$ V_sL(V·cm)**
Trapezoidal Coupler	12.47	7.37
π-Phase Shift Coupler	18.7	11.05
Conventional Directional Coupler	9.04	5.34
Mach-Zehnder	5.19	3.07

For specific modulator designs, the product $V_{switch}L_c$ is in general a constant as well [2-4]. The calculated switching voltage length products for the various modulators are given below in the Tables 2-1 and 2-2. The parameters for these switching voltage calculations for the modulators built in GaAs and separately for $LiNBO_3$ are shown in Table 2-1.

The switching voltage length product for these two modulators, in GaAs and $LiNBO_3$, are separately shown in Table 2-2. The voltage-length product with commercial modulators is quoted for the push-pull case, where these voltage-length product numbers are divided by factor of 2.

2.3 Distortion in Nonlinear Optical Modulators

Nonlinear optical modulators generate harmonics and intermodulation distortion components when excited with two sinusoidal signals with frequencies which are close to each other. When the optical signal is modulated by two different RF signals with same amplitude but slightly different frequencies, f_a and f_b, the output of the modulated optical signal has not only the fundamental signal components (at f_a and f_b), but also distortion terms including second harmonics ($2f_a$, $2f_b$), third harmonics ($3f_a$, $3f_b$), second-order intermodulation distortions (IMD2) ($|f_a \pm f_b|$), and third order intermodulation distortions (IMD3) ($|2f_a \pm f_b|$, $|2f_b \pm f_a|$) [7], which are shown schematically in figure 2-8.

The third order intermodulation distortion (IMD3) term is important as these frequencies are close to f_1 and f_2, and if a bandpass filter for the two tones is used then these may appear within the filter bandwidth. For broadband operation, the second order intermodulation distortion (IMD2) is important as this defines the input power beyond which the second order products start to appear.

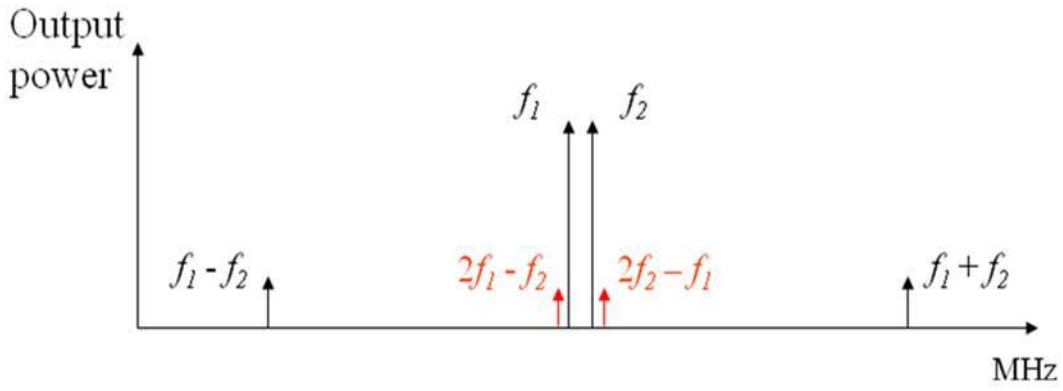

Figure 2-8: Fundamental and intermodulation distortion components for two-tone signal

2.3.1 Distortion Calculation

The usual technique for calculating the distortion of modulators is to express the response function as a polynomial in the applied voltage, and thus for the present case the output signal power is [2-8]

$$v_{out} = a_0 + a_1 v_{appl} + a_2 v_{appl}^2 + a_3 v_{appl}^3 + a_4 v_{appl}^4 + \cdots\cdots. \tag{2.92}$$

where, a_i is the nominal network voltage gain, v_{app} is input voltage, and v_{out} is output voltage. However, expressing the response function in polynomial form results in approximations.

Another method is to superpose two signals at slightly different frequencies, and take the Fourier transform of the response function, either in the Fast Fourier Transform (FFT) technique [2-9]~[2-10], or in the usual integral form. However, it is necessary that the periodicity is not violated by taking too small a sequence, and this also results in inaccuracies due to the large number of points required. The most accurate method is to use the two dimensional (2D) FFT technique in which the two dimensions correspond to the time periods of the two tones passing through the modulator simultaneously. Matlab has this 2D FFT as a standard function and is used in this thesis to calculate normalized frequency components of harmonics and intermodulation distortions.

For the distortion calculation in the modulator response function the input signal with two-tone is written as [2-8]:

$$v_{in}(t) = V_{Bias} + v_{RF}\,. \tag{2.93}$$

where

$$v_{RF} = A\left[\cos(2\pi f_1 t_1) + \cos(2\pi f_2 t_2)\right]. \tag{2.94}$$

V_{bias} is the DC bias voltage of the optical modulator and v_{RF} is the modulation input voltage with two tones of f_1 and f_2.

The distortion calculation in the 2D FFT method requires normalized input values. Therefore, the input RF voltage is normalized to the switching voltage and then modulation depth, *m*, is defined by the following equations:

$$h(t_1, t_2) \equiv \frac{v_{RF}(t_1, t_2)}{V_{switch}}, \tag{2.95}$$

$$m \equiv \frac{2A}{V_{Switch}}. \tag{2.96}$$

Thus, *h* is the normalized input RF voltage and is written as [2-11]:

$$h(t_1, t_2) = \frac{m}{2}\left[\cos(2\pi f_1 t_1) + \cos(2\pi f_2 t_2)\right]. \tag{2.97}$$

By using the 2D FFT function in Matlab with normalized input RF voltage, *h*, the frequency components of output harmonics and intermodulation distortions are calculated as listed in Table 2-3. The powers for the fundamental signals, harmonics, and distortions are calculated by using these frequency components in Chapter 3.

Table 2-3: The frequency components of fundamental signal and distortions using 2D FFT code in Matlab.

Fundamental signal	$H(f_1,0),\ H(0,f_2)$
Second harmonics	$H(2f_1,0),\ H(0,2f_2)$
Second order intermodulation distortion	$H(f_1,f_2),\ H(f_1,-f_2)$
Third order intermodulation distortion	$H(2f_1,f_2), H(2f_1,-f_2),\ H(f_1,2f_2),$ $H(-f_1,2f_2)$

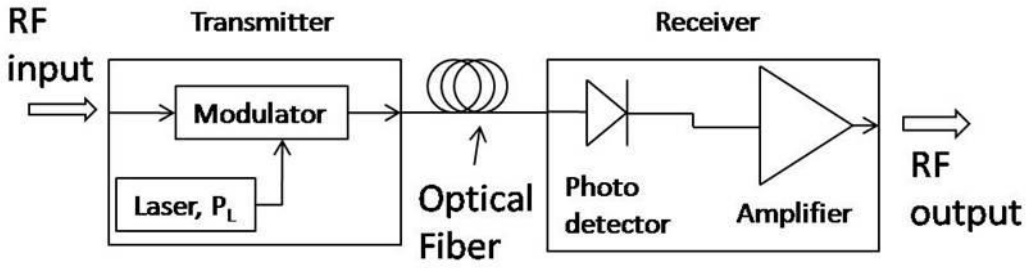

Figure 2-9: Common form of a fiber optical link.

2.4 Optical Link Model

In the previous sections, the theory of the optical modulator is considered. However, it is only a single component of the fiber optic link. The fiber optic link commonly consists of the several components which include the transmitter, the optical fiber, and the receiver [2-12] as shown in figure 2-9. The input is the transmitter which includes a laser, an external modulator which modulates the light with the RF signal. The output is the receiver which includes the photodetector, and recovers the RF signal from modulated optical signal. The fiber is used for the transmission of the optical signal.

In this section, the fiber optic link performance is evaluated for the link parameters including the gain, noise, and distortions [2-13]. Table 2-4 shows the symbols of the parameters used in estimating the link gain, noise, and distortion.

2.4.1 Link Gain and Noise

The basic link parameters are the link gain and link noise because several other link parameters depend upon them. There are a lot of definitions of gain in RF system. The most applicable to analog links is the transducer power gain.

$$G_{total} \equiv 10 \cdot \log\left(\frac{P_{output}}{P_{input}}\right). \tag{2.98}$$

where P_{output} is the power delivered into a matched load and P_{input} is the available power of the source which is $v_{in}^2/4R_s$ [2-12] ~ [2-13].

If the gains of RF-to-Optical Modulation part, optical fiber, and Optical-to RF demodulation part are G_M, G_{Fiber}, and G_D in dB scale, respectively. The total gain, G_{total}, is also expressed as

$$G_{total} \equiv G_M + G_F + G_D. \tag{2.99}$$

where

$$G_M = 10\log\left[R_S\{P_L(1-L_o)\}^2\left|\frac{\partial T}{\partial V}\right|_{V_{bias}}^2\right], \tag{2.100}$$

$$G_F = 10\log(1) = 0, \tag{2.101}$$

$$G_D = 10\log(r_D^2 R_{load}). \tag{2.102}$$

Table: 2-4 Fiber-Optic Link Parameters.

Parameter	Symbol
Laser Power	P_L
Laser Noise	RIN
Total Optical Loss	L_O
Modulator Sensitivity	V_{Switch}
Modulator Impedance	R_M
Detector Responsivity	r_D
Detector Termination	R_T
Load Impedance	R_L
Noise Bandwidth	B

In equations (2.100~102), R_s is the source resistance at the modulator, P_L is the input optical power, L_o is the total loss, T is the optical amplitude response function of the optical modulator, r_D is the responsivity of the photodiode, and R_{load} is the load resistance at the photodetector part. The expression of the total gain, g_{Total} is

$$g_{Total} = R_{load} R_S \left\{ P_L (1 - L_o) r_D \left| \frac{\partial T}{\partial V} \right|_{V_{bias}} \right\}^2 . \tag{2.103}$$

The Noise Power, P_{Noise}, includes the sum of the thermal noise, shot noise, relative intensity noise[2-13~14], and detector noise of the link.

$$P_{noise} = g_{Total} kTB + \frac{1}{2} q I_{DC} RB + \frac{1}{4} I_{DC}^2 RB \cdot RIN + kTB . \tag{2.104}$$

where g is RF-photonic link Gain, k is Boltzmann's constant, T is temperature, **B** is the measurement bandwidth, I_{dc} is the dc photocurrent, and $R=R_s=R_{load}=50\ \Omega$. The first term is the input thermal noise, the second term is photodetector's shot noise, the third term is the RIN in the laser output, and the forth term is the thermal noise from the photodetector termination impedance.

The noise figure is defined as

$$NF = 10 \log \left(\frac{s_{in} / n_{in}}{s_{out} / n_{out}} \right). \tag{2.105}$$

where s_{in}, s_{out}, n_{in}, and n_{out} are the input signal, output signal, input noise, and output noise powers, respectively. The input noise power, $n_{in} = kTB$, and s_{out} and n_{out} are written as

$$s_{out} = g_{Total} \cdot s_{in} , \tag{2.106}$$

$$n_{out} = g \cdot n_{in} + n_{ext} . \tag{2.107}$$

where n_{ext} includes photodetector's shot noise, RIN in the laser output, and the thermal noise from the photodetector.

Substitute (2.106) and (2.107) into (2.105), (2.105) is rewritten

$$NF = 10\log\left(\frac{g_{Total}kTB + \frac{1}{2}qI_{DC}RB + \frac{1}{4}I_{DC}^2RB\cdot RIN + kTB}{g_{Total}kTB}\right)$$

$$= 10\log\left(\frac{P_{Noise}}{g_{Total}kTB}\right). \qquad (2.108)$$

2.5 References

[2-1] A. Yariv, *Optical Electronics in Modern Communications, 5th Ed.* New York: Oxford, 1977.

[2-2] S.L. Chuang, Physics of Optoelectronic Devices, Wiley-Interscience Publication, New York, 1995

[2-3] S. Y. Wang and S.H. Shin, "High-speed III-V electrooptic waveguide modulators at 1.3 μm," Journal of lightwave Tech., vol. 6, no. 6, pp. 78-771, 1988

[2-4] R. C. Alferness, "Waveguide electrooptic modulators," IEEE Trans. On Microwave Theory and Tech., vol. MTT-30, no. 8, pp. 1121-1137, August 1982

[2-5] K. Cheng, Fiber and Electro-optical Components, Handbook of Microwave and Optical Components, vol. 4, Wiley-Interscience, 1991

[2-6] Polloc, Fundamentals of Optoelectronics, Irwin, 1995

[2-7] C. Laliew et al, "A Linearized Optical Directional Coupler Modulator at 1.3 μm," *IEEE Journal of Lightwave Technology*, vol. 18, pp. 1244-9, Sept. 2000.

[2-8] G. M. Kizer, *Microwave Communication*, Ames, IA: Iowa State University Press, 1990

[2-9] William H. Press, Saul A. Teukolsky, William T. Vetterling, and Brian P. Flannery, Numerical recipes in FORTRAN, 2nd, Cambridge, 1992

[2-10] B. P. Lathi, Linear System and Signals, 2nd, Oxford university press, 2004

[2-11] G. E. Betts et al, "On the Linear Dynamic Range of Integrated Electrooptical Modulators," *IEEE J. Quantum Electronics*, vol. QE-22, pp. 1009-1011, July 1986.

[2-12] Charles H. Cox, III, Analog Optical Links Theory and Practice, Cambridge, 2009

[2-13] Scott A. Hamilton, Diego R. Yankelevich, Andr´e Knoesen, Robert T. Weverka, and Richard A. Hill, " Comparison of an In-Line Asymmetric Directional Coupler Modulator with Distributed Optical Loss to Other Linearized Electrooptic Modulators," IEEE Transaction on Microwave Theory and Tech., vol. 47, no. 7, July 1999

[2-14] G. P. Agrawal, Fiber-*Optic Communication Systems, 2nd edition*. New York: Wiley, 1997.

CHAPTER 3 Linear Directional Coupler Modulator Design

3.1 Introduction

Analog fiber optical links require linear modulation, because nonlinearities in the modulator cause to signal distortion and limit the dynamic range. The external modulator is commonly used in high speed analog systems because direct modulation of the laser leads to frequency chirping which causes signal distortion. The widely used electro-optic Mach-Zehnder modulator(MZM) has a nonlinear response and this may be alleviated with a small depth of modulation. To obtain low insertion loss in the link with this low depth of modulation, the optical power needs to be high, 100mW or higher. The electro-absorption modulator may not be able to handle this power, whereas, the MZM in $LiNbO_3$ and III-V semiconductor material should have no difficulty. The electro-optic directional coupler modulator in the same materials will also handle the power, and in addition, lends itself to linearization of the response function.

As discussed in chapter 2, the coupling efficiency, η, or the optical output intensity response function, of the directional coupler modulator is given by [3-1]

$$\eta = \left|S(z)\right|^2_{R(0)=1,S(0)=0} = \frac{\sin^2\left(\kappa L\sqrt{1+\left(\delta/\kappa\right)^2}\right)}{1+\left(\delta/\kappa\right)^2} \quad . \tag{3.1}$$

where κ is a coupling coefficient, L is a coupling length, and δ is $\Delta\beta/2$. $\Delta\beta$ is the difference between the propagation constants of the individual optical waveguide. As shown in equation (3.1), the square root of the response function which is a sinc function, and coupling coefficient of the conventional directional coupler modulator have a Fourier transform relation as shown in figure 3-1.

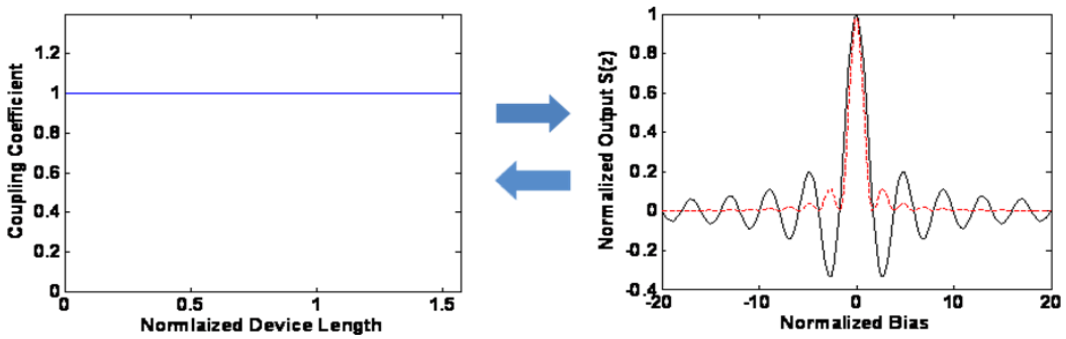

(a) (b)

Figure 3-1: (a) a coupling coefficient and (b) a response function of the conventional uniform directional coupler modulator. The black line is for S(z) and red dashed line is for $|S(z)|^2$.

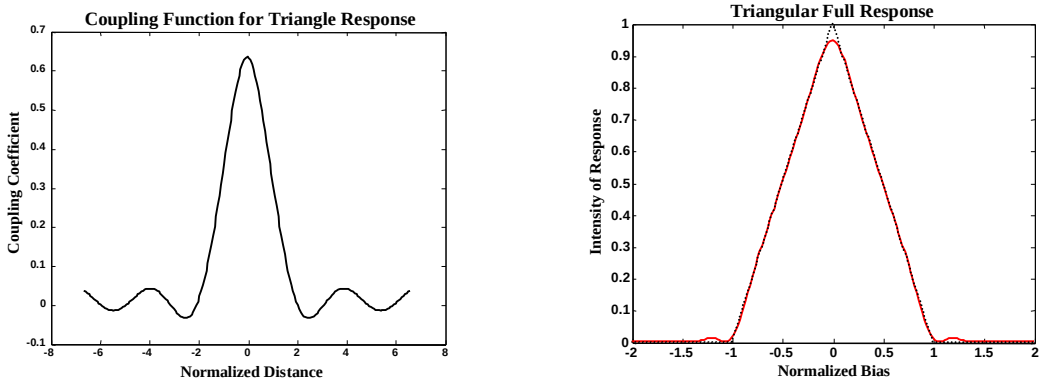

(a) (b)

Figure 3-1-1: (a) Coupling Coefficient (b) Full Response for the Triangular case.

From this Fourier transform relation, the sinc shape of the coupling coefficient is used to obtain the uniform response function for the directional coupler modulator.

A linear intensity response function in the form of a symmetric triangle shown in figure 3-1-1 (a) requires a variable coupling of the form shown in figure 3-1-1 (b). This variable coupling has negative regions and the negative coupling regions are realized by inserting π phase shifts in the coupler with subsequent reversion to the positive coupling as required.

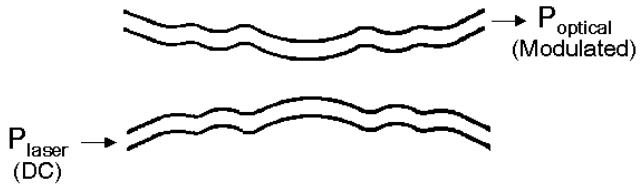

Figure 3-2: Schematic diagram of the variable coupling directional coupler electrooptic modulator. Electrodes on each waveguide (not shown) modulate the power output.

These designs which have variable amplitude and negative coupling increase the linearity of the modulator. The calculations for the second and third order intermodulation distortions (IMD2 and IMD3) of this modulator design were performed and these show spur free dynamic ranges (SFDR) of over 110 dB/Hz$^{2/3}$ in 1 Hz bandwidth for the IMD3 and 100 dB/Hz$^{1/2}$ for the IMD2. The switching voltage is higher than that for the MZM and the propagation loss is high because of variable coupling requires bends in the arms of the coupler.

A linear modulator design uses uniform coupling with negative coupling regions, and the position of these coupling regions were chosen to obtain a linear response. A range of designs have been obtained and two of these based on the location of negative coupling regions show SFDR of 130 dB/Hz$^{2/3}$ for the IMD3 and 125 dB/ Hz$^{1/2}$ for the IMD2 for one design, and 110 dB/Hz$^{2/3}$ and 125dB/ Hz$^{1/2}$ for the IMD3 and IMD2, respectively for the other design but both with increased switching voltages.

3.2 Variable Directional Coupler Modulator

The modulator design shown in figure 3-2 has an additional degree of freedom compared to the Mach-Zehnder, in that the magnitude and phase of the coupling between waveguides may be varied along the length of the device, by changing the spacing and

phase shifts between waveguides or their composition, to influence its response function. This has been used to produce linear directional coupler modulators [3-1].

3.2.1 Design Theory

A. GLM Method

Probably the best-known method for designing variable-coupling directional couplers is the Gel'fand-Levitan-Marchenko (GLM) inverse-scattering method [3-2], which allows synthesis of Butterworth, Chebyshev, Bessel, and other responses. However, although this method has been used to design modulators with linear amplitude response, it has the problem that it neglects the phase response. Modulators designed with this method therefore chirp the optical signal, which adds unwanted distortion to the link.

B. Fourier Transform Method

Many papers [3-3~3-6] have stated that if the coupled power from the dominant mode to the other mode is small, the Fourier transform may be used to characterize the coupling function of the power. To obtain the Fourier transform equation for the power and the coupling function, the Riccati equation is used.

From the coupled mode equations (3.2) and (3.3), which are derived in Chapter 2, it is possible to derive the nonlinear Riccati differential equation with only one dependent variable [3-7].

$$\frac{dR(z)}{dz} = j\delta R(z) - j\kappa_{12} S(z), \tag{3.2}$$

$$\frac{dR(z)}{dz} = -j\delta S(z) - j\kappa_{21} R(z), \tag{3.3}$$

$$|R(z)|^2 + |S(z)|^2 = 1. \tag{3.4}$$

The dependent variable ρ is defined as

$$\rho = \frac{S}{R} \cdot e^{-j\phi(z)} \quad . \tag{3.5}$$

By differentiation of ρ with respect to z,

$$\frac{\partial \rho}{\partial z} = \left(\frac{\frac{\partial S}{\partial z}}{R} - \frac{S\frac{\partial R}{\partial z}}{R^2} - j\frac{S\frac{\partial \phi}{\partial z}}{R} \right) e^{-j\phi(z)}. \tag{3.6}$$

When equations (3.2) and (3.3) are substituted into (3.6), and equation (3.4) is used, the resulting equation has the Riccati equation form:

$$\frac{\partial \rho}{\partial z} = -j\left(2\delta + \frac{\partial \phi}{\partial z} \right)\rho + j\kappa(\rho^2 - 1). \tag{3.7}$$

By using equation (3.4~5), the squared amplitude of S is

$$\eta = |S|^2 = \frac{|\rho|^2}{1 + |\rho|^2}. \tag{3.8}$$

Redefine ρ as

$$\rho = \sigma \cdot e^{-j(2\delta z + \phi)}. \tag{3.9}$$

Substitute equation (3.9) into the Riccati equation (3.7), then

$$\frac{\partial \sigma}{\partial z} = j\kappa\left(\sigma^2 e^{-j(2\delta z + \phi)} - e^{j(2\delta z + \phi)} \right). \tag{3.10}$$

In case of the weak coupling, the absolute value of ρ, which is σ, is small, therefore, the equation (3.10) will be reduced to:

$$\frac{\partial \sigma}{\partial z} = -j\kappa e^{j(2\delta z+\phi)}. \tag{3.11}$$

Then the intensity response function is equal to $|\rho|^2$

$$\eta = |S|^2 = |\rho|^2 = |\sigma|^2. \tag{3.12}$$

When the equation (3.11) is solved over the range of the integration from *–L/2* to *L/2*, the solution is of the form:

$$\eta = |S|^2 \approx \left| \int_{-L/2}^{L/2} \kappa(z) e^{-j(2\delta z+\phi)} dz \right|^2, \tag{3.13}$$

$$|S(\delta)| e^{j\delta L} \approx \int_{-L/2}^{L/2} \kappa(z) e^{j(2\delta z+\phi)} dz. \tag{3.14}$$

where L is the length of the device and δ is the difference of propagation constant between two waveguides discussed in Chapter 2. Since outside of coupler $\kappa = 0$, the boundaries of the integral can be extended to infinity and a Fourier transform of $\kappa e^{j\phi}$ with 2δ as a Fourier frequency parameter. It should be pointed out that the usefulness of this approach in our case would be limited since it assumes that $\rho << 1$. However, for complete power transfer from one guide to the other, $\rho = \infty$, and for half power transfer, $\rho = 1$. Nevertheless, this approach to find the $\kappa(z)$ is used continuously.

The inverse Fourier transform of equation (3.14) is

$$\kappa(z) = \frac{1}{\pi} \int_{-\infty}^{\infty} |S(\delta)| e^{-j\delta(L+2z)} d\delta. \tag{3.15}$$

Now the Fourier transform method can be used to design a linear directional coupler modulator. $|S(\delta)|$ in equation (3.15) needs to be am even function and the equation (3.15) can be simplified as following.

$$\kappa(z) = \frac{2}{\pi}\int_0^{\infty} |S(\delta)| \cos\delta(L+2z) d\delta \,. \tag{3.16}$$

An even response function S(δ) is used because it transforms to a real-valued coupling function [3-8], and because it causes the resulting coupling function to be symmetric about the center of the coupler, which prevents the modulator from chirping the output signal. The coupling function derived from equation (3.16) extends to $\pm\infty$, and this infinity distance will not be realized in practice. Therefore, it needs to be truncated symmetrically to prevent chirp being generated as shown in figure 3-3 (b) blue line. In figure 3-3, the black lines of (a) and (b) are the desired response function and the coupling function, κ, respectively, and blue and thick lines of (b) and (a) are the truncated coupling function and the response function obtained from truncated coupling function by the transfer matrix.

At first glance this approach appears to have one severe limitation: that $\kappa(z_N)$ is essentially the frequency spectrum of the response function, so limiting it to be nonzero only along the length of the coupler ($0 \le z_N \le 1$) must inevitably limit the linearity of the response. Fortunately the Fourier transform method involves substantial approximations that limit its accuracy [3-2], so such a conclusion cannot be drawn. However, it does illustrate that corrections are necessary, particularly because the coupling function must be truncated, to accurately design the modulator for a desired response.

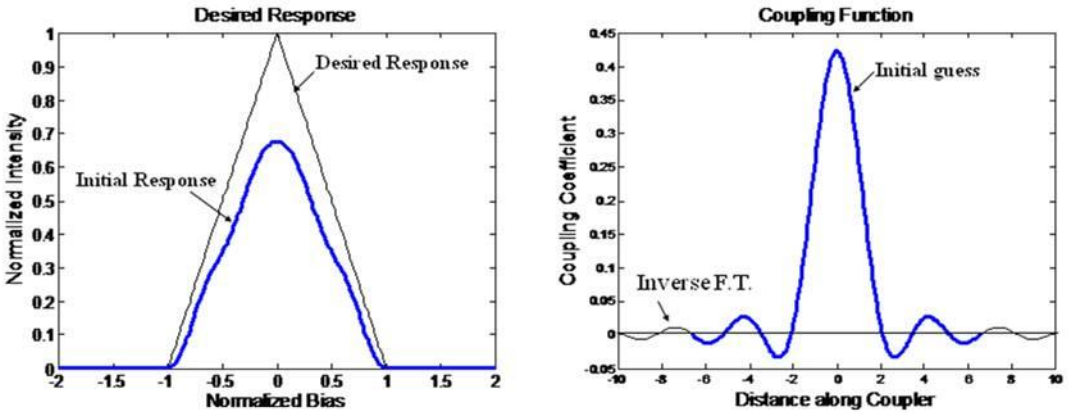

(a) (b)

Figure 3-3: (a) a desired modulator response and (b) its corresponding coupling function obtained through the Fourier transform of the response. The desired response is perfectly linear in the sloped regions, and perfectly flat otherwise.

The truncated coupling function will only provide an approximate form of the desired response as shown in figure 3-3, (a) blue and dark line, and thus needs to be modified to provide a closer agreement.

In the case of the variable coupling directional coupler, the coupler structure represented by the varied coupling function is considered as a cascade of N sections of short length ΔL, $\Delta L << L_c$, and κ is assumed to be uniform for each section. The general solution of the output from each branch of the coupler at any section is

$$\begin{pmatrix} R(z_i + \Delta L) \\ S(z_i + \Delta L) \end{pmatrix} = \begin{pmatrix} t_{11} & t_{12} \\ t_{21} & {}_{22} \end{pmatrix} \begin{pmatrix} R(z_i) \\ S(z_i) \end{pmatrix} = T_i \begin{pmatrix} R(z_i) \\ S(z_i) \end{pmatrix}. \tag{3.10}$$

where i=1, 2, 3,..., N,

$$t_{11} = t_{22}^{\ *} = \cos\left(\Delta L \sqrt{\kappa(z_i)^2 + \delta^2}\right) + j\delta \frac{\sin\left(\Delta L \sqrt{\kappa(z_i)^2 + \delta^2}\right)}{\sqrt{\kappa(z_i)^2 + \delta^2}}, \tag{3.11}$$

$$t_{12} = t_{21} = -j\kappa \frac{\sin\left(\Delta L \sqrt{\kappa(z_i)^2 + \delta^2}\right)}{\sqrt{\kappa(z_i)^2 + \delta^2}}. \tag{3.12}$$

T_i is an unitary matrix and by the law of energy conservation

$$S^*(z)S(z)+R^*(z)R(z)=1. \tag{3.13}$$

Therefore, the solution for the whole sections of the coupler is

$$\begin{pmatrix} R(L) \\ S(L) \end{pmatrix} = T_N \cdots\cdots T_3 T_2 T_1 \begin{pmatrix} R(0) \\ S(0) \end{pmatrix} = \prod_{i=1}^{N} T_i \begin{pmatrix} R(0) \\ S(0) \end{pmatrix}. \tag{3.14}$$

C. Iterative Newton's Method

In order to correct for the inaccuracy of the Fourier transform method, the transfer matrix method is corrected by the Newton's method [3-9]. The concept of this method is to define the coupling function as a linear combination of reference couplings and the correction.

$$\kappa(z)=\kappa_{ref}(z)+p(z). \tag{3.15}$$

where κ is the corrected coupling function, κ_{ref} is a reference coupling, and p is the correction parameter viewed as a perturbation. The Newton's method starts from the first order Tayler series expansion of the transfer matrix to obtain a set of linear equations.

$$S_i(\mathrm{K}+P)\approx S_i(\mathrm{K})+\sum_{j=1}^{N}\frac{\partial S_i(\mathrm{K})}{\partial \kappa_j}p_j. \tag{3.16}$$

where i=1,2,3,…,M, and K and P are the vectors of κ and p, respectively.

The actual first order Tayler series expansion of the transfer matrix is as follows:

$$\begin{aligned} T_i &= T_i^0 + V_i p_i \\ &= \begin{pmatrix} t_{11} & t_{12} \\ t_{21} & t_{22} \end{pmatrix} + \begin{pmatrix} v_{11} & v_{12} \\ v_{21} & v_{22} \end{pmatrix} p_i \end{aligned} \tag{3.17}$$

where

$$t_{11} = t_{22}^{\ *} = \cos\left(\Delta L\sqrt{\kappa_{ref}(z_i)^2 + \delta^2}\right) + j\delta\frac{\sin\left(\Delta L\sqrt{\kappa_{ref}(z_i)^2 + \delta^2}\right)}{\sqrt{\kappa_{ref}(z_i)^2 + \delta^2}}, \tag{3.18}$$

$$t_{12} = t_{21} = -j\kappa_{ref}(z_i)\frac{\sin\left(\Delta L\sqrt{\kappa_{ref}(z_i)^2 + \delta^2}\right)}{\sqrt{\kappa_{ref}(z_i)^2 + \delta^2}}, \tag{3.19}$$

$$v_{11} = v_{22}^{\ *} = -\frac{\sin\left(\Delta L\sqrt{\kappa_{ref}(z_i)^2 + \delta^2}\right)\Delta L\kappa_{ref}(z_i)}{\sqrt{\kappa_{ref}(z_i)^2 + \delta^2}}$$

$$+ j\delta\frac{\kappa_{ref}(z_i)}{\kappa_{ref}(z_i)^2 + \delta^2}\left\{\Delta L\cos\left(\Delta L\sqrt{\kappa_{ref}(z_i)^2 + \delta^2}\right) - \frac{\sin\left(\Delta L\sqrt{\kappa_{ref}(z_i)^2 + \delta^2}\right)}{\sqrt{\kappa_{ref}(z_i)^2 + \delta^2}}\right\}, \tag{3.20}$$

$$v_{12} = v_{21} = -j\frac{\sin\left(\Delta L\sqrt{\kappa_{ref}(z_i)^2 + \delta^2}\right)}{\sqrt{\kappa_{ref}(z_i)^2 + \delta^2}}$$

$$- j\frac{\kappa_{ref}^2(z_i)}{\kappa_{ref}(z_i)^2 + \delta^2}\left\{\Delta L\cos\left(\Delta L\sqrt{\kappa_{ref}(z_i)^2 + \delta^2}\right) - \frac{\sin\left(\Delta L\sqrt{\kappa_{ref}(z_i)^2 + \delta^2}\right)}{\sqrt{\kappa_{ref}(z_i)^2 + \delta^2}}\right\}. \tag{3.21}$$

From equation (3.14) and (3.17), the transfer matrix is

$$T = T_N \cdots\cdots T_3T_2T_1 = \left(T_N^0 + V_N p_N\right)\cdots\cdots\left(T_3^0 + V_3 p_3\right)\left(T_2^0 + V_2 p_2\right)\left(T_1^0 + V_1 p_1\right)$$

$$= T_N^0T_{N-1}^0 \cdots\cdots T_2^0T_1^0$$

$$+ \left(V_N T_{N-1}^0 \cdots\cdots T_2^0T_1^0 p_N + T_N^0V_{N-1}T_{N-2}^0 \cdots\cdots T_1^0 p_{N-1} + \cdots\cdots + T_N^0T_{N-1}^0 \cdots\cdots T_2^0V_1 p_1\right)$$

$$= \prod_{j=1}^{N} T_j^0 + \sum_{i=1}^{N}\frac{\partial\prod_{j=1}^{N} T_j^0}{\partial\kappa_i} p_i = T^0 + \sum_{i=1}^{N}\frac{\partial T^0}{\partial\kappa_i} p_i$$

$$= T^0 + \sum_{i=1}^{N}\frac{\partial T^0}{\partial\kappa_i} p_i \ . \tag{3.22}$$

The recursive algorithm to calculate T^0 and $\sum_{i=1}^{N} \frac{\partial T^0}{\partial \kappa_i} p_i$ is as follows:

$$A_1 = V_1 p_1, \qquad B_1 = T_1^0,$$

$$A_{i+1} = T_{i+1}^0 A_i + V_{i+1} B_i p_{i+1}, \qquad B_{i+1} = T_{i+1}^0 B_i . \tag{3.23}$$

where A_N and B_N are equal to $\sum_{i=1}^{N} \frac{\partial T^0}{\partial \kappa_i} p_i$ and T^0, respectively.

For the directional coupler modulator, the response function S is obtained as

$$S(\delta, \mathrm{K}) = \begin{pmatrix} 0 & 1 \end{pmatrix} T \begin{pmatrix} 1 \\ 0 \end{pmatrix}. \tag{3.24}$$

Therefore, the first order Tayleor's expansion of S is

$$S(\delta, \mathrm{K}) = S^0(\delta, \mathrm{K}) + \sum_{j=1}^{N} \frac{\partial S^0(\delta, \mathrm{K})}{\partial \kappa_j} p_j . \tag{3.25}$$

The matrix equation for the p_j can be solved by the direct matrix inversion method or the least square fit method, and p_j is solved by this iterative procedure. The updated coupling function for the iteration is

$$\kappa_{new}(z) = \kappa_{old}(z) + p(z). \tag{3.26}$$

The iteration is repeated until $\left\| S - S^0 \right\|$ reaches a minimum value.

The above method has been applied to design the coupler modulator which has the response function shown in figure 3-4 and written as follows:

$$|S(\delta)| = \begin{cases} 1 & |\delta| \le 0.8 \\ \sqrt{1 - (|\delta| - 0.8)/0.2} & 0.8 \le |\delta| \le 1 \\ 0 & |\delta| > 1 \end{cases} . \tag{3.27}$$

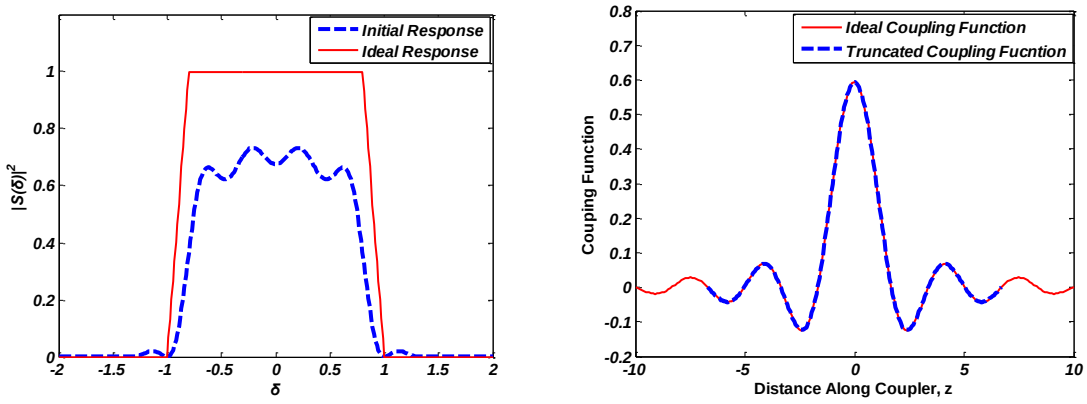

(a) (b)

Figure 3-4: The red lines of (a) and (b) are the ideal intensity response function and coupling coefficient and the blue dash lines of (a) and (b) are the initial intensity response function and coupling coefficient.

The red lines in figure 3-4 (a) and (b) are the expected intensity response function and coupling function calculated by inverse Furier transform, respectively. The blue dashed lines in figure 3-4 (b) and (a) are the truncated coupling function and the initial intensity response obtained by using truncated coupling coefficient, respectively.

Since the initial guess of the intensity response does not fit the expected response, the iteration method should be used to obtain correct response. The coupling function for the desired response function is also obtained by the iteration.

By using the iteration method the coupling coefficient and the response function approaches the required response function, respectively, as shown in figure 3-5 (a) and (b).

The perturbation term, *p*, in the equation (3.26) has also decreased during the iteration as shown in figure 3-6.

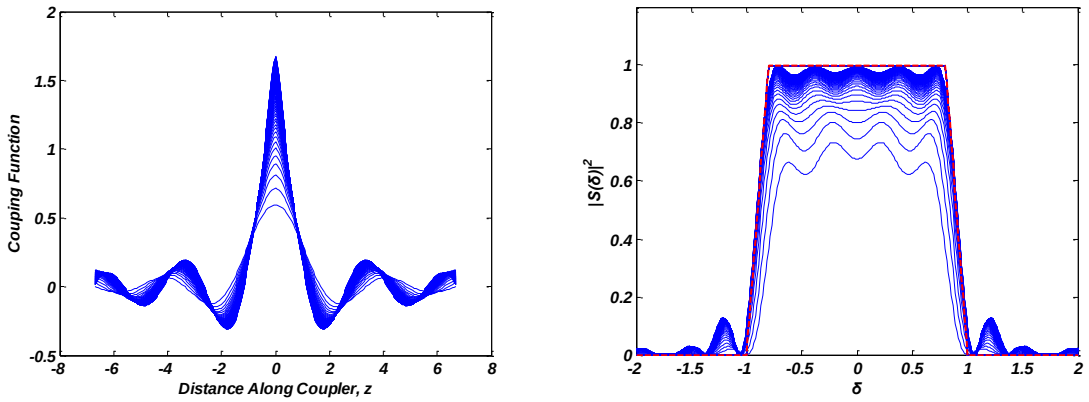

(a) (b)

Figure 3-5: The (a) coupling function and (b) corresponding response function for 100 steps of the iterative Newton's method. Each step improves the fit of the response (solid lines) to the desired response (dotted line).

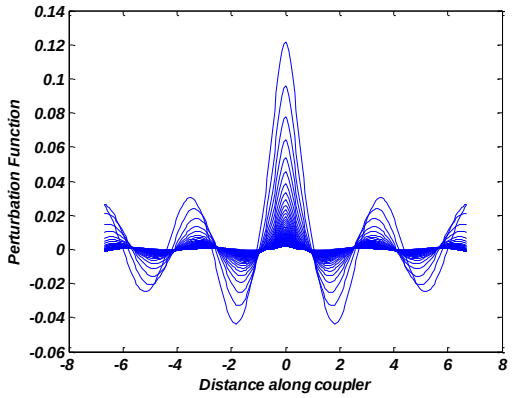

Figure 3-6: The perturbation term of the coupling function, *p*, during the iteration.

The slope, or switching, region of the modulator response is more important than any other regions because it is used for biasing for the linear operation of the modulator. The 100 iterated response function and the best fitted response functions by 17 iteration to the slope region, which are the black lines, are shown in figure 3-7 (a) and (b), respectively.

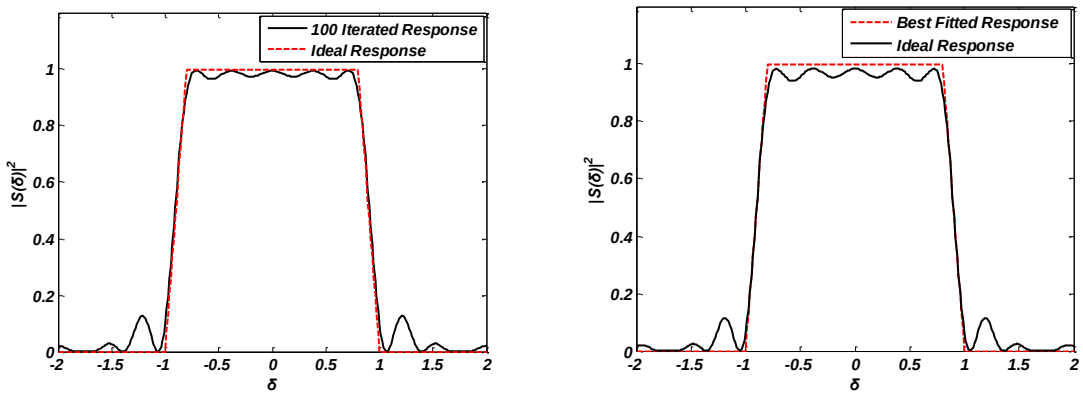

(a) (b)

Figure 3-7: The response functions (a) after 100 iteration (B) of the best fit at slop region.

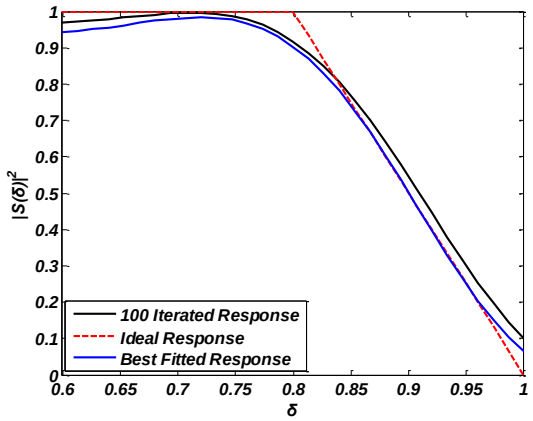

Figure 3-8: The enlarged response functions of 100 iterated response and best fitted response functions.

Figure 3-8 shows the comparison between the blue line for the best fitted response function and the black line for 100 iterated response function. The red dashed line is the ideal response function.

From the above comparison, although the iterative Newton's method builds a much better fit of the desired response than the Fourier transform method, it has one significant problem that it attempts to minimize the total error between desired and calculated response, rather than preferentially improving the linear portion.

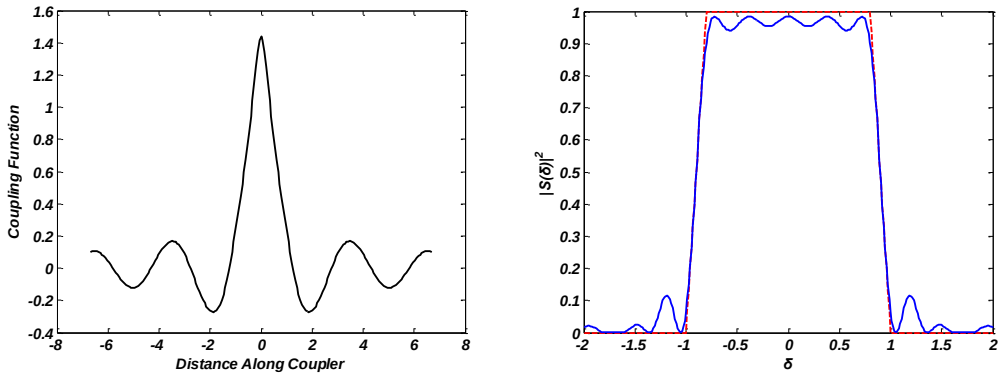

(a) (b)

Figure 3-9: The best fitted version of (a) the variable coupling coefficient (b) the intensity response function.

The iteration attempts to match the horizontal regions of the response rather than improve the fit in the sloped section. As a result the linearity of the response suffers in order to fit less important regions. The fit in the sloped section version of the coupling function and response function are shown in figure 3-9.

D. Iterative Newton's Method with Weighted Error

The iterative Newton's method was modified to fit the linear region, or sloped section, of the response preferentially, so that the linearity would be improved as well as the fit of the rest of the response. This involved a simple modification to the method which weights the error between calculated and desired response most heavily in the center of the sloped region, and less heavily farther from this point. The weight factors are added in equation (3.25)

$$S(\delta,\mathrm{K}) = S^{0}(\delta,\mathrm{K}) + \sum_{j=1}^{N} W(\delta)\frac{\partial S^{0}(\delta,\mathrm{K})}{\partial \kappa_{j}} p_{j} \qquad (3.28)$$

where W(δ) is the weight vector which has the length same length as that of S.

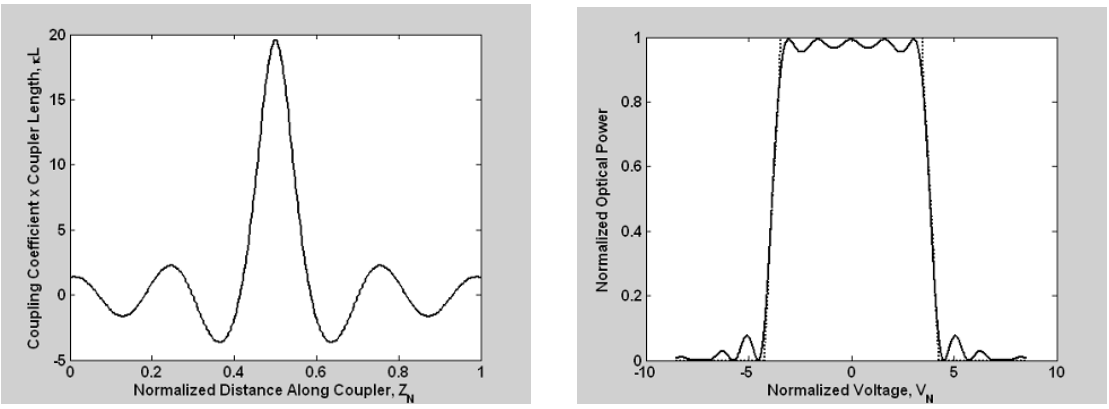

Figure 3-10: (a) Coupling function for the improved modulator design. (b) Response function for the improved modulator design (solid line) and the target response (dotted line).

Since the iterative Newton's method attempts to minimize the total error, weighting causes it to improve both the linear region and the rest of the response. This is a substantial improvement to the preferred synthesis method because it allows variable coupling directional coupler modulators with greater response linearity. The response function and coupling function are shown in figure 3-10.

As intended, the fit is very good in the linear portion of the response, and error is tolerated in the other less important regions. Comparing to the previous design synthesized without weighting as shown in figure 3-9, it can be seen that the fit along the linear region of the response is significantly improved with the weighted method.

The synthesized coupling function for this modulator is shown in figure 3-10. Note that the coupling function changes sign several times along the length of the coupler. This can be achieved in practice by placing a 180° optical phase shift section at each sign change along the coupler [3-10]. Each phase shift section delays the light in one waveguide with respect to the other by one-half period.

The common method to obtain optical phase shift section is building different path length between two identical waveguides [3-1] as shown in figure 3-11 (a). This method is complicated to fabricate the exact length of the bent sections and the radius of the sections needs to be considered to reduce the bending loss. Even with correct design, the fabricated phase change sections show considerable loss.

A new design of the phase shift section is shown in figure 3-11 (b), which uses a different waveguide width over the phase shift section as shown in figure 3-11 (b). This design obtains the phase shift by varying the width of one waveguide of the coupler to obtain a new propagation constant given by β_1, and the difference between the constant width propagation constant β is $\Delta\beta=\beta-\beta_1$, then

$$\phi = \int_0^{\Delta l} \Delta\beta dz = \Delta\beta\Delta l \,. \tag{3.29}$$

This new design is simpler and easier to fabricate. In addition, not only a π-phase shift but also variable phase shifts are easily fabricated by adjusting waveguide width or length over the phase shift section. However, this design has a disadvantage which is the transmission loss between narrow waveguide section and normal waveguide sections in one waveguide.

Figure 3-11: π phase shift with (a) different length and (b) different width.

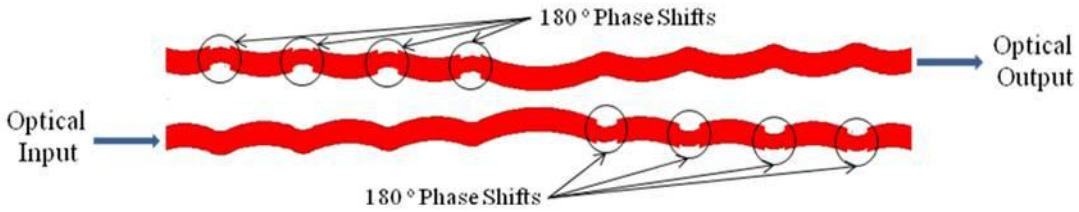

Figure 3-12: The variable coupling directional coupler with 8 π phase shifts.

The final schematic design of the variable coupling directional coupler with π phase shifts is shown in figure 3-12.

3.3 Uniform Coupler Modulator with Negative Coupling Regions

3.3.1 Proposed Design

From the previous variable coupling directional coupler design, the variable amplitude and negative coupling may increase the linearity of the modulator, however, loss is a major factor. In the present design, the phase shifts and negative coupling sections are inserted in the uniform directional coupler to obtain linearity. The coupling coefficient of the proposed directional coupler modulator is shown in figure 3-13. This modulator has uniform coupling but negative coupling in two specific regions. A schematic diagram of the proposed directional coupler for the highly linear electrooptic modulator is shown in figure 3-14. This coupler has two identical, parallel optical waveguides and includes four phase shifts. These four phase shifts create two negative coupling sections and have been located at specific positions along the length of the device to obtain high linearity.

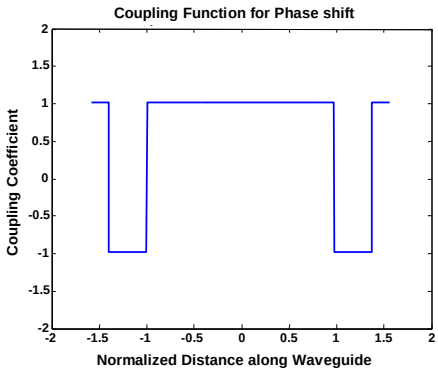

Figure 3-13: The Coupling coefficient of the directional coupler modulator with four π phase shifts.

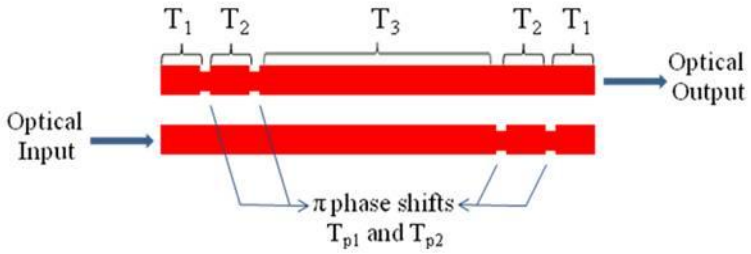

Figure 3-14: The directional coupler with four π phase shifts.

Two negative coupling sections are realized by four π phase shifts as shown in figure 3-14. In this coupler modulator design, the different width solution is applied for phase shift sections. Each phase shift section delays the light in one waveguide with respect to the other by one-half period, producing a 180° relative phase shift. The total coupler length is twice the original directional coupler length, and the optimum response is determined by the correct phase shift positions and these positions are placed symmetrically.

To choose the correct location of the phase shifts of the modulator, a coarse search approach was used. This divided the coupler into *m* sections of uniform length, and checked every possible placement of the *n* phase shifts at the ends of these sections,

given the initial condition $|R(0)|^2 = 1$. In each case the phase shifts were placed symmetrically about the center of the coupler, which was found to keep the phase response constant, and therefore prevent signal chirp. A least-square fit of the intensity response of each design was used to estimate its linearity, and to find the most linear designs. This was done systematically for different device lengths from L_C to $4L_C$, in increments of $0.1L_C$, and for different numbers of sections, from 34 to 64. The analysis was performed for two, four and six phase shifts placed symmetrically along the length of the coupler. Although a number of designs resulted in relatively linear response over the region $0.05 \leq |S|^2 \leq 0.95$, one design exhibited superior linearity, without a great reduction in switching efficiency. The positions of the phase shifts for this design were optimized further to minimize signal distortions, as calculated in Section 3.3.2, using a Nelder-Mead algorithm [3-7].

3.3.2 Design optimization

The response function of the directional coupler modulator was obtained using a transfer matrix approach. The optical field of the light wave after propagating a specific length, l, of the directional coupler is [3-9]

$$\begin{pmatrix} R(l) \\ S(l) \end{pmatrix} = \begin{pmatrix} t_{11} & t_{12} \\ t_{21} & {}_{22} \end{pmatrix} \begin{pmatrix} R_0 \\ S_0 \end{pmatrix}, \tag{3.30}$$

$$t_{11} = t_{22}^{\ *} = \cos\left(l \cdot \sqrt{\kappa^2 + \delta^2}\right) + j\delta \frac{\sin\left(l \cdot \sqrt{\kappa^2 + \delta^2}\right)}{\sqrt{\kappa^2 + \delta^2}}, \tag{3.31}$$

$$t_{12} = t_{21} = -\frac{j\kappa \sin\left(l \cdot \sqrt{\kappa^2 + \delta^2}\right)}{\sqrt{\kappa^2 + \delta^2}}. \tag{3.32}$$

where R_0 and S_0 are the normalized input optical field to the two waveguides and $R(l)$ and $S(l)$ are the output field from the two waveguides after propagation of length, l. κ is the coupling coefficient and δ is the difference of the propagation constant between two waveguides, which is linearly proportional to applied voltage [3-13].

The transfer matrices for the phase shifts are defined as following.

$$T_{ps1} = \begin{bmatrix} e^{-j\theta} & 0 \\ 0 & 1 \end{bmatrix} \quad or \quad T_{ps2} = \begin{bmatrix} 1 & 0 \\ 0 & e^{-j\theta} \end{bmatrix}. \tag{3.33}$$

where T_{ps1} and T_{ps2} are the transfer matrices for the one waveguide and the other waveguide, respectively, and θ is the phase delay by the phase shift section, which is equal to π in this design. As shown in figure 3-14, the first two phase shift sections are placed on one waveguide and the other two are on the other waveguide because the input light propagates and fully transfers from one waveguide to the other waveguide, and is made not to pass the phase shifts section directly to avoid coupling loss. The phase shift sections were placed symmetrically about the center of the coupler, which was found to keep the phase response constant and prevent signal chirp.

The transfer matrix of the directional coupler modulator with four π-phase shifts is defined by five transfer matrices with different length for normal directional coupler and four transfer matrices for the phase shift sections. The each section is represented by its own transfer matrix as shown in figure 3-14 and the whole transfer matrix, T, and the power intensity response $|S(L_c)|^2$ are obtained by their cascade multiplication.

$$\begin{pmatrix} R(L_c) \\ S(L_c) \end{pmatrix} = T \cdot \begin{pmatrix} R(0) \\ S(0) \end{pmatrix}, \tag{3.34}$$

$$T = T_1 \cdot T_{ps2} \cdot T_2 \cdot T_{ps1} \cdot T_3 \cdot T_{ps1} \cdot T_2 \cdot T_{ps1} \cdot T_1 . \tag{3.35}$$

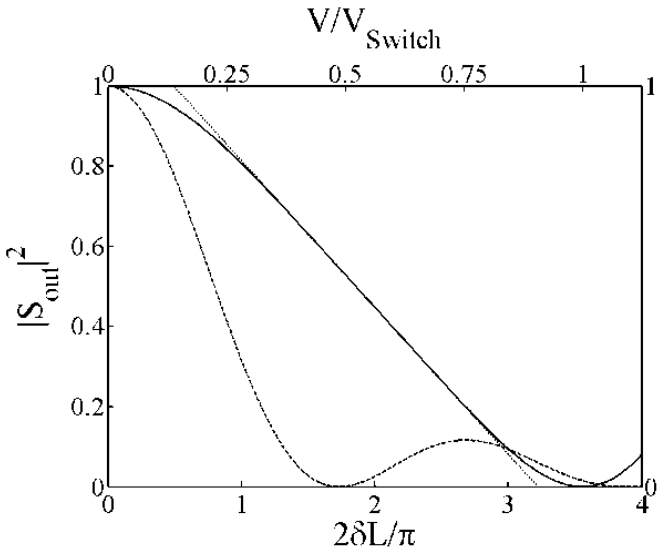

Figure 3-15: Intensity response of the phase-shifted directional coupler modulator (solid line), and intensity response of the conventional directional coupler modulator (dashed line).

where $R(0)=1$ and $S(0)=0$ and L_c is the coupling length. $R(L_c)$ and $S(L_c)$ are the output optical fields from the end of the directional coupler.

The directional coupler modulator has total length L_c, which is the twice the length of the conventional directional coupler, and the phase shift sections are placed optimally at positions of 5.933%, 18.617%, 81.383% and 94.067% along the length of the coupler The intensity response for this design is shown in figure 3-15, plotted versus $2\delta L/\pi$ on the lower axis, and in normalized coordinates V/V_{switch} on the upper axis. The region $0.3 \leq |S|^2 \leq 0.6$ was fitted to a straight line as shown to illustrate that this region was essentially linear. The value of $2\delta L/\pi$ to switch the modulator was 3.54, as compared to $\sqrt{3}=1.73$ for the simple directional coupler. For comparison, the response of the conventional directional coupler modulator [3-11] is also included in figure 3-15. This shows that the modulator with phase shifts offers greater response linearity, but at some expense in switching efficiency.

Table 3-1: The fundamental signal and distortion components.

Fundamental signal	$H(f_1,0),\ H(0,f_2)$
Second harmonics	$H(2f_1,0),\ H(0,2f_2)$
Second order intermodulation distortion	$H(f_1,f_2),\ H(f_1,-f_2)$
Third order intermodulation distortion	$H(2f_1,f_2), H(2f_1,-f_2),\ H(f_1,2f_2),$ $H(-f_1,2f_2)$

3.4 Linearity Analysis

The common way to evaluate the linearity of the modulator response is the two-tone test. As discussed in Chapter 2, when the optical signal is modulated by two different RF signals with same amplitude, the output of the modulated optical signal has fundamental signal components and distortion products including harmonics and intermodulation terms and these are listed in Table 3-1. The spurious free dynamic range (SFDR) of device is determined by

$$SFDR = \frac{P_{Input}\Big|_{P_{Distortion}=P_{Noise}}}{P_{Input}\Big|_{P_{Fundamental Signal}=P_{Noise}}}. \qquad (3.36)$$

where P_{Noise} is the noise power as it was defined in chapter 2, which includes the sum of the thermal, shot and relative intensity noise of the link.

$$P_{noise} = GkTB + \frac{1}{2}qI_dRB + \frac{1}{4}I_d^2RB\cdot RIN + kTB. \qquad (3.37)$$

where G is RF-photonic link gain, k is Boltzmann's constant, T is temperature, B is the measurement bandwidth, I_d is the dc photocurrent, and $R=R_s=R_{load}=50\ \Omega$. The first term is the input thermal noise, the second term is photodetector shot noise, the third term is

the RIN in the laser output and the fourth term is the thermal noise from the photodetector termination impedance.

The link gain is obtained by

$$G = \frac{1}{4}\left(P_L(1-L_o)\eta_D R \frac{\partial S^2}{\partial V}\bigg|_{V_{Bias}} \right)^2 . \tag{3.38}$$

where L_o is the total optical loss, η_D is the receiver's responsivity, and S^2 is the intensity response of the modulator.

Each power of the distortion component which are obtained by FFT explained in Chapter 2 is calculated as

$$P_{Fundamental} = P_o \cdot |H(f_1,0)|^2 = P_o \cdot |H(0,f_2)|^2 , \tag{3.39}$$

$$P_{2nd-Harmonic} = P_o \cdot |H(2f_1,0)|^2 = P_o \cdot |H(0,2f_2)|^2 , \tag{3.40}$$

$$P_{IMD2} = P_o \cdot |H(f_1,f_2)|^2 = P_o \cdot |H(f_1,-f_2)|^2 , \tag{3.41}$$

$$P_{IMD3} = P_o \cdot |H(2f_1,f_2)|^2 = P_o \cdot |H(2f_1,-f_2)|^2 ,$$

$$= P_o \cdot |H(f_1,2f_2)|^2 = P_o \cdot |H(-f_1,2f_2)|^2 . \tag{3.42}$$

Where P_0 is defined as

$$P_0 \equiv \frac{R_L}{4}\{P_L(1-L_o)\eta_D\}^2 . \tag{3.43}$$

The spur free dynamic range (SFDR) of the modulators is illustrated graphically in figures 3-16, which plots the RF output power versus RF input power in *dBm* at the optimal bias voltage for the maximum SFDR.

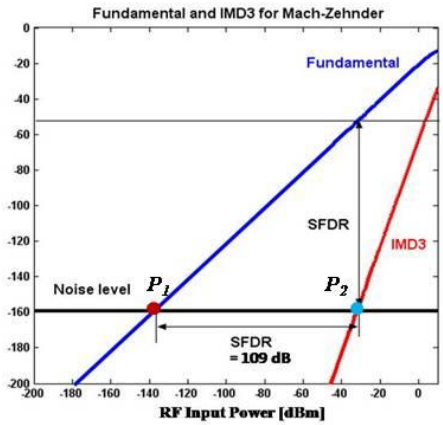

Figure 3-16: The two tones SFDR calculation of Mach-Zehnder modulator. P_1 and P_2 are $P_{Input}\big|_{P_{FundamentalSignal}=P_{Noise}}$ and $P_{Input}\big|_{P_{Distortion}=P_{Noise}}$ in equation (3.36) , respectively.

The spur free dynamic range is the horizontal distance between P_1 and P_2 in figure 3-16, which are the intersections of the noise floor with the distortion and fundamental power lines, respectively. The parameters for the SFDR calculation is give in Table 3-2. SFDR calculations with the parameters in Table 3-2 are performed for various modulator design in the next sections.

Table 3-2: Fiber-optic link parameters.

Parameter	Symbol	Value
Laser Power	P_L	0.1 W
Laser Noise	RIN	-165 dB/Hz
Total Optical Loss	L_O	0.9
Modulator Sensitivity	V_{Switch}	10 V
Modulator Impedance	R_M	50 Ω
Detector Responsivity	r_D	0.7 A/W
Detector Termination	R_T	50 Ω
Load Impedance	R_L	50 Ω
Noise Bandwidth	B	1 Hz

3.4.1 Trapezoidal Response case

The curve, in figure 3-17 (a), is the coupling function for trapezoidal response. In Figure 17 (b), the dashed-line is the desired response and solid line is the obtained response from the coupling function in figure 3-17 (a) by the iterative method.

The second harmonic and third harmonic are shown in figure 18 (a) and IMD2 and are shown in figure 3-18 (b). From figure 3-18 (a) and (b), the third harmonic is a little higher than IMD3 and the second harmonic and IMD2 have the same values, but the peak value of the second harmonic is higher than the corresponding IMD2 peak value.

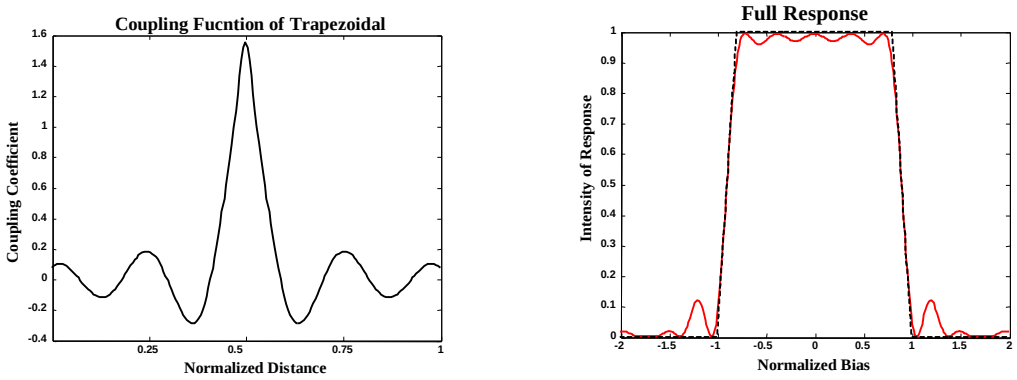

(a) (b)

Figure 3-17: (a) Coupling Coefficient (b) Full Response for the Original Trapezoidal case.

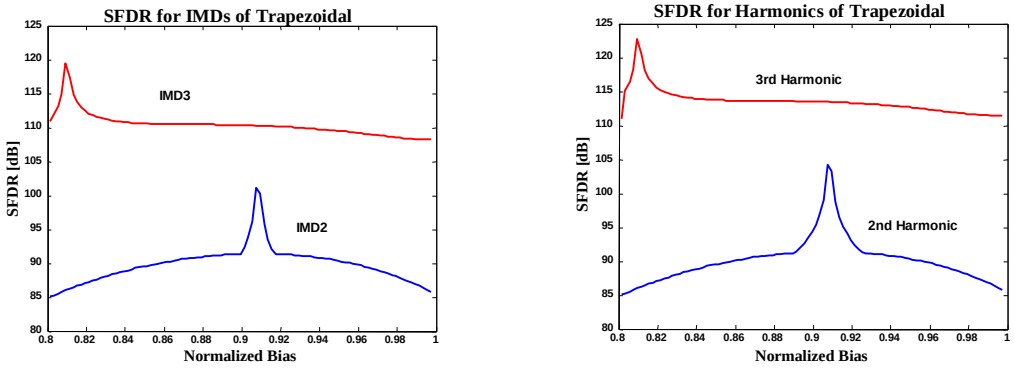

(a) (b)

Figure 3-18: (a) SFDR for IMD2 and IMD3 (b) SFDR for the Second Harmonic and the Third Harmonic for Trapezoidal Response.

3.4.2 Uniform directional coupler with negative coupling

Figure 3-19 shows the locations of the phase shifts in the directional coupler design with constant coupling coefficient over the entire device length with four phase shifts, and the response is shown in figure 3-19 (b). The SFDRs for IMDs and harmonics from this response are shown in figure 3-20. The maximum value of third harmonic is higher than the peak value of the IMD3 and the maximum value of IMD2 is higher than the peak value of second harmonic. When the bias voltage for the maximum SFDR is applied, which is V/V_{Switch} = 0.5456, the SFDRs are 130 dB/Hz$^{2/3}$ and 125.7 dB/Hz$^{1/2}$. Figure 3-20 (b) shows the overall SFDR which is 125.7 dB.

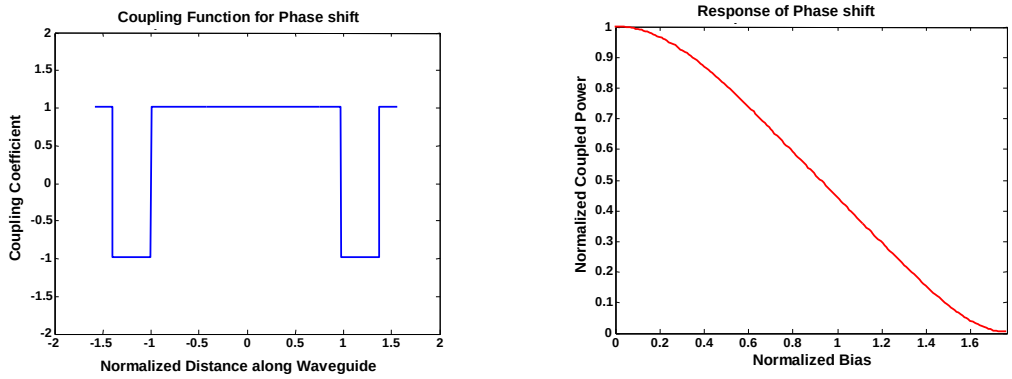

(a) (b)

Figure 3-19: (a) Coupling coefficient which changes sign at each pi-phase shifter, otherwise coupling is uniform (b) response for a constant directional coupler with pi-phase shifters along the optical waveguides.

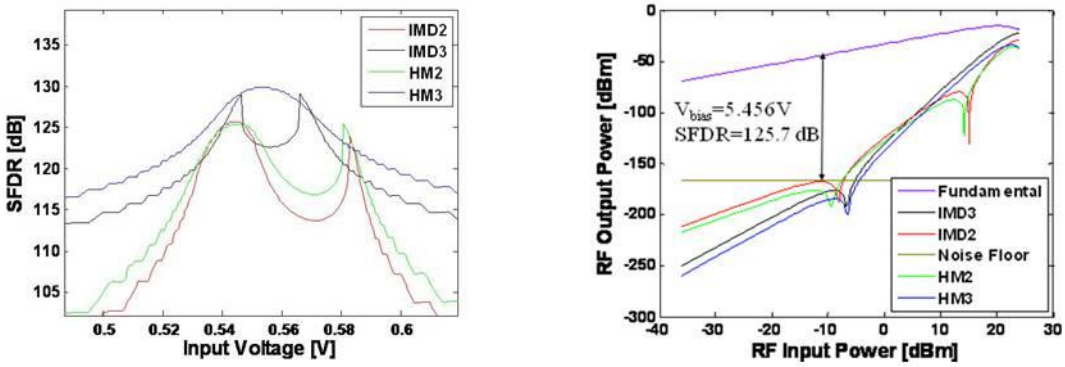

(a) (b)

Figure 3-20: (a) SFDR for the harmonics and IMDs along the varied bias voltages and (b) overall SFDR of harmonics and IMDs as functions of the RF input power.

3.4.3 Triangular Response case

A typical linear response function shape is triangular. The coupling and the response functions are shown in figure 3-21. The dotted line in figure 3-21 (b) is the desired response and the solid line is the designed response. The difference with trapezoidal case is that the center region of the coupling is higher than that of the trapezoidal coupling coefficient, and rest of region of the coupling coefficient is lower than that of the trapezoidal coupling coefficient.

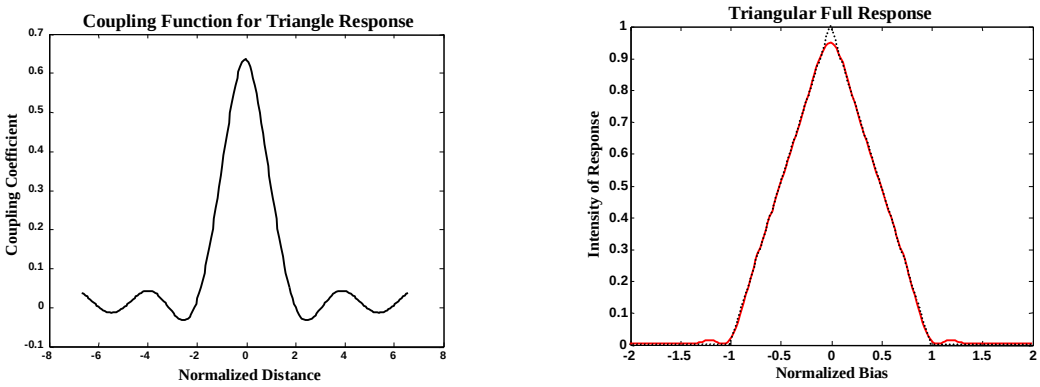

(a) (b)

Figure 3-21: (a) Coupling Coefficient (b) Full Response for the Triangular case.

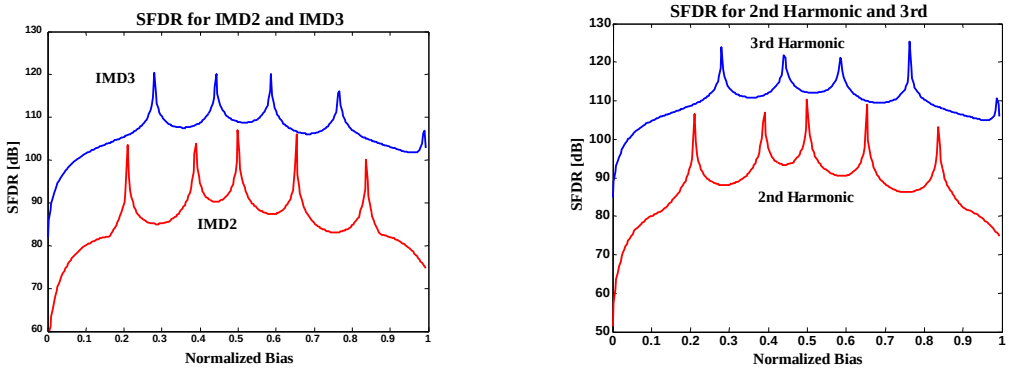

(a) (b)

Figure 3-22: (a) SFDR for IMD2 and IMD3 (b) SFDR for the Second Harmonic and the Third Harmonic for Triangular Response.

Table 3-3: Performance of fiber-optic links with parameters of Table 3-1.

Modulator Type	SFDR for IMD3 ($dB/Hz^{2/3}$)
Directional Coupler with Negative Coupling	130
Trapezoidal Response Variable Directional Coupler	110
Triangle Response Variable Directional Coupler	109.9
Conventional Directional Coupler	109
Single Mach-Zehnder (MZ)	109.9
Dual MZ ("Cubic")	126.2
Series Directional Coupler (2 Bias Sections, "Cross")	127.1

IMD3 and IMD2 calculations for the Triangular response shows that IMD2 and IMD3 are reduced at several dc bias points. From figure 3-22 (a) and (b), the third Harmonic and the second Harmonic are a little higher than IMD3 and IMD2, respectively. However, the peak values of the second Harmonic and IMD2 are the same, but do not coincide with the peak values of SFDR of third harmonic and IMD3.

The link parameters in Table 3-2 are those used previously to compare distortion in different modulator designs [3-14~3-15], and therefore allow the various directional coupler modulators to be included in the comparison. This has been done in Table 3-3, which lists link properties for various modulator designs.

It can be seen that the directional coupler with negative coupling offers a significant improvement of 12-16 dB in SFDR compared to the Mach-Zehnder and conventional directional coupler modulators, which is comparable to the best linearized modulator designs. However, this modulator design offers some expense in switching efficiency as shown in figure 15.

Table 3-4: Voltage and coupler length products.

Modulator Design	$GaAs/Al_{0.2}Ga_{0.8}As$ V_sL(V·cm)	$LiNBO_3$ V_sL(V·cm)
Trapezoidal Coupler	12.47	7.37
π-Phase Shift Coupler	18.7	11.05
Conventional Directional Coupler	9.04	5.34
Mach-Zehnder	5.19	3.07

3.5 Switching Voltage

The calculated switching voltage length products for the various modulators are given below in the Tables 3-4 which is used in Chapter 2. The switching voltage length product for these two modulators, in GaAs and $LiNBO_3$, are separately shown in this table.

3.6 Designs for the Variable Phase shifts at Different Locations in the Uniform Coupler Modulator

In the previous section, only the π phase shifts at specific positions for increasing the modulator linearity were considered. The phase shifts sections may also be designed to have other than π phase delay, and in this section, the variable phase delay sections and their positions in the uniform coupler modulator will be briefly discussed.

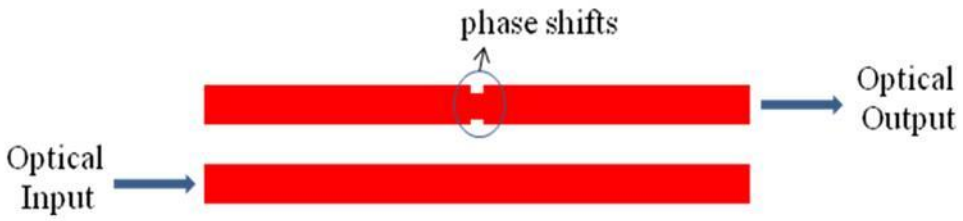

Figure 3-23: The schematic design of the uniform directional coupler modulator with one phase shift section.

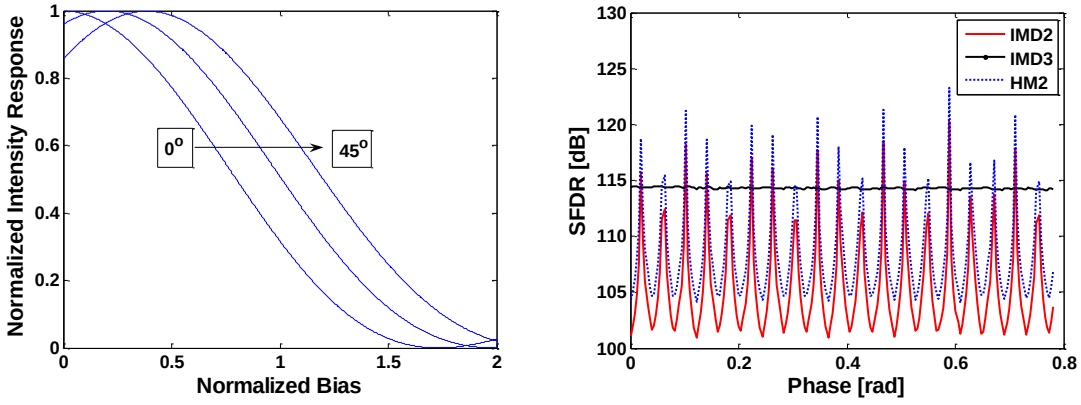

(a) (b)

Figure 3-24: (a) Intensity response and (b) the second harmonic, IMD3, and IMD2 with varying the phase from 0° to 45°.

3.6.1 One phase shift in center of the device

The schematic design of the device is shown in figure 3-23. The phase shift section is located at the center along the uniform directional coupler modulator length, and the phase delay is varied.

If the phase delay is less than π, the coupling function is not real but becomes complex varying in both amplitude and phase. Therefore, the response function will be changed as well. The intensity response functions with varied phases are shown in figure 3-24 (a), and the second harmonic, IMD2, and IMD3 responses are shown in figure 3-24 (b). When the phase is changed from 0° to 45°, the response function is shifted and the SFDR of second harmonic and IMD2 increases and decreases below the SFDR of IMD3

which is 114 dB. Therefore, the SFDR at specific phase delay of this design is larger than conventional directional coupler modulator and Mach-Zehnder modulator, and the switching voltage is equal to conventional uniform coupler modulator.

As shown in figure 3-24 (b), the variation of the second harmonic and IMD2 are periodic. The study of the characteristic of the periodicity and other designs which has two, three, and four phase shift sections will be left for the future investigation.

3.7 References

[3-1] C. Laliew, S. W. Lovseth, X. Zhang, and A. Gopinath, “A Linearized Optical Directional Coupler Modulator at 1.3 μm,” *IEEE J. Lightwave Technology*, vol. 18, pp. 1244-9, September 2000.

[3-2] G. H. Song and S. Y. Shin, "Design of corrugated waveguide filters by the Gel'fand-Levitan-Marchenko inverse- scattering method," J. Opt. Soc. Am. A, vol. 2, no. 11, pp. 1905-1915, November 1985.

[3-3] R. C. Alferness, “Titanium-diffused lithium niobate waveguide devices,” in *Guided-Wave Optoelectronics*, 2nd ed, T. Tamir, Ed. New York: Springer-Verlag, 1990, pp. 145–206.

[3-4] K. A.Winick, “Design of corrugated waveguide filters by Fourier transform techniques,” *IEEE J. Quantum Electron.*, vol. 26, pp. 1918–1929,Nov. 1990.

[3-5] R. C. Alferness and P. S. Cross, “Filter characteristics of codirectionally coupled waveguides with weighted coupling,” *IEEE J. Quantum Electron.*, vol. QE-14, pp. 843–847, Nov. 1978.

[3-6] M. G. Cohen and E. I. Gordon, “Acoustic beam probing using optical techniques,” *Bell Syst. Tech. J.*, vol. 44, no. 4, pp. 693–721, Apr. 1965.

[3-7] Lagarias, J.C. et al, "Convergence Properties of the Nelder-Mead Simplex Method in Low Dimensions," *SIAM Journal of Optimization*, vol. 9, pp. 112-147, 1998.

[3-8] L. W. Couch, II, Digital and Analog Communication Systems, New York: Macmillan, 1993.

[3-9] T. Li, C. Laliew and A. Gopinath, “An iterative transfer matrix inverse scattering technique for synthesis of codirectional optical coupler and filters,” *IEEE J. of Quantum*

Electronics, vol. 38, no. 4, pp. 375-379, April 2002.

[3-10] K. Baek, C. Laliew and A. Gopinath, “ The wavelength dependence of a synthesized electro-optic co-directionalcoupler modulator with π-phase shifters,” *2002 Integrated Photonics Research Technical Digest,* pp. IThD3, July 2002.

[3-11] L. A. Coldren and S. W. Corzine, *Diode Lasers and Photonic Integrated Circuits*, New York: Wiley, 1995.

[3-12] G. M. Kizer, *Microwave Communication*, Ames, IA: Iowa State University Press, 1990.

[3-13] R. C. Alferness, “Waveguide Electrooptic Modulators,” *IEEE Trans. Microwave Theory Tech.*, vol. TMM-30, pp. 1121-1137, August 1982.

[3-14] W. B. Bridges and J. H. Schaffner, “Distortion in Linearized Electrooptic Modulators,” *IEEE Trans. Microwave Theory Tech*., vol. 43, pp. 2184-2197, Sept. 1995.

[3-15] S. A. Hamilton et al, “Comparison of an In-Line Asymmetric Directional Coupler Modulator with Distributed Optical Loss to Other Linearized Electrooptic Modulators,” *IEEE Trans. Microwave Theory Tech*., vol. 47, pp. 1184-1193, July 1999.

CHAPTER 4 Velocity and Impedance Matching Electrode Structure

4.1 Introduction

Traveling-wave type electrodes are required for high frequency operation of external optical modulators to increase the modulation efficiency and bandwidth. It is well known that efficiency and bandwidth of traveling wave electro-optic devices are limited by mismatch of the optical and the electrical phase velocities. The optical phase velocity is constrained by the material indices and the waveguide dimension, which may not be changed. However, the electrical phase velocity may be adjusted for velocity matching. Since the electrical phase velocity of the CPS line is larger than the optical phase velocity of optical waveguides in III-V semiconductor structures, a slow wave electrode structure is required for velocity matching.

There are several studies for the slow wave structures, and most of them are for the coplanar waveguide (CPW) [4-1~4.5] and all of them use shunt capacitor loading. The paper [4-6] has reported using only series inductive sections in CPW. For the CPS case, there are a few studies for shunt capacitive loaded electrodes [4-7].

There are two ways to design the slow wave electrode structure: One is to add only extra shunt capacitive loads, the other is to add extra series inductive and shunt capacitive loads simultaneously. In the first case, CPS with higher characteristic impedance than 50 Ω should be used because extra capacitance decreases the characteristic impedance. However, in the second case, the characteristic impedance of the unloaded line in CPS is maintained at 50 Ω, while adding series inductances and shunt capacitances. When inductance and capacitance values are increased by the same

ratio, the characteristic impedance of the slow wave structure does not change, but the phase velocity of the electrical signals in the structures reduces.

The general equivalent circuit of the normal transmission lines is shown in figure 4-1. In case of lossless circuit, the phase velocity and impedance are given by

$$Z_0 = \sqrt{\frac{L}{C}} \tag{4.1}$$

$$v_m = \frac{1}{\sqrt{LC}} = \frac{c_0}{n_m} \tag{4.2}$$

where c_0 is the microwave velocity in free space, respectively, and n_m is the effective microwave index or microwave refractive index. For the design calculation it is usual to neglect R and G in the expressions for the phase velocity.

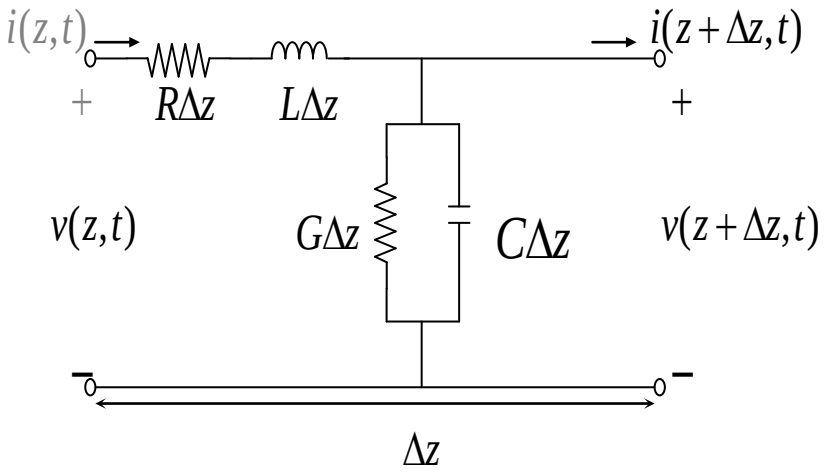

Figure 4-1: The equivalent circuit of a segment of a transmission line with length ΔZ. note that all of R, L, G, and C are distributed components of the line.

4.2 Theory of Periodic Structure

A simple example of the slow-wave electrode structure is a periodic structure with shunt capacitive loads as shown in figure 4-2. In figure 4-2, the length of unit-cell of the periodic structure is l, Z_0 and k are the characteristic impedance and the propagation constant of normal transmission line respectively, and Y is a shunt susceptance of ωC_0. I_n and V_n are the input current and voltage, respectively, and I_{n+1} and V_{n+1} are the output current and voltage, respectively.

The unit-cell of the periodic structure may be considered as a twoport network, and described by the ABCD matrix to obtain the relationship between input and output parameters.

$$\begin{bmatrix} V_n \\ I_n \end{bmatrix} = \begin{bmatrix} A & B \\ C & D \end{bmatrix} \begin{bmatrix} V_{n+1} \\ I_{n+1} \end{bmatrix}. \tag{4.3}$$

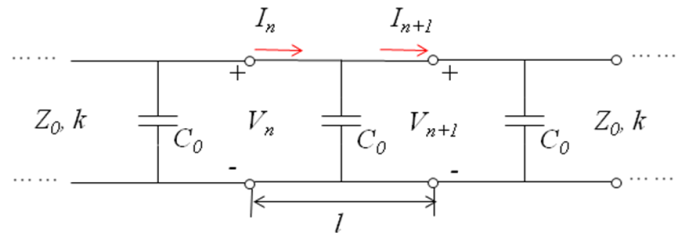

(a)

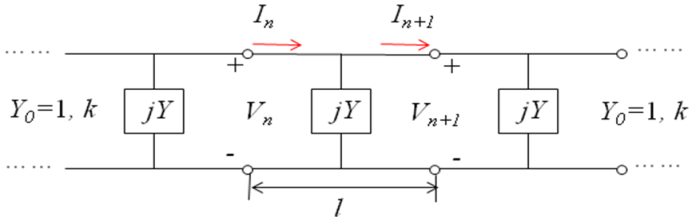

(b)

Figure 4-2: (a) Equivalent circuit of the transmission line with shunt capacitive loads and (b) its normalized form by Z_0.

The unit-cell of the periodic structure consists of two normal transmission line sections, length of which is *l*/2, and a shunt susceptance section in between them. The ABCD matrix, therefore, is obtained by a cascade of three matrices which represents each section as shown in equation (4.4).

$$\begin{bmatrix} A & B \\ C & D \end{bmatrix} = \begin{bmatrix} \cos\frac{kl}{2} & j\sin\frac{kl}{2} \\ j\sin\frac{kl}{2} & \cos\frac{kl}{2} \end{bmatrix} \begin{bmatrix} 1 & 0 \\ js & 1 \end{bmatrix} \begin{bmatrix} \cos\frac{kl}{2} & j\sin\frac{kl}{2} \\ j\sin\frac{kl}{2} & \cos\frac{kl}{2} \end{bmatrix}$$

$$= \begin{bmatrix} \cos\frac{kl}{2} - \frac{s}{2}\sin\frac{kl}{2} & j\left(\sin\frac{kl}{2} + \frac{s}{2}\cos\frac{kl}{2} - \frac{s}{2}\right) \\ j\left(\sin\frac{kl}{2} + \frac{s}{2}\cos\frac{kl}{2} + \frac{s}{2}\right) & \cos\frac{kl}{2} - \frac{s}{2}\sin\frac{kl}{2} \end{bmatrix}. \qquad (4.4)$$

The equation (4.4) is in the normalized form, where the susceptance Y and Z_0 are normalized to Z_0, and replaced by s and 1, respectively. V_n, I_n, V_{n+1}, and I_{n+1} have a following relation as well.

$$V_{n+1} = V_n e^{-\gamma l}, \qquad (4.5)$$

$$I_{n+1} = I_n e^{-\gamma l}. \qquad (4.6)$$

where $e^{-\gamma l}$ is a propagation factor and γ is a propagation constant of the periodic structure, which is $\gamma = \alpha + j\beta$.

Equation (4.3) is modified by using equations (4.5) and (4.6) as following.

$$\begin{bmatrix} V_n \\ I_n \end{bmatrix} = \begin{bmatrix} A & B \\ C & D \end{bmatrix} \begin{bmatrix} V_{n+1} \\ I_{n+1} \end{bmatrix} = e^{\gamma l} \begin{bmatrix} V_{n+1} \\ I_{n+1} \end{bmatrix},$$

$$\begin{bmatrix} A - e^{\gamma l} & B \\ C & D - e^{\gamma l} \end{bmatrix} \begin{bmatrix} V_{n+1} \\ I_{n+1} \end{bmatrix} = 0. \qquad (4.7)$$

For the solution, the determinant of above matrix is zero.

$$AD-(A+D)e^{\gamma l}+e^{2\gamma l}-BC=0. \tag{4.8}$$

Using $AD-BC=1$ and derivation, the equation (4.8) is arranged as follows:

$$\cosh\gamma l=\cos kl-\frac{s}{2}\sin kl. \tag{4.9}$$

The equation (4.9) is the final form of the matrix eigenvalue equation for γ. In the equation (4.9), $\cosh\gamma l$ should be real because right-hand side is real, and α or β of γ should be zero. However, for the wave propagation, only α should be zero. Therefore, γ can be replaced by β as following equation (4.10).

$$\cos\beta l=\cos kl-\frac{s}{2}\sin kl. \tag{4.10}$$

When the length of the unit-cell, l, is much shorter than λ, kd and βl are small, and equation (10) is modified as a equation (11)

$$\cos\beta l\approx 1-\frac{(\beta l)^2}{2}=1-\frac{(kl)^2}{2}-\frac{skl}{2}. \tag{4.11}$$

By definitions of $k=\omega\sqrt{LC}$, $s=\omega C_0\sqrt{(L/C)}$, the β and v_p are obtained as following.

$$\beta=\omega\sqrt{L\left(C+C_0/l\right)}, \tag{4.12}$$

$$v_p=\frac{1}{\sqrt{L\left(C+C_0/l\right)}}. \tag{4.13}$$

From equation (4.13) the periodic structure with the shunt capacitive loads has a slower phase velocity than unloaded electrode structure by C_0/l term.

The characteristic impedance, Z_s, of the unit-cell of the periodic structure with shunt capacitive loadsis defined by equation (4.14)

$$Z_s=Z_0\frac{V_{n+1}}{I_{n+1}}. \tag{4.14}$$

Using the equation (4.7), equation (4.14) is modified as equation (4.15).

$$Z_s = Z_0 \frac{-B}{A - e^{\gamma l}} . \tag{4.15}$$

From equation (4.8), $e^{\gamma l}$ can be solved in terms of *A* and *D*, and A is equal to D for the symmetrical unit-cell. Therefore, the characteristic impedance of the periodic structure with the shunt capacitive loads is obtained as equation (4.16).

$$Z_s = Z_0 \sqrt{\frac{B}{C}} . \tag{4.16}$$

Finally, the characteristic impedance of periodic structure with the shunt capacitive loads is expressed as the equation (4.17).

$$Z_s = \sqrt{\frac{L}{(C + C_0 / l)}} . \tag{4.17}$$

From above derivation, when the shunt capacitive loads are added, the periodic structure has slower phase velocity and smaller characteristic impedance than unloaded electrode structure. Therefore, the unloaded transmission line with higher impedance than 50 Ω is needed for designing the slow-wave structure with the shunt capacitive loads in III-V substrate material.

The next case is the series inductive and shunt capacitive loaded periodic structure. The unit-cell of this structure is shown in figure 4-3. In figure 4-3, the length of unit-cell of the periodic structure is *l*, Z_0 and *k* are the characteristic impedance and the propagation constant of unloaded transmission line, respectively. The red dashed box indicates lumped element, and it has no length.

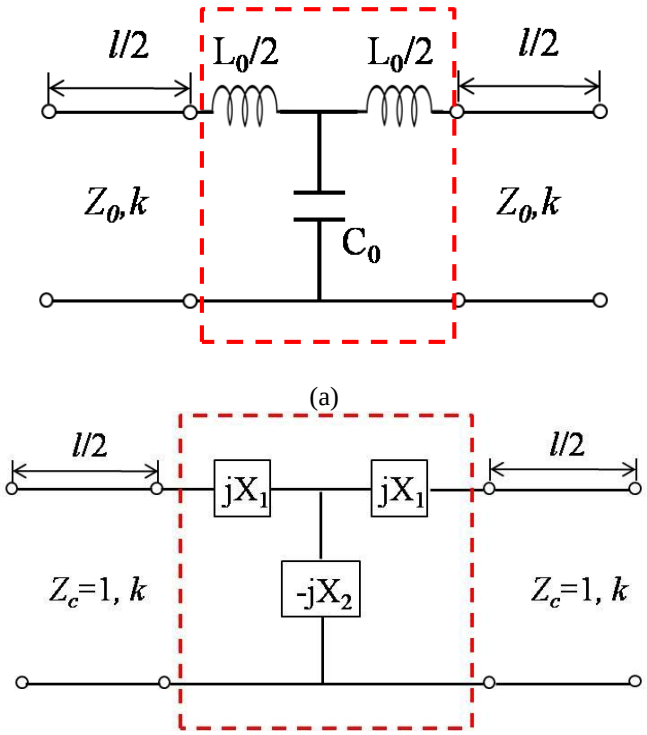

Figure 4-3: (a) The equivalent circuit of the unit cell of series inductive and shunt capacitive loads periodic electrode structure and (b) its normalized circuit form.

This structure consists of two unloaded transmission line sections and one two-port T network in red square box, which has two series inductive loads of jX_1 and one shunt capacitive load of $-jX_2$. Their inductance and capacitance are L_o and C_o, respectively.

Its ABCD matrix is also obtained by a cascade of three matrices which represents each section as shown in equation (18).

$$\begin{bmatrix} A & B \\ C & D \end{bmatrix} = \begin{bmatrix} \cos\frac{kl}{2} & j\sin\frac{kl}{2} \\ j\sin\frac{kl}{2} & \cos\frac{kl}{2} \end{bmatrix} \begin{bmatrix} 1-\frac{\overline{X}_1}{\overline{X}_2} & j2\overline{X}_1 + j\frac{\overline{X}_1^2}{\overline{X}_2} \\ j\frac{1}{\overline{X}_2} & 1-\frac{\overline{X}_1}{\overline{X}_2} \end{bmatrix} \begin{bmatrix} \cos\frac{kl}{2} & j\sin\frac{kl}{2} \\ j\sin\frac{kl}{2} & \cos\frac{kl}{2} \end{bmatrix}. \quad (4.18)$$

A, *B*, *C*, and *D* become

$$A = \left(1 - \frac{\overline{X}_1}{\overline{X}_2}\right)\cos kl - \frac{1}{2}\left(2\overline{X}_1 + \frac{1}{\overline{X}_2} + \frac{\overline{X}_1^2}{\overline{X}_2}\right)\sin kl,$$

$$B = j\left(1 - \frac{\overline{X}_1}{\overline{X}_2}\right)\sin kl - j\left(2\overline{X}_1 + \frac{\overline{X}_1^2}{\overline{X}_2}\right)\cos^2\frac{kl}{2} - j\frac{1}{\overline{X}_2}\sin^2\frac{kl}{2},$$

$$C = j\left(1 - \frac{\overline{X}_1}{\overline{X}_2}\right)\sin kl - j\frac{1}{\overline{X}_2}\cos^2\frac{kl}{2} - j\left(2\overline{X}_1 + \frac{\overline{X}_1^2}{\overline{X}_2}\right)\sin^2\frac{kl}{2},$$

$$D = \left(1 - \frac{\overline{X}_1}{\overline{X}_2}\right)\cos kl - \frac{1}{2}\left(2\overline{X}_1 + \frac{1}{\overline{X}_2} + \frac{\overline{X}_1^2}{\overline{X}_2}\right)\sin kl.$$

where $\overline{X}_1$ and $\overline{X}_2$ are normalized value of X_1 and X_2 by Z_0.

When the equations (4.8~9) are used, the eigenvalue equation is obtained as following,

$$\cosh \beta l = A = \left(1 - \frac{\overline{X}_1}{\overline{X}_2}\right)\cos kl - \frac{1}{2}\left(2\overline{X}_1 + \frac{1}{\overline{X}_2} + \frac{\overline{X}_1^2}{\overline{X}_2}\right)\sin kl. \tag{4.19}$$

The propagation constant of the series inductive and shunt capacitive loaded periodic structure, therefore, is obtained.

$$\beta = \omega\sqrt{\left(L + \frac{L_0}{l}\right)\left(C + \frac{C_0}{l}\right) - \omega^2 L_0 C_0 C\left(L - \frac{L_0}{l}\right)}. \tag{4.20}$$

In the equation (4.20), the second term can be ignored because it is much smaller than the first term. Therefore, the final form of the propagation constant, β, is

$$\beta = \omega\sqrt{\left(L + \frac{L_0}{l}\right)\left(C + \frac{C_0}{l}\right)}. \tag{4.21}$$

The phase velocity of the series inductive and shunt capacitive loaded periodic structure is as following.

$$v_p = \frac{1}{\sqrt{\left(L + \frac{L_0}{l}\right)\left(C + \frac{C_0}{l}\right)}}. \tag{4.22}$$

The equation (4.22) also can be obtained by simply adding extra inductance and capacitance terms to the equation (4.2) when the series inductance and shunt capacitance are added.

The characteristic impedance of this structure is shown in equation (4.23)

$$Z_c = \sqrt{\frac{\left(L + \frac{L_0}{l}\right) - w^2 L_0 C_0 \left(L - \frac{L_0}{l}\right)}{\left(C + \frac{C_0}{l}\right) - w^2 L_0 C_0 C}}. \tag{4.23}$$

The second term of the numerator and denominator in the equation (4.23) can be ignored because they are much smaller than their first term. The final form of the characteristic impedance of the series inductive and shunt capacitive loaded periodic structure, therefore, is as following.

$$Z_c = \sqrt{\frac{\left(L + L_0 / l\right)}{\left(C + C_0 / l\right)}}. \tag{4.24}$$

If the equation (4.23) is compared to the equation (4.1), extra inductance and capacitance terms are simply added when the series inductance and shunt capacitance are added as equation (4.22).

From above derivation, when the series inductances and capacitances are periodically loaded in the normal transmission line, the extra unit-length capacitance and inductance are simply added to the unit length capacitance and inductance of unloaded transmission line.

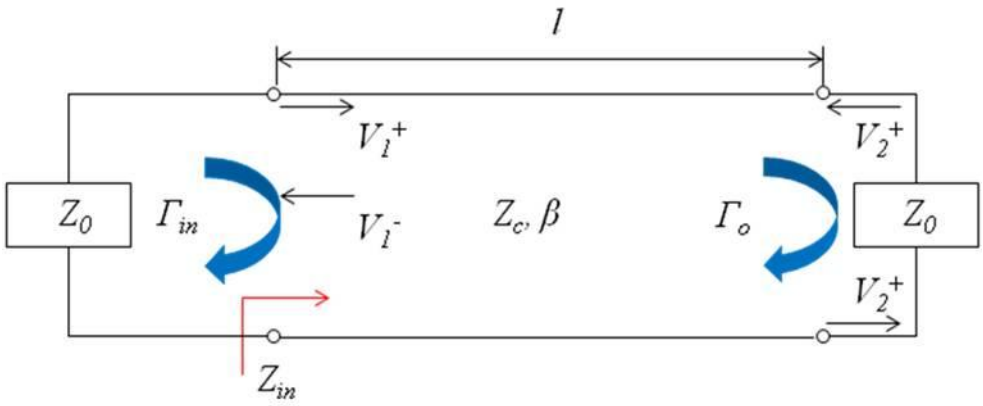

Figure 4-4: The two port network of the slow-wave electrode structure terminated with input and output impedance .

4.3 Calculating Z_c and β of the Periodic Structure from Simulation and Measurement Results

After designing or measuring slow-wave structure, its characteristic impedance, Z_c and effective dielectric constant, ε_r, need to be calculated to check the matching condition of 50 Ω and phase velocity. The S parameters are used to obtain the characteristic impedance and propagation constant of the slow-wave electrode structure from simulation because they are functions of the Z_c and β. For the high frequency transmission line simulations, HFSS of ANSOFT is usually used. However, in case of the CPS, only CST can be used to obtain proper S parameters of the transmission line.

The slow-wave electrode structure can be considered two port network as shown in figure 4-4. Z_c is the characteristic impedance of the slow-wave electrode structure, Z_0s are the input and output termination impedance of 50 Ω, Γ_{in} and Γ_o are the reflection coefficient at input and output of slow-wave electrode structure, respectively, V_1^+ and V_1^- are the forward voltage and reverse voltage at the input , respectively, and V_2^+ and V_2^- are

the forward voltage and reverse voltage at the output, respectively. Γ_{in} and Γ_o are defined as following.

$$\Gamma_{in} = \frac{Z_{in} - Z_0}{Z_{in} + Z_0}, \tag{4.25}$$

$$\Gamma_o = \frac{Z_0 - Z_c}{Z_0 + Z_c}. \tag{4.26}$$

where Z_{in} is the input impedance of the transmission line defined as

$$Z_{in} = Z_c \frac{1 + \Gamma_0 e^{-2j\beta l}}{1 - \Gamma_0 e^{-2j\beta l}}. \tag{4.27}$$

S_{11} is defined in equation (4.28) and Γ_{in} is re-defined as equation (4.29) using equation (4.25) and (4.27).

$$S_{11} = \left.\frac{V_1^-}{V_1^+}\right|_{V_2^+=0} = \Gamma_{in} = S_{22}, \tag{4.28}$$

$$\Gamma_{in} = S_{11} = S_{22} = \frac{\Gamma_0\left(e^{-2j\beta l} - 1\right)}{1 - \Gamma_0^2 e^{-2j\beta l}}. \tag{4.29}$$

S_{21} is defined in equation (4.30)

$$S_{21} = \left.\frac{V_2^-}{V_1^+}\right|_{V_2^+=0} = \frac{\left(1+\Gamma_0\right)\left(1-\Gamma_0\right)}{\sqrt{\left(1-\Gamma_0^2\right)^2 \cos^2 \beta l + \left(1+\Gamma_0^2\right)^2 \sin^2 \beta l}} \angle \arctan\left(\frac{\left(1+\Gamma_0^2\right)\sin \beta l}{\left(1-\Gamma_0^2\right)\cos \beta l}\right). \tag{4.30}$$

Using the phase term of S_{21}, the effective dielectric constant for the slow-wave electrode structure is obtained as following.

$$\varepsilon_{e,eff} = \left(\frac{c \cdot \beta}{2\pi f}\right)^2. \tag{4.31}$$

where c is the velocity of microwave in free space, l_D is the length of the slow-wave electrode structure, and f is the frequency.

To obtain characteristic impedance, Z_c, of the slow-wave electrode structure, *ABCD* matrix is used, which is obtained from S parameters [4-9].

$$\begin{pmatrix} A & B \\ C & D \end{pmatrix} = \begin{pmatrix} \dfrac{(1+S_{11})(1-S_{22})+S_{12}S_{21}}{2S_{21}} & Z_0 \dfrac{(1+S_{11})(1+S_{22})-S_{12}S_{21}}{2S_{21}} \\ \dfrac{1}{Z_0}\dfrac{(1-S_{11})(1-S_{22})-S_{12}S_{21}}{2S_{21}} & \dfrac{(1-S_{11})(1+S_{22})+S_{12}S_{21}}{2S_{21}} \end{pmatrix}. \quad (4.32)$$

Therefore, the characteristic impedance, Z_c, is calculated by using equation (4.16)

Once Z_c is obtained, the output reflection coefficient, Γ_0, propagation constant, β, and relative dielectric constant, $\varepsilon_{r,eff}$, are calculated by using equation (4.26), (4.30), and (4.31), respectively.

4.4 Slow-wave Electrode Structure

The first design is the electrode structure with periodic T-rail type shunt capacitive loads as shown in figure 4-5, which employs symmetric coplanar strip (CPS) design with higher characteristic impedance than 50 Ω, and its equivalent circuit is shown in figure 4-6.

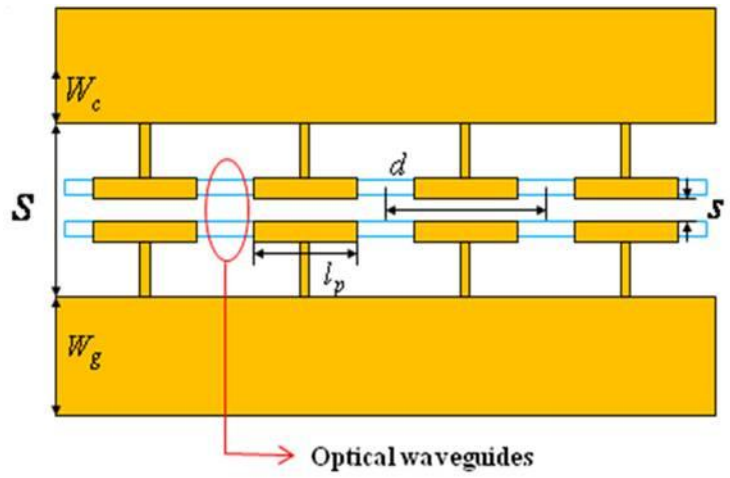

Figure 4-5: The structure of the electrode with shunt capacitive loads.

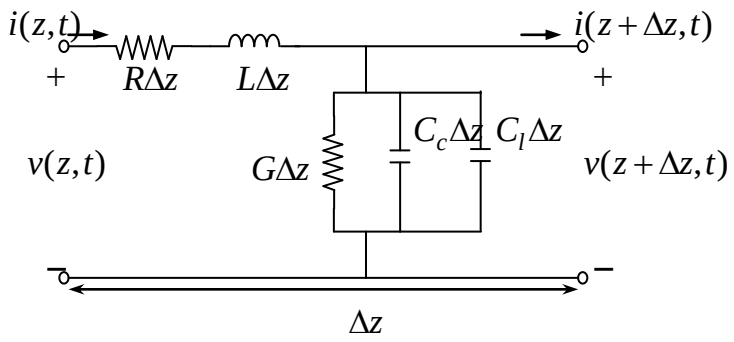

Figure 4-6: The equivalent circuit for unit cell of periodic structure.

The CPS lines are placed on both sides of the optical waveguides. These lines are periodically loaded in shunt with the T-shaped sections (T-rails) placed on the optical waveguides, which are the shunt capacitors, and are connected to the middle of the unit cell sections as shown in figure 4-5.

Charge flows in and out of these rails as displacement current. However, axial transmission line current will not flow through them because of narrow rails, and the inductance of the transmission line, therefore, will remain virtually constant. If the rails are narrow enough, and their periodicity is short then the cut off frequency is very high.

The total capacitance, characteristic impedance, and phase velocity of the shunt capacitive loaded electrode structure are written as following.

$$C_{tot} = C_c + C_l \,, \tag{4.32}$$

$$Z_0 = \sqrt{\frac{L}{C_{tot}}} = \sqrt{\frac{L}{C_c + C_l}} \,, \tag{4.33}$$

$$v_m = \frac{1}{\sqrt{LC_{tot}}} = \frac{1}{\sqrt{L(C_c + C_l)}} \,. \tag{4.34}$$

where C_c is the unit length capacitance of the CPS, C_l is the additional shunt capacitance, and L is the inductance. Therefore, the capacitance is increased without

changing the inductance, and Z_0 and v_m are decreased. The group velocity is theoretically constant and is equal to the phase velocity for these electrode structures. The effective microwave index for the capacitive-coupled electrodes becomes

$$n_m = \frac{c_0}{v_m} . \tag{4.35}$$

Where c_0 is the velocity of microwave in the free space and R and G in figure 4-6 are ignored because the loss is small..

Second design is the electrode structure with series inductive and shunt capacitive loaded periodic structure. In this design, the characteristic impedance of CPS can be 50 Ω because the proper amount of the extra inductive and capacitive loads are maintaining the characteristic impedance of 50 Ω.

The inductive loads are realized by inserting a high impedance short length of transmission line in the original CPS transmission line as shown in figure 4-7. The upper part in figure 4-7 is the top view of the CPS line and the lower is the schematic diagram of the line. In figure 4-7, T_1 is the original 50 Ω transmission line and T_2 is the inserted short high impedance transmission line, Z_o and Z_h are the characteristic impedances of T_1 and T_2 respectively, and $Z_h > Z_o$. Let Z_{in} be the input impedance at terminals AA' and d is the length of the inserted transmission line, T_2.

Using the approximation in [4-8], Z_{in} is expressed by

$$Z_{in} \cong Z_o + jZ_h\beta_h d . \tag{4.36}$$

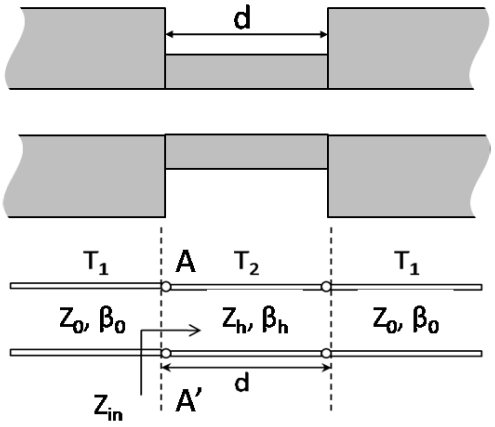

Figure 4-7: Schematic of CPS with the series inductive load.

provided d/λ << 1. In equation (4.36), the real part of Z_{in} is the same as Z_o and the imaginary part of Z_{in} is a positive value due to its short length, and the positive imaginary part of Z_{in} is inductive. Therefore, the inductive load is added in series by inserting a short length of high impedance line in the original CPS line.

The series inductive and shunt capacitive loaded slow-wave electrode structure is shown in figure 4-8. The CPS lines are placed on both sides of the optical waveguides.

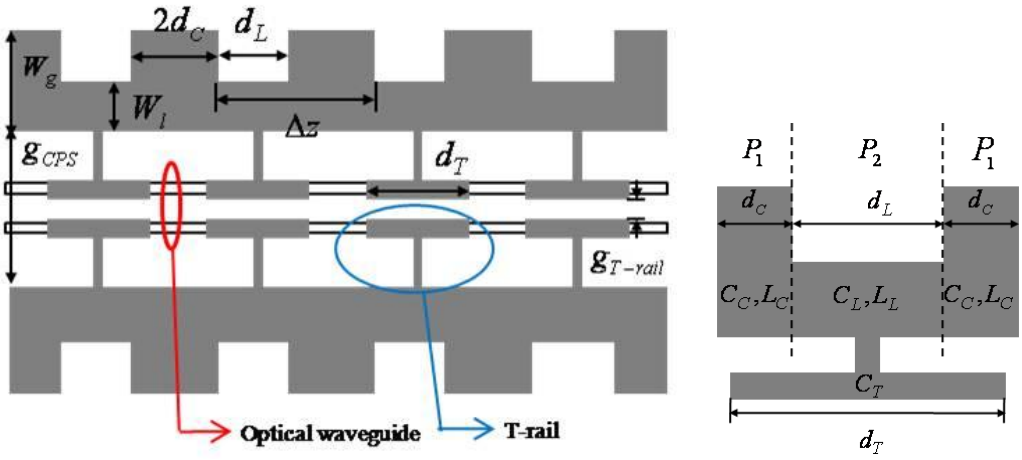

(a) (b)

Figure 4-8: (a) The slow wave electrode structure with inductive and capacitive loads (b)an enlarged view of a unit cell.

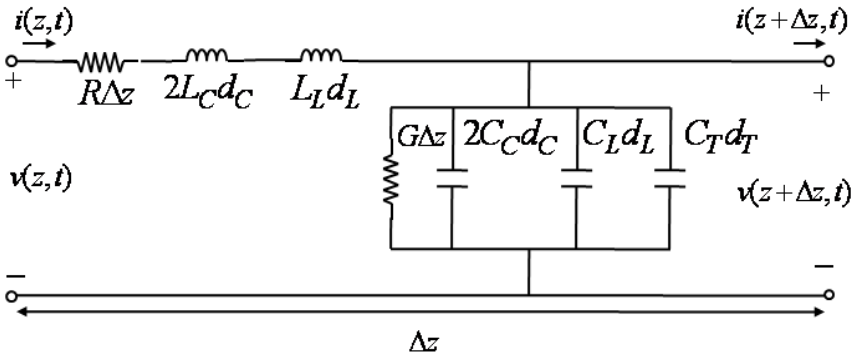

Figure 4-9: An equivalent circuit of the unit cell.

These lines are periodically loaded in series with inductive sections and the T-shaped sections (T-rails) placed on the optical waveguides, which are the shunt capacitors, are connected to the middle of the inductive sections as shown in figure 4-8. In figure 4-8, W_g and W_l are the widths of the original CPS and inductive section respectively, Δz is the length of the unit cell, d_L is the length of the inductive section, g_{CPS} and $g_{T\text{-}rail}$ are gaps between signal and ground lines of CPS and T-rails, respectively.

T- rails are narrow, and their periodicity is 100 μm, which is much shorter than the wavelength at the maximum frequency of interest, so that the lumped element equivalent circuit model may be used to calculate the characteristic impedance and effective refractive index over a wide frequency range.

From figure 4-9, the total inductance and capacitance may be written as

$$L_{tot} = 2L_C d_C + L_L d_L , \tag{4.37}$$

$$C_{tot} = 2C_C d_C + C_L d_L + C_T d_T , \tag{4.38}$$

$$Z_o = \sqrt{L_{tot} / C_{tot}} , \tag{4.39}$$

$$v_m = 1 \Big/ \left(\sqrt{L_{tot} C_{tot}} \Big/ \Delta z \right). \tag{4.40}$$

where L_C *and* C_C are the unit length inductance and capacitance of the original CPS line, P_1 section in figure 4-8 (b), L_L *and* C_L are the unit length inductance and capacitance of the inductive part, P_2 section in figure 4-8 (b), C_T is the unit length capacitance of the capacitive loading part, a T-rail section in figure 4-8 (b), C_{tot} and L_{tot} are the total capacitance and inductance of loaded CPS line respectively, Z_o is the characteristic impedance, v_m is the phase velocity of the microwave signal in the slow wave structure with series inductive and shunt capacitive loads, and R and G in figure 4-9 are ignored as the loss is small.

From equations (4.39) and (4.40), the characteristic impedance Z_o is maintained at 50 Ω, and the phase velocity is lowered depending on the values of series inductance and shunt capacitance.

The dimension of the designed slow-wave structure is shown in figure 4-10. W_g=80 μm, W_l=32 μm, Δz=100 μm, d_T=92 μm, g_{CPS}=54 μm, $g_{T\text{-}rail}$=5.62 μm, d_L=50 μm, substrate thickness=150 μm, device length=2.5 *cm*, and electrode thickness=3 μm.

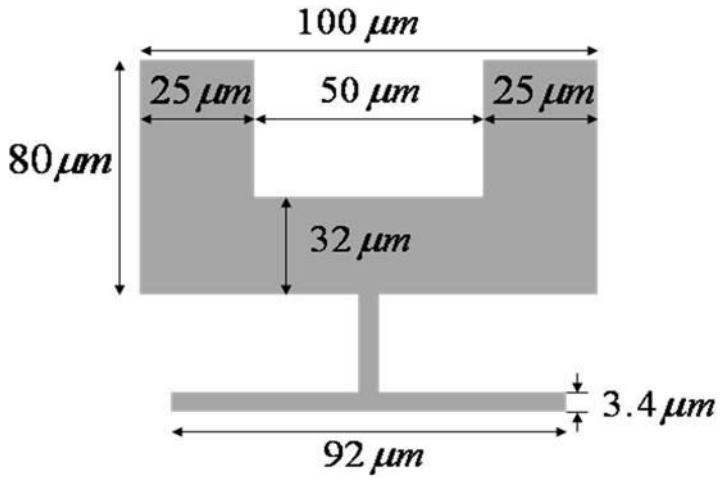

Figure 4-10: The dimension of the designed slow-wave structure

4.5 References

[4-1] R. Spickermann, N. Dagli, "Experimental analysis of millimeter wave coplanar waveguide slow wave structures on GaAs," *IEEE Trans. Microwave Theory & Tech.,* Vol. 42, pp. 1918-1924, Oct. 1994

[4-2] A. Gorur, G. Karpus, and M. Alkan, "Characteristics of periodically loaded CPW structure," *IEEE Microwave Guided Wave Lett,* vol. 8, pp. 278-280, Aug. 1998

[4-3] J. Sor, Y. Oian, and T. Itoh, "Miniature low-loss CPW periodic structures for filter applications," *IEEE Trans. Microwave Theory Tech,* vol. 49, pp. 2336-2341, Dec. 2001

[4-4] Xu Feng, Li Lin, Wu Ke, S. Deoprat, M. Chaker, "Application of FDFD Algorithm Combined with Shift-and-Invert Arnoldi Technique in Bilateral Interdigital Coplanar Waveguide Slow wave Structure," *IEEE MTT-S Int. Micro. Symp. Dig.* 11-16, pp.1025-1028, June, 2006

[4-5] E.H. Bottcher, H. Pfitzenmaier, E Droge and D Bimberg, "Millimetre-wave coplanar waveguide slow wave transmission lines on InP*," Electron. Lett.*, Vol.32, No.15, pp1377-1378, July 1996

[4-6] Lei Zhu, "Guided-Wave Characteristics of Periodic Coplanar Waveguides With Inductive Loading-Unit-length Transmission Parameters," *IEEE Trans. Microwave Theory & Tech.,* Vol. 51, pp. 2133-2138, Oct.2003

[4-7] Nicolas A.F. Jaeger, Farnoosh Rahmatian, Hiroshi Kato, Robert James, Ezio Berolo, and Zachary K.F. Lee, "Velocity-Matched Electrodes for Compound Semiconductor Traveling-Wave Electrooptic Modulators: Experimental Results," *IEEE Microwave Guided Wave Lett.*, vol. 6, pp. 82-84, Feb.1996

[4-8] David, M, Pozar, *Microwave and Rf Desing of Wireless Systems*, John Wiley & Sons Inc, pp. 174-175, Nov. 2000

[4-9] David, M, Pozar, *Microwave and Rf Desing of Wireless Systems*, John Wiley & Sons Inc, pp. 211, Nov. 2000

CHAPTER 5 Fabrication of the Linear Directional Coupler Modulators

5.1 Introduction

In this section, the fabrication of the various designs of the linear optical directional coupler modulators is discussed. The fabrication procedure has several steps, and there are waveguide fabrication, electrode fabrication, and the thinning of wafer. The most important section in the optical coupler modulator fabrication is the etching the optical waveguide. The etch rate between the ends the coupler waveguides should be identical, as otherwise the mode profile and the coupling property will vary. However, actual etch rates between the center and the end of the waveguides are different because of the limitation of the etching equipment. The Trion II, which is chlorine-based RIE (Reactive Ion Etching) etching machine, is used for etching the waveguides of the GaAs/InGaAs material. This machine was built in 1990 and its etching is not uniform even over 50mm wafers. The length of the optical coupler waveguides is 3 cm including input and output sections, and the coupler waveguides are not etched uniformly.

The cross section of the wafer for the optical coupler modulator is shown in Figure 5-1. The epitaxial layers of GaAs/AlGaAs/GaAs/AlGaAs are grown with [100] vector normal to the plane of the semi-insulating GaAs substrate by MBE (Molecular beam epitaxy), which thicknesses of 100/10000/10000/30000 Å, respectively.

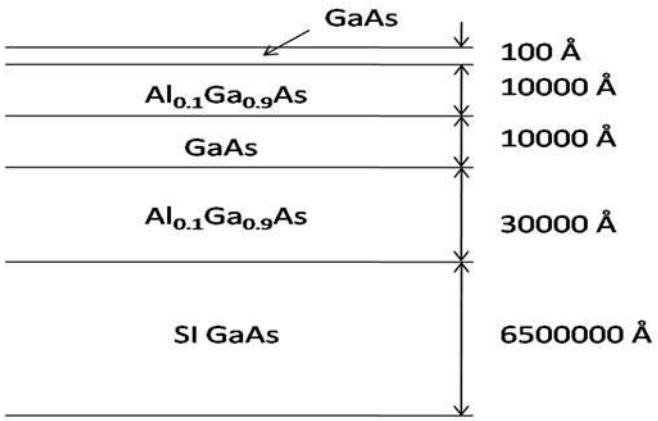

Figure 5-1: Epitaxial layers used for the fabrication of the optical modulator.

In the figure 5-1, the top layer of GaAs is grown to prevent oxidization of the upper AlGaAs layer, where this and the fourth layers of AlGaAs are the cladding of the waveguides, and the third of GaAs is the guiding layer. The refractive index of the cladding and guiding layers are 3.4021 and 3.4501, respectively, at 1300 nm wavelength.

5.2 Waveguide Fabrication

The light propagate along the $\langle 01\bar{1} \rangle$ and $\langle 011 \rangle$ directions which is parallel with cleaved facet. Quarter sections of 75 mm GaAs/AlGaAs wafers were used for the optical modulator. The optical waveguides dimension is shown in figure 5-2. The single ridged waveguide has a width of 3.5 μm and height of 0.8 μm. The gaps between the ridges are 5um for the uniform coupler and varied from 2 μm to 6um for the variable coupler. The length of the coupler is 3 cm including input and output sections. Although 4cm and 5cm device had been designed, and fabricated, these could not be measured, because of uneven etching and rough surface on the wafer due to the malfunctioning of RIE system,

which caused light leakage and high losses. Therefore, only the 3 cm long couplers have been fabricated and tested.

The equipment used in the waveguide fabrication are plasma-enhanced chemical vapor deposition (PECVD) for depositing SiO_2 and Si_3N_4, the photoresist spinner for coating the wafer with photoresist (PR), Karl Suss Mask Aligner (MABA6 or MA6), STS Reactive Ion Etching (RIE) etcher for removing organic material or PR residues on the wafer and etching SiO_2 and Si_3N_4, and the Trion II chlorine-based RIE system for etching GaAs/AlGaAs. The chemicals used in photolithography are Acetone, Methanol, Isopropanol (IPA), Hexamethyldisilizane (HMDS), PR, 351 developer, and Buffered oxide etch (BOE). Acetone, Methanol, and IPA are used for cleaning wafers or removing PR on the wafers, HMDS is used as a PR adhesion promoter, the PR 351 developer is used for developing patterns exposed by mask aligner in the PR on the wafers, and BOE is used for etching SiO_2 and Si_3N_4.

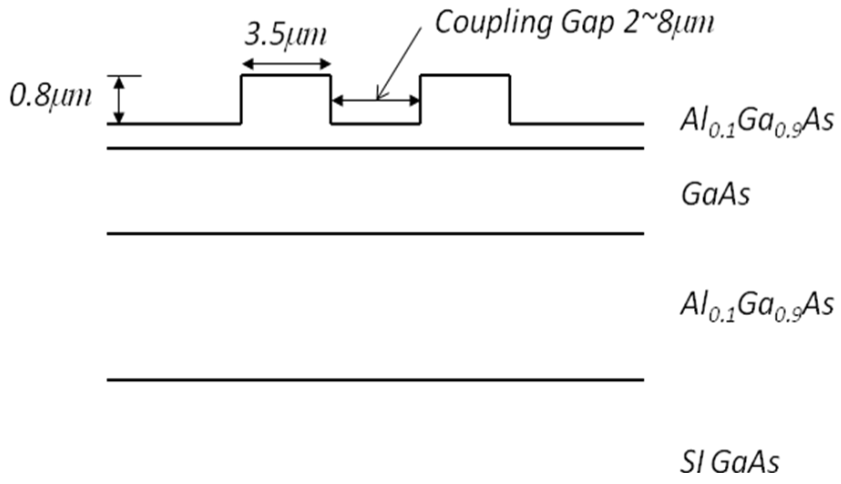

Figure 5-2: Dimension of the Coupler waveguides and coupling gap is about 6μm for the uniform coupler and varied from 2 μm to 10 μm for the variable gap coupler.

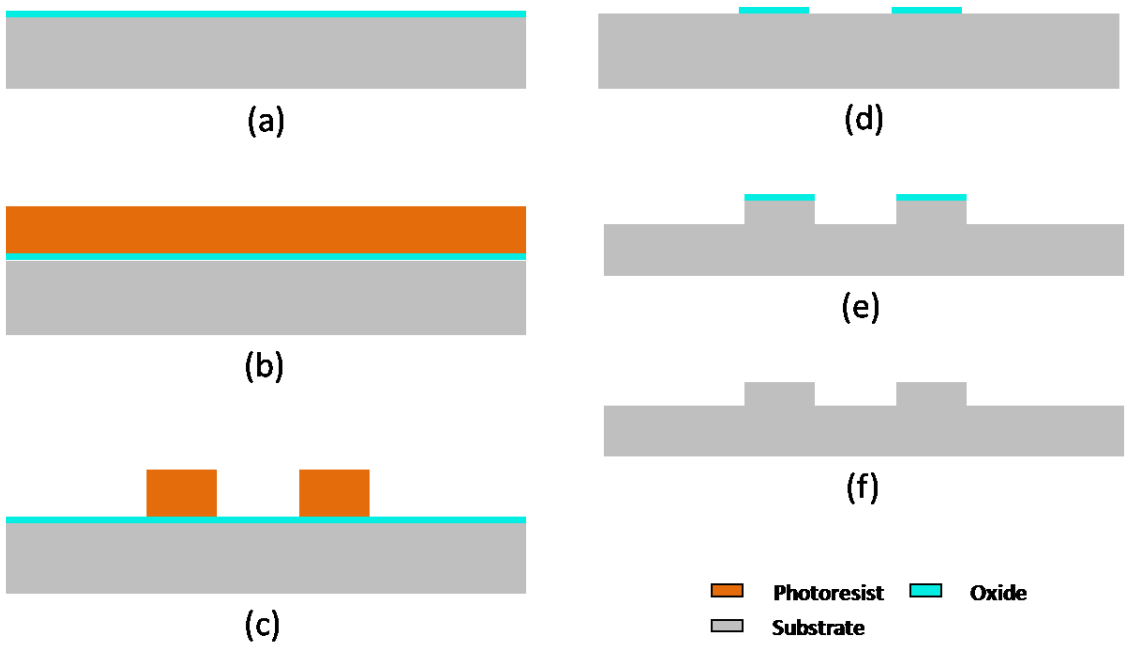

Figure 5-3: The steps of the waveguide fabrication.

The processing steps for the waveguides fabrication are shown in Figure 5-3. The fabrication starts with depositing 1000 Å oxide on the entire wafer as shown in figure 5-3 (a). This oxide layer is used for the waveguide mask during the waveguide etching. PR is commonly used for the waveguide mask, but the etch gases for GaAs/AlGaAs are Cl_2 and BCL_3, and these etch the PR as well. However, SiO2 is a good material for the etch mask because the etch rate is very low with these gases. Titanium was also used for the waveguide mask. However, it was later abandoned because it re-deposits on the wafer during the waveguide etching. The SiO_2 layer is deposited on the AlGaAs/GaAs wafer by using PECVD at 300 ˚C for 4 minutes.

The second step is photolithography with the first waveguide mask depicted in figure 5-3 (b) and (c). The photolithography process is as following;

1) Solvent clean with Acetone, Methanol, and IPA.

2) Pre-bake the wafer on a hot plate at 115 ˚C for 60 second.

3) place wafer in HMDS bath for 3 minutes.

4) Coat wafer with PR type S1813, with spinner speed set at 3500 rpm for 30 seconds.

5) Soft-bake wafer on hot plate at 105 ˚C for 60 seconds.

6) Expose with Mask I in the MABA6 aligner for 4 seconds.

7) Post-bake wafer on hot plate at 105 ˚C for 1 minute.

8) Develop patterns on wafer in 351 developer for 1 minute.

9) Rinse wafer with DI water for 3 minute

9) O_2 clean using STS etcher for 10 second to remove PR residue.

Next step is etching the oxide layer using the STS etcher. However, one important procedure should be performed before dry etching of the oxide layer. At the edge of the waveguide patterns, the PR and the oxide create polymer residue during the plasma etching, and the waveguides are not clean and smooth, which results in scattering of the guided light and increased loss. Wet etching the oxide with BOE (Buffered oxide etch) for 3 seconds is the solution to this problem. The steps by wet etching shown in the circle of figure 5-4 remove the chance to create PR/oxide polymer from plasma etching.

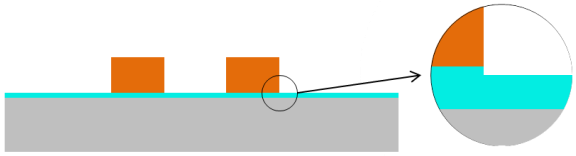

Figure 5-4: The step after short time wet etching.

The next step is etching the waveguides using the Trion II RIE system. The wafer holder for the Trion II is for 4" wafer, and a quarter of a 3" wafer used for the fabrication is loaded centrally in the wafer holder as shown in figure 5-5. In addition, to obtain better etching results, a blank 4" GaAs wafer was used as a pad wafers. The etching condition is as following;

Power 80 Watt

pressure 30 mtorr

Cl_2 20 sccm

BCl_3 20 sccm

Ar 40 sccm

etch rate of first run 420 Å/10 sec ~ 505 Å/10 sec

etch rate of second run 280 Å /10 sec ~ 350 Å /10 sec

Cl2 and BCl3 are usually used for etching GaAs or AlGaAs, but the etched surface using only these gases is not smooth. To obtain good surface condition, Argon gas is added, and increases surface smoothness. The etch rates of the sample are around 460 Å/10sec and 290 Å/10sec, respectively. In the first etch, GaAs and AlGaAs were etched, and in the second etch, only AlGaAs was etched. The wafer being etched should be rotated after the first etching step as shown in figure 5-5 because the etch rate at the ends of the wafer is higher than that at center of the wafer, and the etch rate of each end of the wafer is also different. The etching profile along the wafer is shown in figure 5-6.

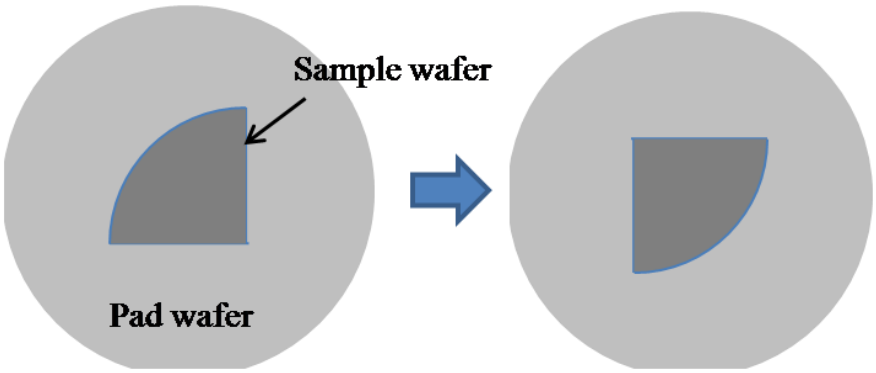

Figure 5-5: Rotation of the etching sample during etching.

After the first dry etch process the sample is soaked in DI water for 5 min to remove Cl2 on its surface, as otherwise the surface quality remains poor during the second etch step.

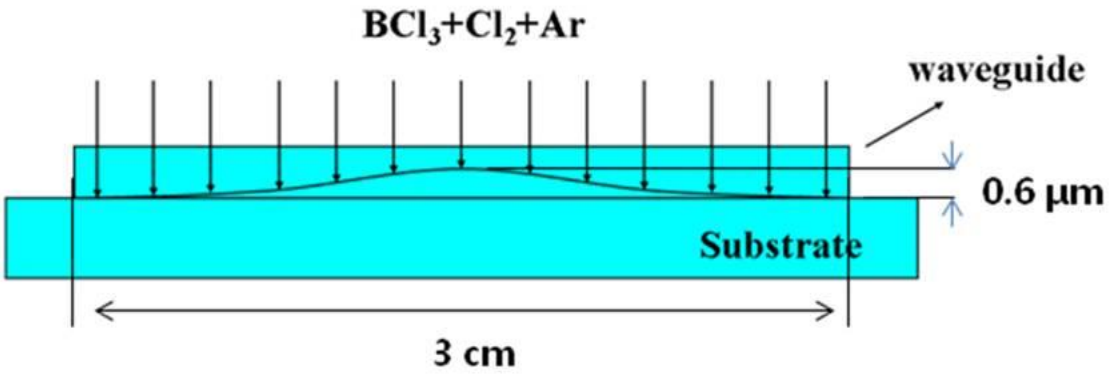

Figure 5-6: The side view of the waveguide after etching.

5.3 Electrode Fabrication

In high frequency operation, the electrodes of the directional coupler modulator are considered as a transmission line. For the low conductor loss, 3 μm thick Au was used for the transmission line, and electroplating was used to obtain this thick line. However, during the electroplating both side of T-rail shunt capacitive loads were connected because the gap between the signal and ground of the T-rail loads is too narrow. To

avoid this happening, a thick nitride layer was used for the electroplating mask. To obtain a good profile of thick electrode, the process of the fabrication is more complicated and needed more steps. The process needed around 10 or more hours to deposit the thick silicon nitride and also to etch the thick silicon nitride.

The normal electro-plating procedure with blank wafer or plating sample is as following;

1) depositing seed layer of Ti/Au (400A/2500A) over the entire area of the sample wafer

2) Expose the transmission line pattern using photolithography and open the contact area for the current flow

3) Place the sample wafer which is connected to the current source in the gold-plating solution

4) After plating remove the PR

5) Remove the seed layer of Au layer using gold etchant

6) Remove the seed layer of Ti layer using HF solution.

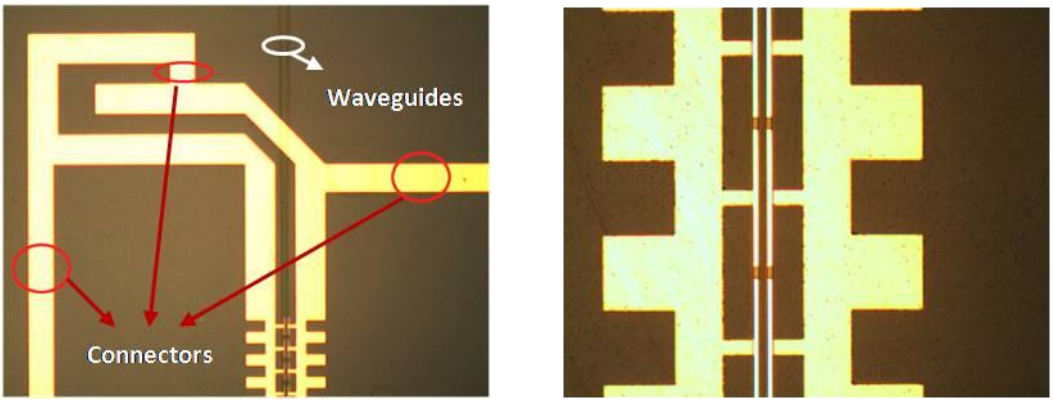

Figure 5-7: The seed layer which is not covered entire surface of sample.

A problem of etching the seed layer process arises if there are waveguides on the wafer. The waveguides should be protected from gold etchant, otherwise the gold

etchant attack the waveguides. The gold etchant sinks into the narrow opening at the T-rail structure and waveguide contact region, and destroys the waveguides. To protect waveguides the seed layer is deposited only over the transmission line patterns and connection parts between transmission lines as shown in figure 5-7, and then using silicon nitride to cover the waveguides area after electro-plating. Then, the optical waveguides protecting process should be added, and in the figure 5-7, the red circles indicate connector to another transmission line for the electro plating.

Two methods are possible for the liftoff process, depending on the PR type, the first uses normal positive PR of S1800 series with chlorobenzene, and the other uses the liftoff resist (LOR). In the first process, the chlorobenzene makes the surface of the PR harder than inner part, and the etching speed of PR surface is slower than that of inner part. The profile of the cross-section of the developed PR after soaking the sample in chlorobenzene is shown in figure 5-8 (b). However, the chlorobenzene should be treated carefully in the fume hood, because it is a cancer-causing factor. In the Liftoff process using LOR, the lower layer of LOR is coated first and then normal PR such as S1800 series is coated as a second layer. The upper layer of the PR is developed first after the exposure in the aligner , and then the LOR is etched. The etching depth and width of LOR layer is identical to the PR because the LOR does not react with the ultra violet light in the aligner, but since it is an isotropic material, it also has etched side walls as shown in figure 5-8 (f). The thickness of the LOR should be carefully chosen for the height of the pattern on the sample. The liftoff process using LOR gives better quality metal contact if there are no waveguides on the surface. However, if there are waveguides on the surface, chlorobenzene method and LOR method are comparable. The liftoff

procedures of S1800 series and liftoff resist are shown in figure 5-8 and explained in Table 5-1. Figure 5-8 (a) ~ (d) show the chlorobenzene process and figure 5-8 (e)~ (i) show the LOR method.

The process steps for the transmission line fabrication are shown in figure 5-9.

a) Deposit 0.4 μm thick oxide on the entire area of the sample wafer by using the PECVD system.

b-1) Normal photolithography process with Mask II to open the contact area in the oxide between T-rail and top of the waveguides.

b-2) Etch the oxide with STS etcher.

c) Liftoff process by the chlorobenzene method with PR 1818 to deposit seed layer.

d) deposit 3.5 μm thick silicon nitride at 300˚C in the PECVD system.

e-1) Photolithography process with Mask III to open the area for electroplating.

e-2) Soak the sample contacted by wire with current source in gold plating solution at 2mA for 1 hr.

f-1) deposit 2000 Å thick silicon nitride at 300 ˚C in the PECVD system.

f-2) Photolithography process with Mask IV to open the area for etching connection sections.

f-3) Open the connection sections by etching with STS etcher.

f-4) Etch the gold using gold etchant for 30 sec.

f-5) Etch the Pt/Ti film, all silicon nitride, and silicon dioxide except the pad oxide under the transmission lines

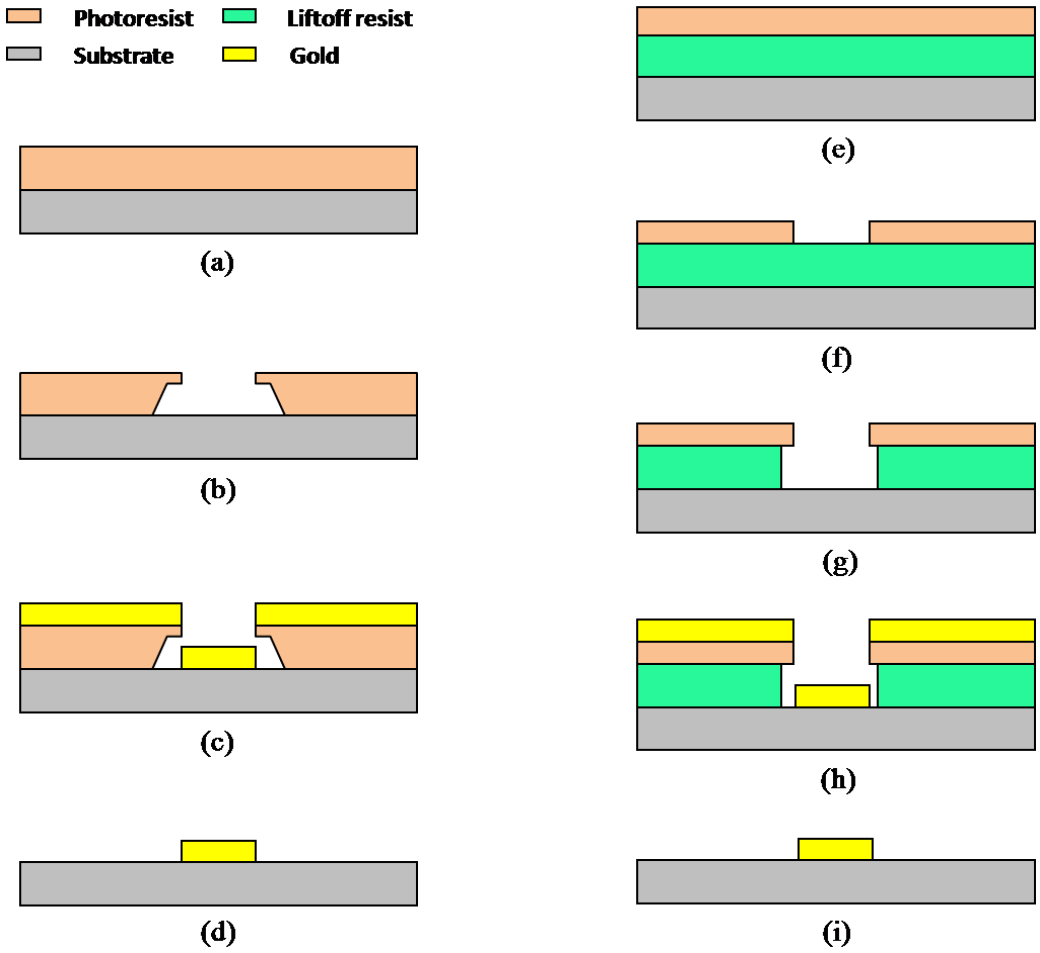

Figure 5-8: The liftoff process step of chlorobenzene method and LOR method.

Table 5-1: The liftoff procedure of Chlorobenzene method and LOR method.

Fig 8.10	Chlorobenzene method	Fig 8.10	LOR method
	Solvent cleaning procedure		Solvent cleaning procedure
	Prebake the sample at 115 on the hotplate		Prebake the sample at 115 on the hotplate
(a)	Coat the PR 1818 at 3500 RPM for 30 sec	**(e)**	Coat LOR at 2500 RPM for 45 sec
	Softbake the coated sample at 105 on the hotplate for 90 sec		Softbake the coated sample at 175 on the hotplate for 2 min
	Soak the sample in Chlorobenze for 7 min		Coat the PR 1813 at 3500 RPM for 30 sec
	Exposing the sample for 7 sec		Softbake the coated sample at 105 on the hotplate for 60 sec
	Post bake at 105 for 1 min		Exposing the sample for 4 sec
(b)	Developing for 90 sec with 351 developer	**(f)**	Developing for 30 sec with 351 developer
	Brow dry and Plasma O2 clean process to removing PR residues		Softbake the developed sample at 170 on the hotplate for 2 min
	HF for 10 sec to remove the oxide on the surface of the sample		Soak the developed sample in MF SD-26 for 90 sec
(c)	Metal deposition by CHA E-beam evaporator		Brow dry and Plasma O2 clean process to removing PR residues
(d)	Soak the metal deposited sample in the Acetone for long period		HF for 10 sec to remove the oxide on the surface of the sample
	Rinse the sample with solvent cleaning	**(g)**	Metal deposition by CHA E-beam evaporator
		(h)	Soak the metal deposited sample in the Acetone to remove PR and then boiled 1165 to remove LOR
			Rinse the sample with solvent cleaning

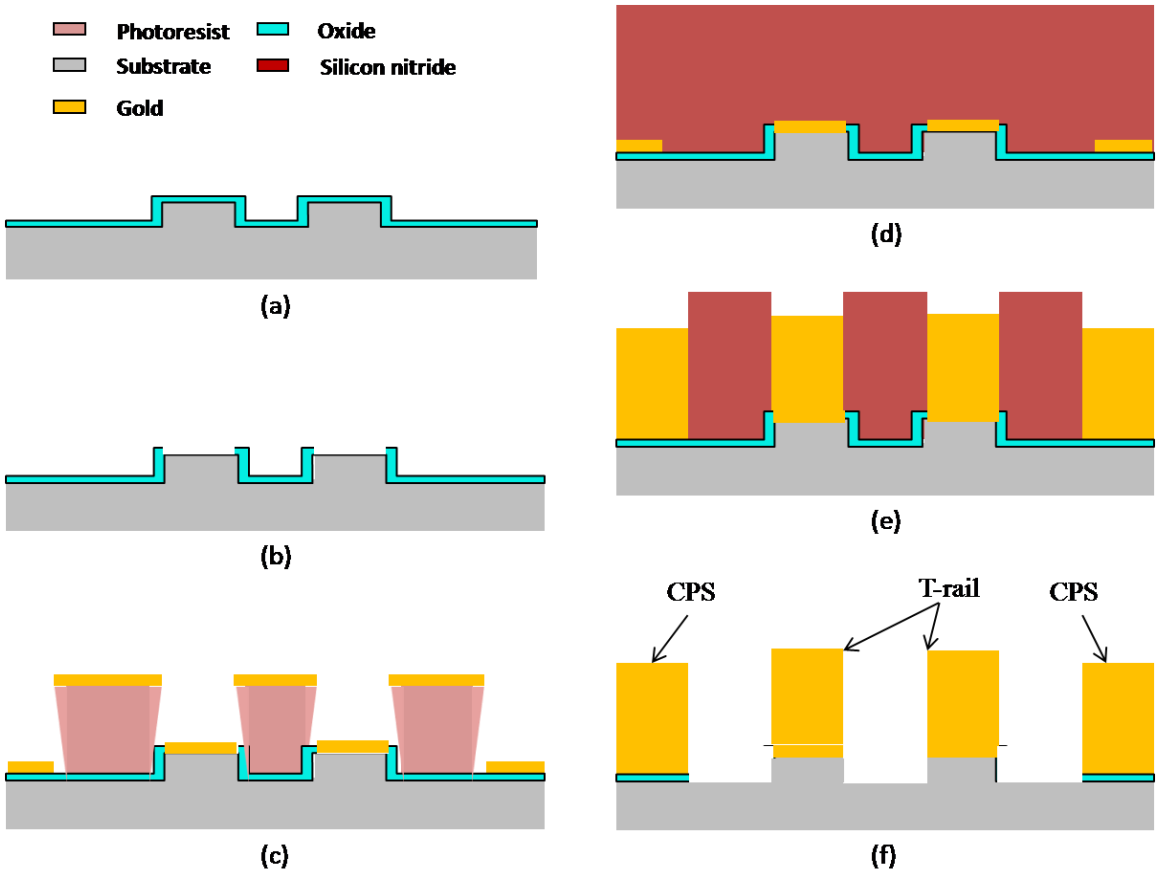

Figure 5-9: The fabrication procedure of the transmission line.

5.4 Thinning Wafer

The waveguide of the optical directional modulators is cleaved to obtain clean facets for the input and output ends for minimize coupling loss. However, the thickness of the sample wafer is around 650 μm, and it is too thick to get the clean facets at the input and output ends of the waveguides when it is cleaved. If the thickness of the sample is around 100 μm, the clean facets are obtained. It is therefore necessary to thin the wafer.

For thinning the sample, abrasive papers of 400 and 600 grit, DI water, and a thickness guage were used. The sample is thinned using sand paper and DI water by hand in a hood in a figure of eight trace and turning sample. The thickness needs to be checked

frequently using the thickness guage, otherwise the thickness of the sample may not be even. The sample should be attached with PR on a glass slide as shown in figure 5-10 for this thinning process.

5.5 Background Metalization

For integrating the optical directional coupler modulator at the circuit level, it should have background metalization, for attaching the substrate to a suitable package. The sample remains attached to the glass slide, and these are cleaned using cotton tips soaked by acceton and IPA, and wrapped with aluminum foil except for the areas where the ground plane of transmission lines, with probe pads exist, as shown in figure 5-11.

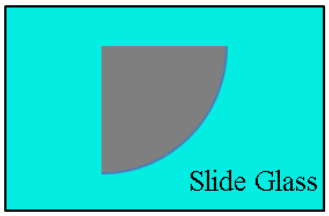

Figure 5-10: The sample wafer attached on the slide glass for thinning.

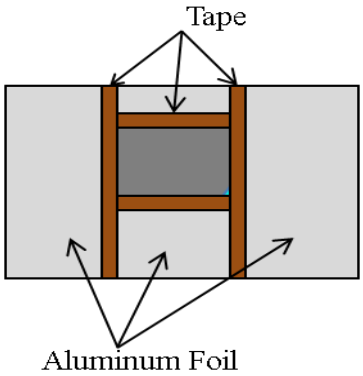

Figure 5-11: The sample attached on the glass and wrapped by aluminum foil.

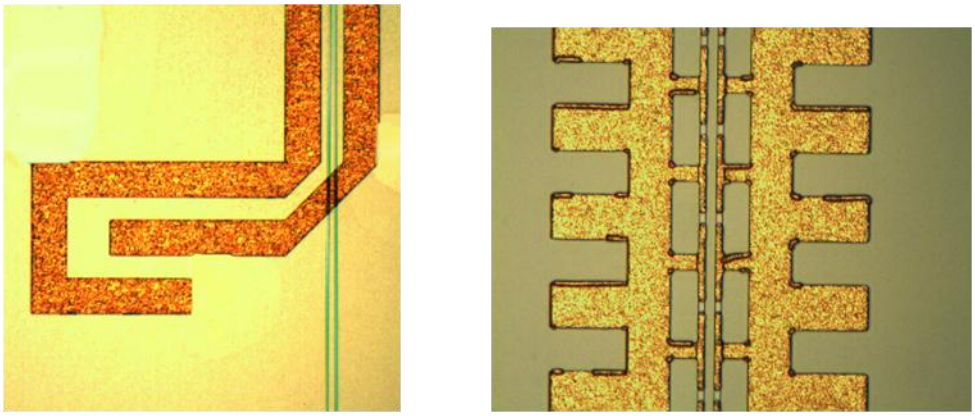

Figure 5-12: Fabricated optical directional coupler modulator with slow wave electrode structure.

Ti/Au are deposited to a thickness of 400/2000Å using the CHA e-beam evaporator. The sample deposited with the metals needs to be soaked for one day in the acetone to detach it from slide glass. The final version of the optical modulator is shown in figure 5-12.

CHAPTER 6 Experiment

In this chapter, the measurement of DC and RF for the optical directional coupler modulator are performed and the waveguide loss is measured as well.

In section 6.1, basic measurement of the optical modulator is presented, which includes breakdown voltage measurement and optical waveguide loss measurement In section 6.2, the DC and RF measurements of the modulator are discussed, which obtain the DC intensity response of optical modulator, the characteristics of the slow-wave electrodes, RF frequency response, and modulation test with two-tone for the harmonics and SFDR response.

6.1 Basic Measurement

6.1.1 Breakdown Voltage Measurement

The breakdown voltage determines the maximum voltage that can be applied to the Schottky barrier electrodes of the device. For the SI doped wafer which has the minimal carrier concentration, the breakdown voltage is in general over 50 V. When the modulators are designed the breakdown voltage should be considered because switching voltage of the modulator should not be larger than that, otherwise the device may be broken. The doping concentration of the carrier determined the depletion region width and is important to determine the overlap integral between the applied electric field and the field of the optical mode. The depletion region is defined by

$$w_{depletion} = \sqrt{\frac{2\varepsilon_0 \varepsilon_r (V_{Built} + V_{Applied})}{qN}} \quad . \tag{6.1}$$

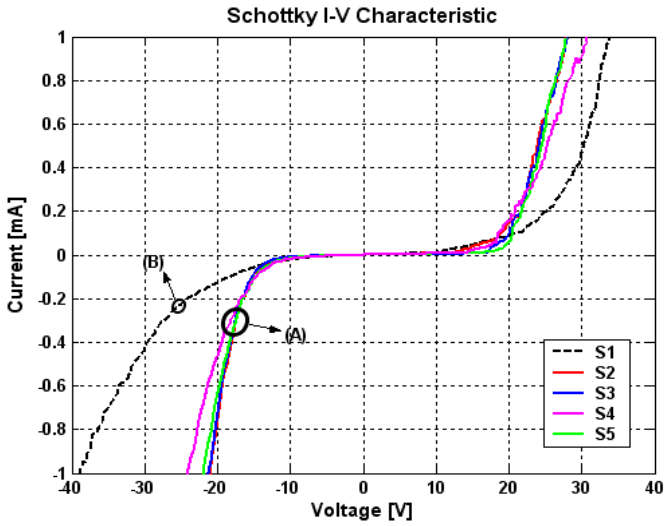

Figure 6-1: I-V characteristic of Schottky contact for real devices.

where ε_0 and ε_r are the permittivity of vacuum and dielectric constant of the semiconductor material, respectively, V_{Built} and $V_{Applied}$ are the built-in voltage and applied voltage, respectively, and N is the doping concentration. For the high concentration of the carrier with fixed applied voltage, the depletion region is small which means that the electric field does not extend to the guiding layer, and so the overlap integral is poor. The switching voltage of the device, therefore, is high, which is undesirable.

The I-V characteristics of the devices shown in figure 6-1 were measured by using HP 4145A parameter analyzer with 5 designed electrode samples which are from S1 to S5. From this figure most of the devices (S2 to S5) of group (A) show breakdown voltages around 15V, but one devices (S1) of group (B) shows the breakdown voltage of 20V.

To obtain proper value of breakdown voltage, very low doped GaAs substrate was used. During the fabrication process, residue of photoresist or oxide layer may remain, and the I-V characteristics become poor. To reduce this problem, STS Etcher was used

to remove photoresist, and wet etch may be used to remove native oxide layer before the Schottky metal Ti/Au are deposited. After the STS etcher operation for removing residue of photoresist with O_2 background, for wet etching the samples were put in the $NH_4OH:H_2O$ (1:20) for 20 seconds. After the wet etch step, the sample was put in the evapolator immediately to reduce the effect of creating native oxide. After this processing, reasonable Schottky diodes were obtained.

6.1.2 Loss measurement

To measure the waveguide loss, the cut-back method illustrated in figure 6-2 was used, and loss measurements were carried out without electrodes on the waveguides. The result of the loss measurement is shown in figure 6-3. When the input power is 361μW the output is about 3.95 μW and the output increased to about 8.8 μW after the cleaving, and the loss is about 1.42dB/cm which is a very low value for dry etched ridge waveguides. In this measurement, insertion loss is larger than typical value because input facet may have been rough due to difficulties with cleaving.

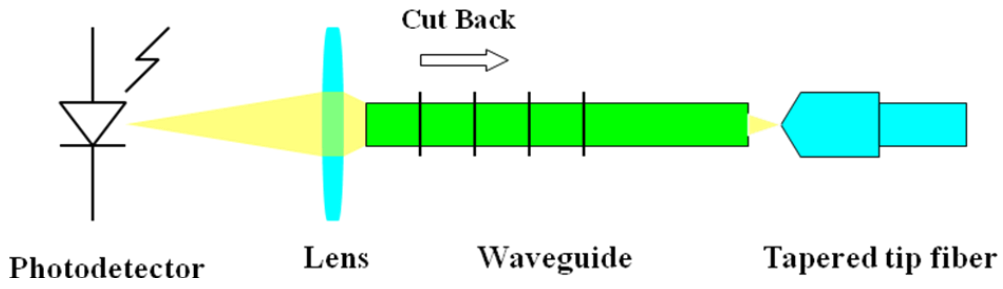

Figure 6-2: Cut-back loss measurement.

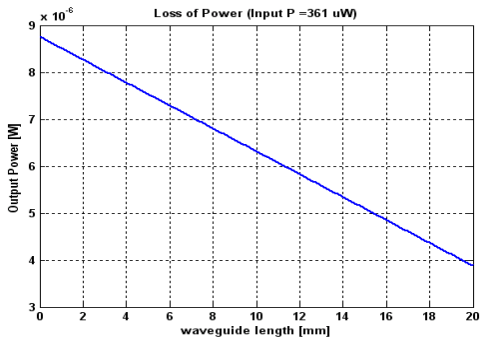

Figure 6-3: Power loss of waveguide.

6.2 RF and DC Measurement

6.2.1 Characteristics of the Slow-wave electrode structure Measurement

The S-parameter measurement should be performed to define the characteristic of the designed slow-wave electrode structure. The schematic diagram of the measurements setting is shown in figure 6-4 and the photo of this setting is shown in figure 6-5. The measurements have been carried using HP 83651B 10 ~ 50 GHz synthesized sweeper, HP 8517B 45 MHz ~ 50 GHz S-parameter test set, and HP 8510C Network analyzer. The transmission line measurement is performed after calibration with the TRL method. The calibration kit for this, which includes a 50 Ω line, three delay lines, through and open lines of CPS, is built with optical waveguides and transmission lines on the same substrate.

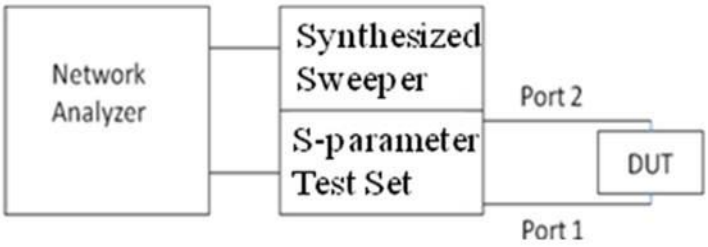

Figure 6-4: The schematic diagram of the RF measurement.

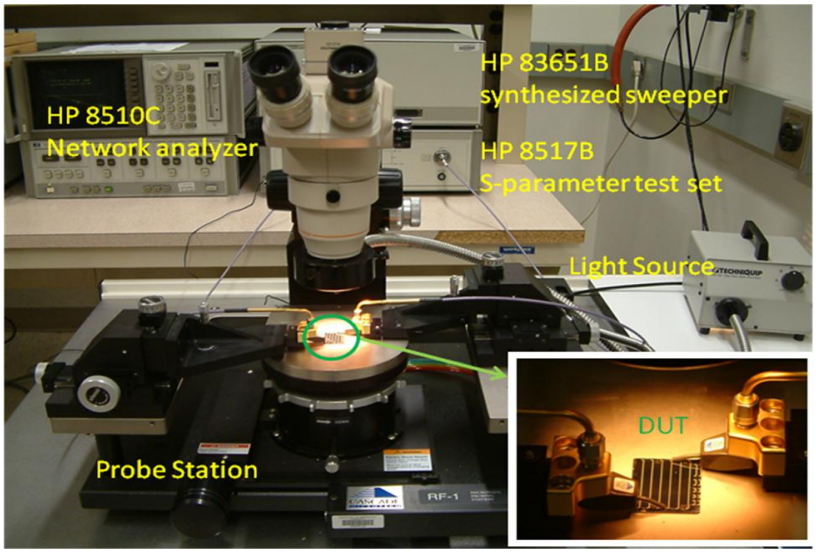

Figure 6-5 The RF measurement setting

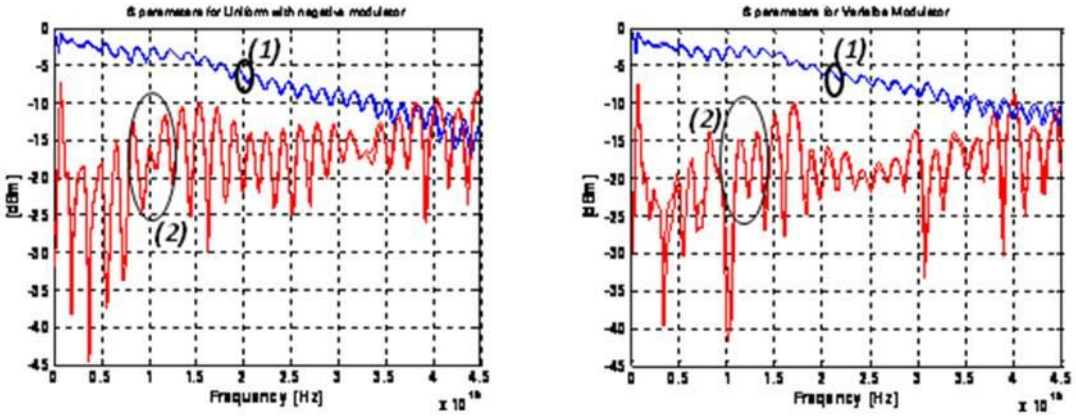

(a) (b)

Figure 6-6: S-parameters of (a) uniform coupler with phase shifts modulator (b) variable coupling coupler modulator. (1) lines are S11 and (2) lines are S21.

The measurements of S-parameters by network analyzer are shown in figure 6-6 and the results show that both of slow wave electrode structures for the variable and uniform coupling case have similar properties. The effective refractive index and characteristic impedance calculated using measured S-parameters are shown in figure 6-7 and 6-8 for the uniform coupling with phase shifts and variable coupling cases, respectively.

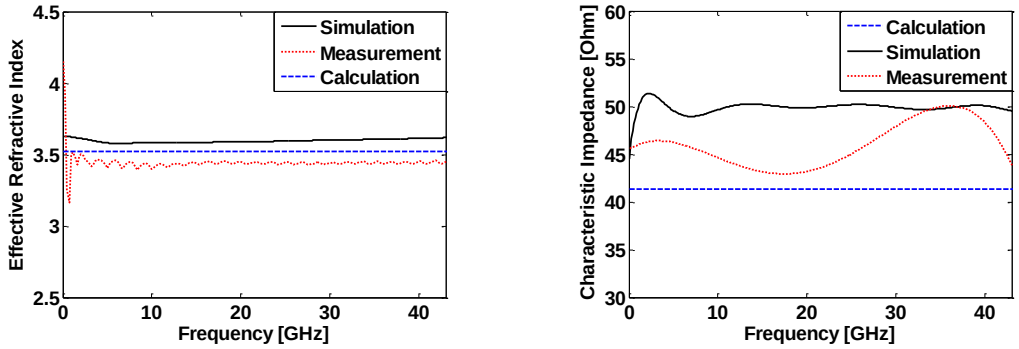

(a) (b)

Figure 6-7: (a) Three lines of the calculation, simulation, and measurement for the effective refractive index of the slow wave electrode structure and (b) three lines of the calculation, simulation, and measurement for the characteristic impedance of the slow wave electrode structure for the uniform coupling with phase shifts case.

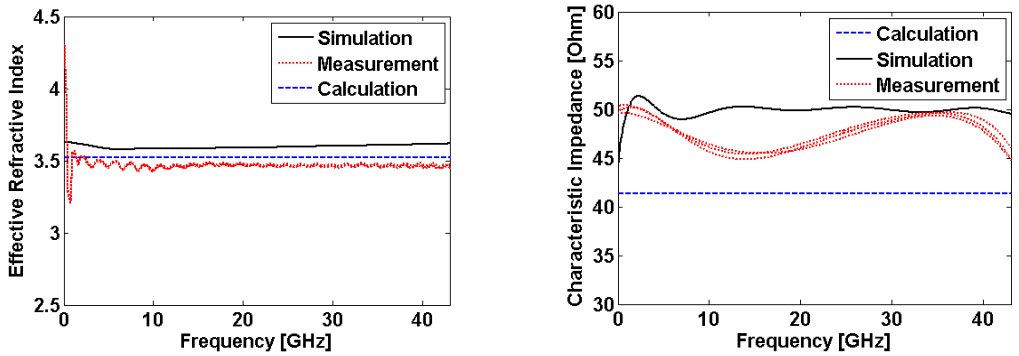

(a) (b)

Figure 6-8: (a) Three lines of the calculation, simulation, and measurement for the effective refractive index of the slow wave electrode structure and (b) three lines of the calculation, simulation, and measurement for the characteristic impedance of the slow wave electrode structure for the variable coupling case.

From figure 6-7 and 6-8, the effective refractive indices are about 3.47, which is well matched with the refractive index of GaAs which is 3.59. The characteristic impedances are about 46 Ω. The agreement of the impedance with simulation and calculation shows about ±8%. This error may be due to the neglect of junction and other parasitics in calculation. The difference between the simulation and the measurement results may also be due to the dimensional size error of the transmission line during the fabrication.

6.2.2 DC Measurement

The schematic diagram of the experiment setting for the DC measurement is shown in figure 6-9 and the photographs of the setting is shown in figure 6-10. For the light source a laser diode MLD1300-50S9P which is made by MeshTel and has maximum 50mW output is used. However, coupled power at the end of the input fiber to the modulator is much less than 10mW because the coupling is performed with lenses after a polarizer as shown in figure 6-9.

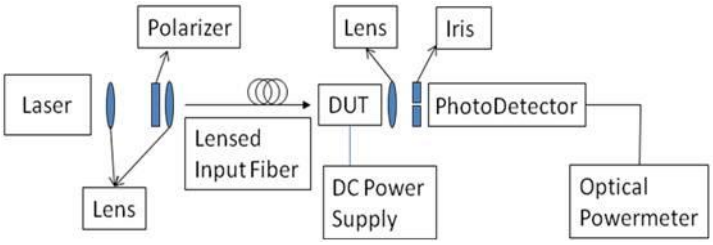

Figure 6-9: Schematic diagram of the DC measurement of the modulator.

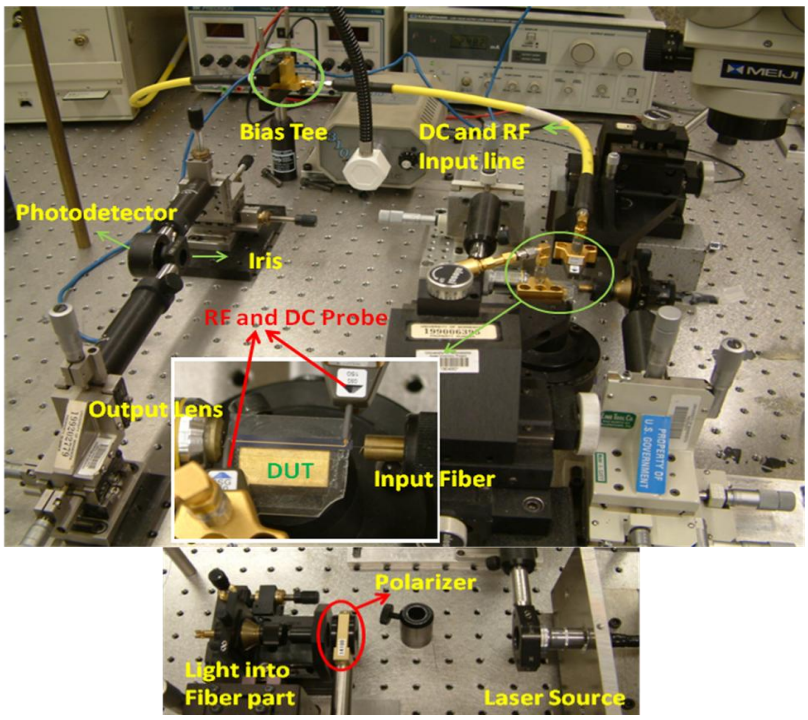

Figure 6-10: DC measurement setting with light source.

Light from the laser is focused by a lens which is located immediately after the laser and passes through the polarizer to obtain the correct polarization. The polarized light is coupled to a polarization maintaining fiber by a second lens and coupled to the input waveguide of the optical modulator through the lensed tip of the input fiber. The working distance of the lensed tip is 6±2μm and the spot diameter is 2.5±0.7μm. The output from the modulator gathered by a lens shows two bright spots shown in figure 6-11 (a), which represent modes of input and output waveguides. To obtain these pictures, a IR camera and monitor used. The spot on the left and the large spot on the right in figure 6-11 (a) are from the input waveguide and output waveguide, respectively. These two spots are due to the incorrect coupling length which is caused by uneven etching during the waveguide fabrication.

To measure the intensity response of the modulator, the output from the input waveguide should be blocked which is performed by an iris in front of the photodetector shown in figure 6-10 (a). The result is shown in figure 6-11 (b).

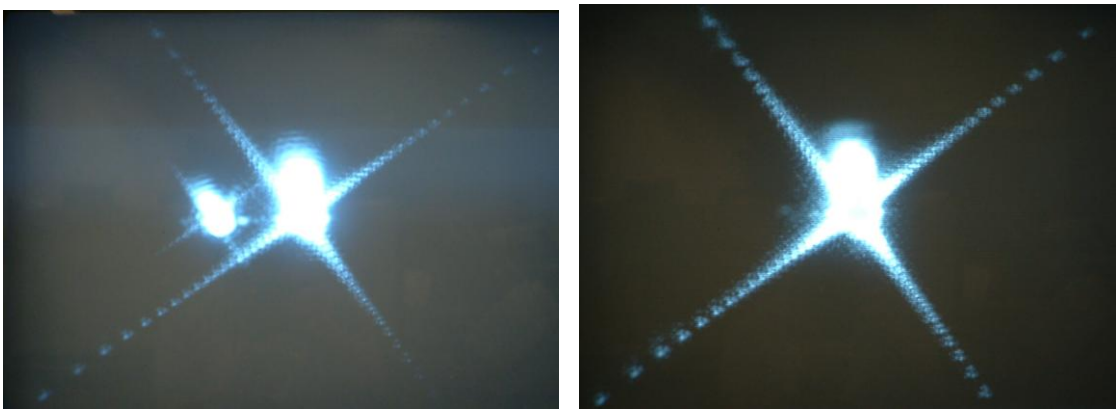

(a) (b)

Figure 6-11: (a) Two spots represents the mode of input and output waveguides and (b) Output, with the input guide blocked using an iris.

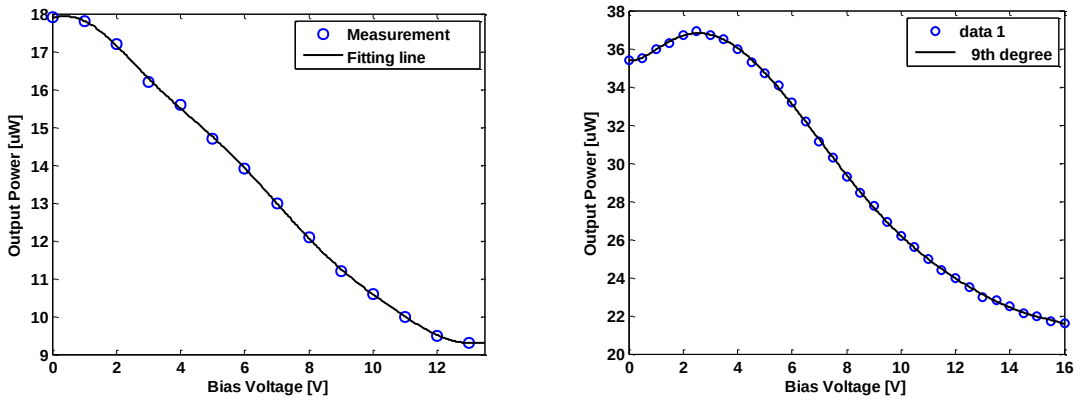

(a) (b)

Figure 6-12: The intensity responses of the directional coupler modulators.

The intensity response which is shown in figure 6-12 is measured by the photodetecter with an optical powermeter. Two measurements were performed for the uniform coupling with phase shifts and variable coupling directional coupler modulator. The results show that the switching voltage for the uniform coupling with phase shifts and variable coupling modulators are around 14V, which are higher than the calculation result shown in table IV in Chapter 3, and the attribute bias to the difference is due to the uneven etching of the waveguides. The figure 6-12 shows good linearity in the slope region, however, the optical loss of the modulator is high. The measured maximum optical intensity at the end of the output waveguide of the modulator is shown in figure 6-12 (b), is approximately 35.4 μW with lens and photodetector and 11.5 μW with lensed fiber and photodetector at $0V$ of bias voltage. The output power is low because the coupling losses at the input and output are high. The total loss from the input end to output end of the modulator is about 23.5dBm which includes input and output coupling loss, and the propagation loss in the modulator. This high loss may come from uneven

etch of the waveguides, and the roughness of cut facets at the input and output of the modulator due to the manual thinning by hand.

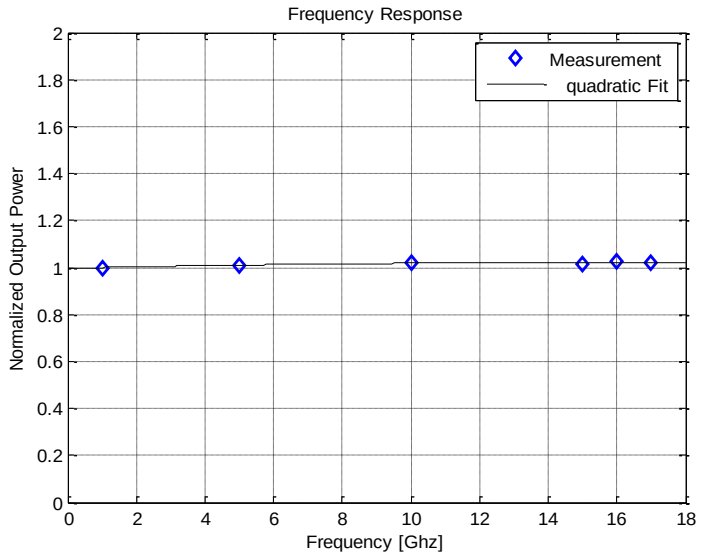

Figure 6-13: The frequency response of the uniform coupling with phase shifts modulator.

The measurement of the frequency response is also performed using signal generator which covers till 20 GHz. The result shows almost flat response shown in figure 6-13 which means that the slow-wave electrode structure works well. However, the measurement was not performed beyond 18GHz because of the limitation of the frequency range of the signal generator and the low output power of the modulator.

The measurement of the modulation is performed with two-tone test by using two signal generators, a custom built Wilkinson combiner, a bias tee, RF probes, DC blocked connector, 50Ω termination, output lensed fiber, a receiver, a low noise amplifier, and a RF spectrum analyzer. The schematic diagram of the modulation test is shown in figure 6-14. Figure 6-15 is a photograph of the measurement setting of the modulation test. The photodetector and iris are removed and the output lens is replaced with output lensed

fiber. For the two-tone modulation test, two signal generators shown in figure 6-16 (a) are used. These two signals are combined by the wilkinson combiner shown in figure 6-16 (b) which has a loss of 0.5dB. The RF output signal from the combiner goes into a bias tee to add DC bias voltage to the modulator which is shown in figure 6-15.

DC bias voltage and RF signal are applied on the input pad of the slow wave electrode of the modulator through the RF Ground-Signal-Ground (GSG) probe. To prevent the reflection at the output end of the electrode, a 50Ω termination is connected with a DC block as shown in figure 6-15. The modulated optical signal by two RF signals comes out from the modulator output waveguide in coupled into the output lensed fiber. This output lensed fiber is connected to the receiver which is a photodiode and the output of the receiver is connected to the low noise amplifier, which are shown in figure 6-17 (a) and (b). The amplified RF signal is detected by the spectrum analyzer shown in figure 6-18.

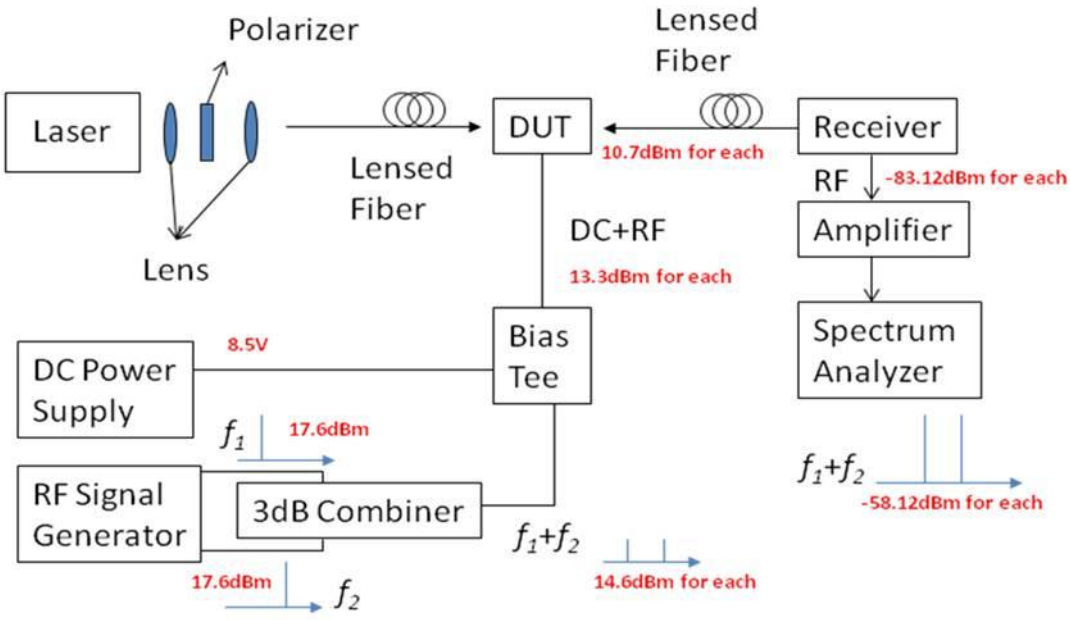

Figure 6-14: The schematic diagram of the modulation and two-tone test.

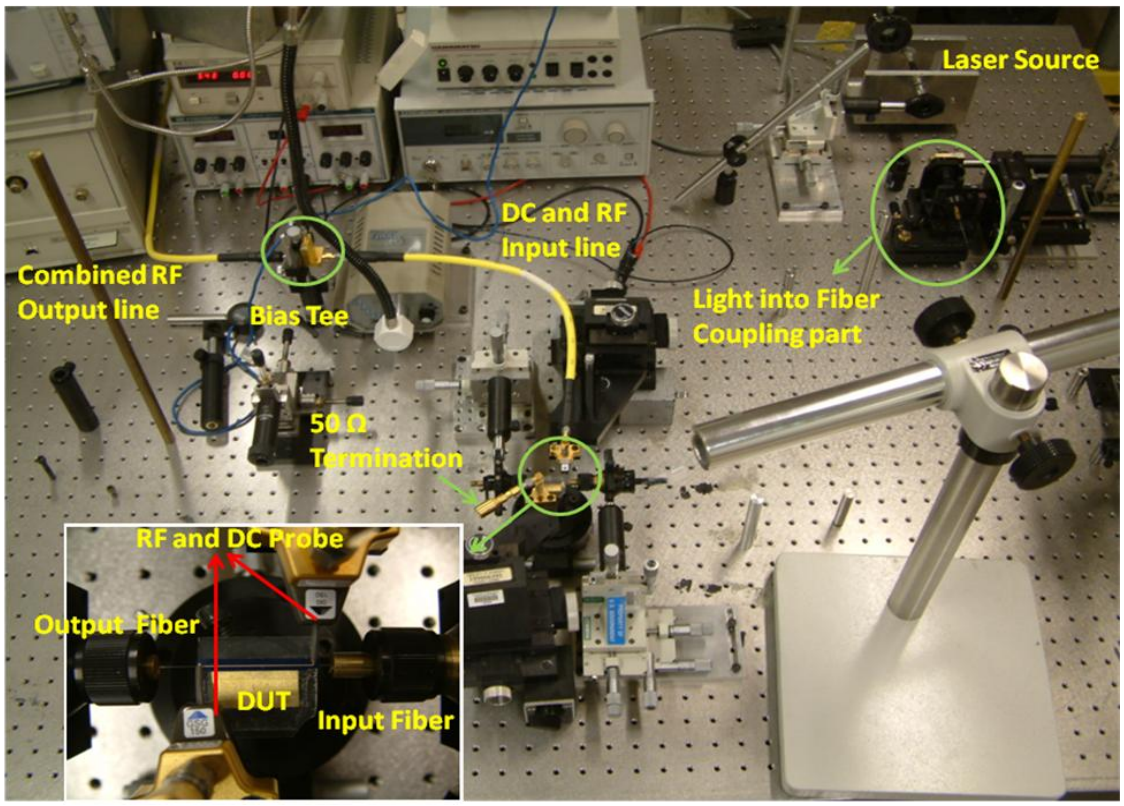

Figure 6-15: Measurement setting for the Modulation test .

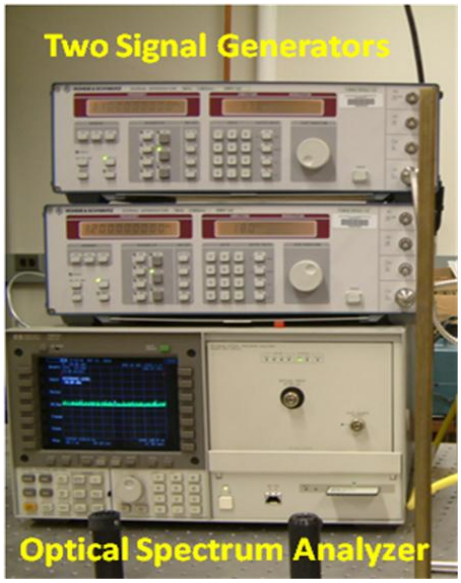

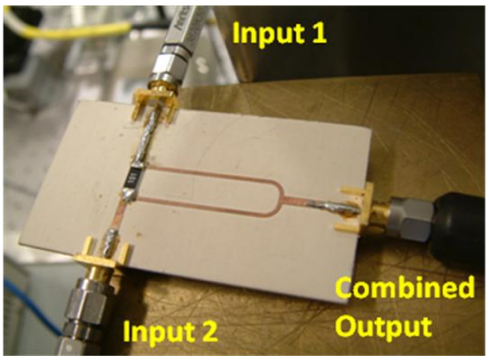

(a) (b)

Figure 6-16: (a) Two signal generator and optical spectrum analyzer, (b) 3dB power combiner.

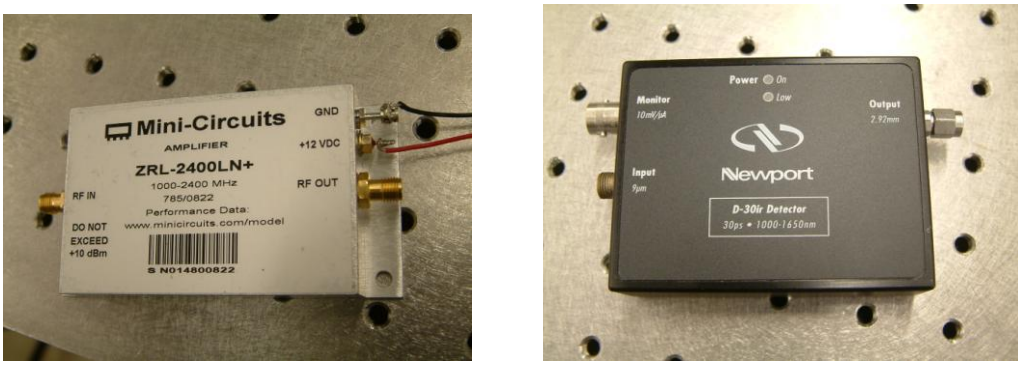

(a) (d)

Figure 6-17: (a) ZRL-2400LN+ LNA and (b) D-30ir Detector receiver.

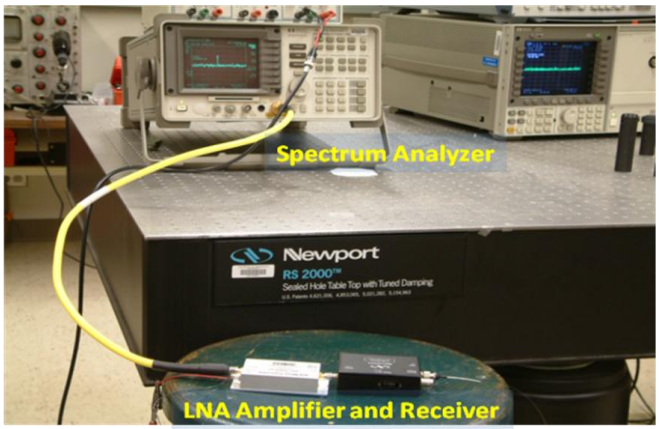

Figure 6-18: RF spectrum analyzer and the connection with LNA and Receiver.

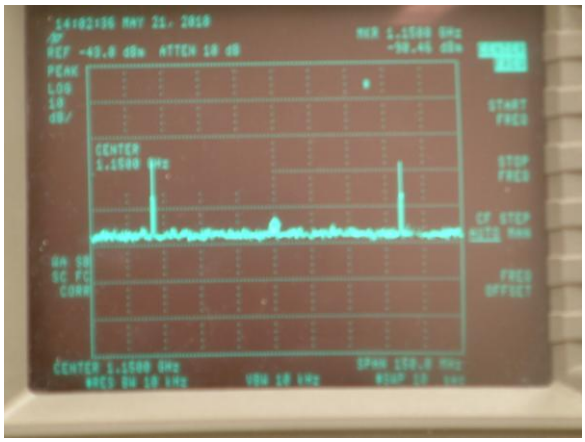

Figure 6-19: The measured two-tone modulated signal.

The output measured by spectrum analyzer is shown in figure 6-19, and it shows two peaks at the frequencies of modulation signals. Although the directional coupler modulator works successfully, the modulated optical output power level is too low to evaluate the linearity of the modulator response, and obtain its SFDR and its harmonic response.

When the DC bias voltage is 8.5V and RF input power is 17.1dBm the output power is -58.12dBm. The calculation of the output power is performed to compare with the measurement result. The gain is calculated using equation (2.128) written as

$$g_{Total} = \left\{ P_L (1 - L_o) r_D R^2 \left| \frac{\partial T}{\partial V} \right|_{V_{bias}} \right\}^2 . \tag{6.2}$$

The optical output power, $P_L(1-L_o)$, from the modulator output waveguide is 11.5μW, the responsivity of the receiver is 0.8A/W, R is 50Ω, and a slop efficiency, $|\partial T/\partial V|$, at the applied DC bias is 0.044 for the response function shown figure 6-12 (b).

When all parameters are substituted in equation (6.2), the total link gain is

$$g_{Total} = 4.09658 \times 10^{-10} . \tag{6.3}$$

Therefore, the RF output power after the amplifier is

$$P_{out} = 10\log(g_{Total}) + P_{in} + G_{amplifier} . \tag{6.4}$$

where $G_{amplifier}$ is the gain of amplifier which is about 25dBm. The RF output power at the load of the modulator's electrode is 10.7dBm shown in figure 6-14 which is correspond to the input RF power, P_{in}. Therefore, the calculated total output power is -58.17dBm which is well matched with measured result.

CHAPTER 7 Conclusion and Future Work

7.1 Conclusion

Variable coupling along the length of an optical directional coupler modulator is used to obtain linear intensity response and for a desired response function the coupling function can be synthesized. This synthesis gives rise to negative coupling function sections realized by placing a π phase shift in one of the arms of the coupler, and the reversion to the positive coupling requires a second π phase shift again in one of the arms. A second design of an uniform coupler with four π phase shifts was considered to obtain linear response.

These two linear designs have been investigated, fabricated, and measured. The trapezoidal response design was synthesized by the Fourier transform and refined using the Newton's method. The uniform coupler with phase shift design was achieved by four phase shift points, which were chosen very carefully for linear response. The small signal calculations for the second and third order intermodulation distortions (IMD2 and IMD3) show Spur Free Dynamic Ranges(SFDR) of the better than 120 $dB/Hz^{2/3}$ in 1 Hz bandwidth for the IMD3 for both designs, and the IMD2 of the order of 105 $dB/Hz^{1/2}$ for the trapezoidal response and better than 120 $dB/Hz^{1/2}$ for the phase shift design. The switching voltage–length product of the trapezoidal response is lower than the phase shift design.

Since the electrical phase velocity in III-V semiconductor coplanar strip electrode structures is larger than the optical phase velocity, a slow-wave electrode structure is required for velocity-match of the optical and RF velocities, and the coplanar strip with series inductive and shunt capacitive loads was designed and tested.

The fabrication of the optical coupler modulator was complicated because of the etching equipment limitation, electroplating with narrow gap electrodes, and the manual thinning.

The velocity matched design works well because the electrode frequency response shows almost a flat response up to 20Ghz, which is limited by test equipment. The modulation test is also successful and the measured output power is well matched with the calculation value. However, the intensity responses of the coupler modulator designs are different from the design values because of uneven waveguide etching. The coupling length does not match with the calculated value because uneven etching changed the coupling length. In addition, this uneven etching condition makes asymmetric coupler waveguides which causes incomplete power transfer in the coupler and changed the switching voltage. The output power level is too low to measure the harmonics and intermodulation distortion powers and to estimate the linearity.

7.2 Future Work

As was mentioned in the previous section, there are several difficulties in fabricating and testing the linear optical directional coupler modulator.

The one major problem in the fabrication is uneven waveguide etching. To overcome this, diffused channel waveguides may be used. If channel waveguides are used the etching process is not needed, and then there is no uneven etching problem.

The measurement problems are low optical intensity level of the output from the optical modulator and high coupling loss from laser source to fiber, fiber to modulator input, and modulator output to fiber. For the low level intensity problem, high power

laser source which has over 100mW should be used because high power laser source increases the optical output level. The laser source which has a fiber connector is favored because the connector removes the free-space coupling loss from laser source to fiber. For the coupling loss problem between modulator and fiber, the tapered waveguide input and output may be used to reduce the coupling losses. To obtain clean cut facets at the input and output end of the waveguides reduce the coupling loss as well.

Another measurement problem is low value of S_{21} for the fabricated slow wave electrode structure. This problem may be caused by the input and output pad design of the electrode structure for the RF probes. Although the coplanar stripline is used for the electrode structure which commonly uses ground-signal (GS) probes, the probe pads are designed for the ground-signal-ground (GSG) probes which are used for the coplanar waveguides. Therefore, this GSG probes generate extra parasitic components, and they causes the transmission loss. To improve RF measurement results, input and output pad designs are modified for using GS probes.

In this thesis, only the optical modulator is discussed. However, since the modulator is on a semiconductor substrate, integration with other components including lasers, FET/HBT circuits may also be possible, and needs investigation.

In addition, phase modulation in the directional coupler modulator needs to be investigated by examining the phase of the RF excitation of the electrodes on the two arms of the coupler. Success here would lead to applications in other modulator formats including digital PSK, QPSK, DPSK, and QAM, and extend the reach of the coupler modulator.

CHAPTER 8 References

[1-1] K. Kishino, S. Aoki, and Y. Suematsu, "Wavelength variation of 1.6 μm wavelength buried heterostructure GaInAdP/InP lasers due to direct modulation," IEEE J. of Quantum Electronics, vol. QE-18, pp. 343-351, 1982

[1-2] M. Suzuki, H. Tanaka, and S. Akiba, "Effect of hole pile-up at heterointerface on modulation voltage in GaInAsP electroabsorption modulators," Electronics letter, vol.25, no. 2, pp. 88-89, Jan 1989

[1-3] E. I. Ackerman and C. H. Cox, "RF Fiber-Optic Link Performance," *IEEE Microwave Magazine*, vol. 2, pp. 50-58, Dec. 2001.

[1-4] W. B. Bridges and J. H. Schaffner, "Distortion in Linearized Electrooptic Modulators," *IEEE Transactions on Microwave Theory and Techniques*, vol. 43, pp. 2184-2197, Sept. 1995.

[1-5] E. L. Wooten et al, "A Review of Lithium Niobate Modulators for Fiber-Optic Communications Systems," *IEEE Journal of Selected Topics in Quantum Electronics*, vol. 2, pp. 69-82, Jan./Feb. 2000.

[1-6] R. Spickermann and N. Dagli, "Experimental Analysis of Millimeter wave coplanar waveguide slow wave structure on GaAs," IEEE Trans. On Microwave Theory and Techniques, vol. 42, no. 10, pp. 1918-1924, Oct. 1994

[1-7] R. Spickermann, N. Dagli, and M.G. Peters, "GaAs/AlGaAs electrooptic modulator with bandwidth > 40 GHz," Electronics Letters, vol. 31, no. II, pp. 915-916, May 1995

[1-8] N. Dagli, R. Spickermann, S. Sakamoto, and M. Peters, "Ultra wide bandwidth GaAs/AlGaAs electrooptic modulators," 1995 IEEE International Microwave Symposium Digest, pp 251-254, 1995

[1-9] J. C. Cartledge and V. Bouder, "Measurement of alpha-parameter for push-pull operation of π phase shift MQW Mach-Zehnder modulator," Electronics Letters, vol. 37, no. 7, pp. 452-444, May 2001

[1-10] N. Miyazaki, K. Ooizumi, T. Hara, M. Yamada, H. Nagata, T. Sakane, "LiNbO3 optical intensity modulator packaged with monitor photodiode," IEEE photonics Technology Letters, vol. 13, no. 5, pp. 442-444, May 2001

[1-11] B. Enning, "Simple approach to the simulation of the polarization dependence of a LiNbo3 Mach-Zehnder modulator," Journal of Optical Communications, vol.21, no. 5, pp. 162-164, Oct 2000

[1-12] Y. H. Min, J. Mun, C.S. Yoo, K. H. Kim, K. S. Lee, "Mach-Zehnder eletro-optic modulator based on organic-silica sol-gel hybrid films," Electronics Letters, vol. 35, no. 20, pp. 1770-1771, 1999

[1-13] L. M. Johnson and H. V. Roussell, "Reduction of Intermodulation Distortion in Interferometric Optical Modulators," *Optics Letters*, vol. 13, pp. 928-930, 1998.

[1-14] P.-L. Liu, J. Li and Y. S. Trisno, "In Search of a Linear Electrooptic Amplitude Modulator," *IEEE Photonics Technology Letters*, vol. 3pp. 144-146, Feb. 1991.

[1-15] A. Djupsjobacka, "A Linearization Concept for Integrated-Optic Modulators," *IEEE Photonics Technology Letters*, vol. 9, pp. 869-879, Aug. 1992.

[1-16] J. H. Schaffner and W. B. Bridges, " Intermodulation Distortion in High Dynamic Range Microwave Fiber-Optic Links with Linearized Modulators," *IEEE Journal of Lightwave Technology*, vol. 11, pp. 3-6, Jan. 1993.

[1-17] M. L. Farwell, W. S. C. Chang and D. R. Huber, "Increased Linear Dynamic Range by Low-Biasing the Mach-Zehnder Modulator," *IEEE Photonics Technology Letters*, vol. 5, pp. 779-782, July 1993.

[1-18] G. E. Betts, "Linearized Modulator for Suboctave-Bandpass Optical Links," *IEEE Transactions on Microwave Theory and Techniques*, vol. 42, pp. 2642-2649, Dec. 1994.

[1-19] W. K. Burns, "Linearized Optical Modulator with Fifth-Order Correction," *IEEE Journal of Lightwave Technology*, vol. 13, pp. 1724-1727, Aug. 1995.

[1-20] C. Laliew et al, "A Linearized Optical Directional Coupler Modulator at 1.3 μm," *IEEE Journal of Lightwave Technology*, vol. 18, pp. 1244-9, Sept. 2000.

[1-21] M. L. Farwell et al, "An Electrooptic Intensity Modulator with Improved Linearity," *IEEE Photonics Technology Letters*, vol. 3, pp. 792-795, Sept. 1991.

[1-22] R. F. Tavlykaev and R. F. Ramaswamay, "Highly Linear Y-Fed Directional Coupler Modulator with Low Intermodulation Distortion," *IEEE Journal of Lightwave Technology*, vol. 17, pp. 282-291, Feb. 1999.

[1.23] S. A. Hamilton et al, "Comparison of an In-Line Asymmetric Directional Coupler Modulator with Distributed Optical Loss to Other Linearized Electrooptic Modulators," *IEEE Transactions on Microwave Theory and Techniques*, vol. 47, pp. 1184-1193, July 1999.

[1-24] C. Laliew, K. H. Baek and A. Gopinath, “A synthesized electrooptic directional-coupler modulator at 1.3 μm with low switching voltage,” *2002 Conference on Lasers and Electro-Optics Technical Digest*, pp. 42, May 2002.

[1-25] A. Gorur, G. Karpus, and M. Alkan, "Characteristics of periodically loaded CPW structure," *IEEE Microwave Guided Wave Lett,* vol. 8, pp. 278-280, Aug. 1998

[1-26] J. Sor, Y. Oian, and T. Itoh, "Miniature low-loss CPW periodic structures for filter applications," *IEEE Trans. Microwave Theory Tech*, vol. 49, pp. 2336-2341, Dec. 2001

[1-27] Xu Feng, Li Lin, Wu Ke, S. Deoprat, M. Chaker, "Application of FDFD Algorithm Combined with Shift-and-Invert Arnoldi Technique in Bilateral Interdigital Coplanar Waveguide Slow wave Structure," *IEEE MTT-S Int.* 11-16, pp.1025-1028, June, 2006

[1-28] E.H. Bottcher, H. Pfitzenmaier, E Droge and D Bimberg, "Millimetre-wave coplanar waveguide slow wave transmission lines on InP,*" Electron. Lett.*, Vol.32, No.15, pp1377-1378, July 1996

[1-29] Lei Zhu, "Guided-Wave Characteristics of Periodic Coplanar Waveguides With Inductive Loading-Unit-length Transmission Parameters," *IEEE Trans. Microwave Theory & Tech.,* Vol. 51, pp. 2133-2138, Oct.2003

[1-30] Nicolas A.F. Jaeger, Farnoosh Rahmatian, Hiroshi Kato, Robert James, Ezio Berolo, and Zachary K.F. Lee, "Velocity-Matched Electrodes for Compound Semiconductor Traveling-Wave Electrooptic Modulators: Experimental Results," *IEEE Microwave Guided Wave Lett.*, vol. 6, pp. 82-84, Feb.1996

[2-1] A. Yariv, *Optical Electronics in Modern Communications, 5th Ed.* New York: Oxford, 1977.

[2-2] S.L. Chuang, Physics of Optoelectronic Devices, Wiley-Interscience Publication, New York, 1995

[2-3] S. Y. Wang and S.H. Shin, "High-speed III-V electrooptic waveguide modulators at 1.3 μm," Journal of lightwave Tech., vol. 6, no. 6, pp. 78-771, 1988

[2-4] R. C. Alferness, "Waveguide electrooptic modulators," IEEE Trans. On Microwave Theory and Tech., vol. MTT-30, no. 8, pp. 1121-1137, August 1982

[2-5] K. Cheng, Fiber and Electro-optical Components, Handbook of Microwave and Optical Components, vol. 4, Wiley-Interscience, 1991

[2-6] Polloc, Fundamentals of Optoelectronics, Irwin, 1995

[2-7] C. Laliew et al, "A Linearized Optical Directional Coupler Modulator at 1.3 μm," *IEEE Journal of Lightwave Technology*, vol. 18, pp. 1244-9, Sept. 2000.

[2-8] G. M. Kizer, *Microwave Communication*, Ames, IA: Iowa State University Press, 1990

[2-9] William H. Press, Saul A. Teukolsky, William T. Vetterling, and Brian P. Flannery, Numerical recipes in FORTRAN, 2nd, Cambridge, 1992

[2-10] B. P. Lathi, Linear System and Signals, 2nd, Oxford university press, 2004

[2-11] G. E. Betts et al, "On the Linear Dynamic Range of Integrated Electrooptical Modulators," *IEEE J. Quantum Electronics*, vol. QE-22, pp. 1009-1011, July 1986.

[2-12] Charles H. Cox, III, Analog Optical Links Theory and Practice, Cambridge, 2009

[2-13] Scott A. Hamilton, Diego R. Yankelevich, Andr´e Knoesen, Robert T. Weverka, and Richard A. Hill, " Comparison of an In-Line Asymmetric Directional Coupler Modulator with Distributed Optical Loss to Other Linearized Electrooptic Modulators," IEEE Transaction on Microwave Theory and Tech., vol. 47, no. 7, July 1999

[2-14] G. P. Agrawal, Fiber-*Optic Communication Systems, 2nd edition*. New York: Wiley, 1997.

[3-1] C. Laliew, S. W. Lovseth, X. Zhang, and A. Gopinath, "A Linearized Optical Directional Coupler Modulator at 1.3 μm," *IEEE J. Lightwave Technology*, vol. 18, pp. 1244-9, September 2000.

[3-2] G. H. Song and S. Y. Shin, "Design of corrugated waveguide filters by the Gel'fand-Levitan-Marchenko inverse- scattering method," J. Opt. Soc. Am. A, vol. 2, no. 11, pp. 1905-1915, November 1985.

[3-3] R. C. Alferness, "Titanium-diffused lithium niobate waveguide devices," in *Guided-Wave Optoelectronics*, 2nd ed, T. Tamir, Ed. New York: Springer-Verlag, 1990, pp. 145–206.

[3-4] K. A.Winick, "Design of corrugated waveguide filters by Fourier transform techniques," *IEEE J. Quantum Electron.*, vol. 26, pp. 1918–1929,Nov. 1990.

[3-5] R. C. Alferness and P. S. Cross, "Filter characteristics of codirectionally coupled waveguides with weighted coupling," *IEEE J. Quantum Electron.*, vol. QE-14, pp. 843–847, Nov. 1978.

[3-6] M. G. Cohen and E. I. Gordon, "Acoustic beam probing using optical techniques," *Bell Syst. Tech. J.*, vol. 44, no. 4, pp. 693–721, Apr. 1965.

[3-7] Lagarias, J.C. et al, "Convergence Properties of the Nelder-Mead Simplex Method in Low Dimensions," *SIAM Journal of Optimization*, vol. 9, pp. 112-147, 1998.

[3-8] L. W. Couch, II, Digital and Analog Communication Systems, New York: Macmillan, 1993.

[3-9] T. Li, C. Laliew and A. Gopinath, "An iterative transfer matrix inverse scattering technique for synthesis of codirectional optical coupler and filters," *IEEE J. of Quantum*

Electronics, vol. 38, no. 4, pp. 375-379, April 2002.

[3-10] K. Baek, C. Laliew and A. Gopinath, " The wavelength dependence of a synthesized electro-optic co-directionalcoupler modulator with π-phase shifters," *2002 Integrated Photonics Research Technical Digest*, pp. IThD3, July 2002.

[3-11] L. A. Coldren and S. W. Corzine, *Diode Lasers and Photonic Integrated Circuits*, New York: Wiley, 1995.

[3-12] G. M. Kizer, *Microwave Communication*, Ames, IA: Iowa State University Press, 1990.

[3-13] R. C. Alferness, "Waveguide Electrooptic Modulators," *IEEE Trans. Microwave Theory Tech.*, vol. TMM-30, pp. 1121-1137, August 1982.

[3-14] W. B. Bridges and J. H. Schaffner, "Distortion in Linearized Electrooptic Modulators," *IEEE Trans. Microwave Theory Tech.*, vol. 43, pp. 2184-2197, Sept. 1995.

[3-15] S. A. Hamilton et al, "Comparison of an In-Line Asymmetric Directional Coupler Modulator with Distributed Optical Loss to Other Linearized Electrooptic

Modulators,” *IEEE Trans. Microwave Theory Tech*., vol. 47, pp. 1184-1193, July 1999.

[4-1] R. Spickermann, N. Dagli, "Experimental analysis of millimeter wave coplanar waveguide slow wave structures on GaAs," *IEEE Trans. Microwave Theory & Tech.,* Vol. 42, pp. 1918-1924, Oct. 1994

[4-2] A. Gorur, G. Karpus, and M. Alkan, "Characteristics of periodically loaded CPW structure," *IEEE Microwave Guided Wave Lett*, vol. 8, pp. 278-280, Aug. 1998

[4-3] J. Sor, Y. Oian, and T. Itoh, "Miniature low-loss CPW periodic structures for filter applications," *IEEE Trans. Microwave Theory Tech*, vol. 49, pp. 2336-2341, Dec. 2001

[4-4] Xu Feng, Li Lin, Wu Ke, S. Deoprat, M. Chaker, "Application of FDFD Algorithm Combined with Shift-and-Invert Arnoldi Technique in Bilateral Interdigital Coplanar Waveguide Slow wave Structure," *IEEE MTT-S Int. Micro. Symp. Dig.* 11-16, pp.1025-1028, June, 2006

[4-5] E.H. Bottcher, H. Pfitzenmaier, E Droge and D Bimberg, "Millimetre-wave coplanar waveguide slow wave transmission lines on InP*," Electron. Lett.*, Vol.32, No.15, pp1377-1378, July 1996

[4-6] Lei Zhu, "Guided-Wave Characteristics of Periodic Coplanar Waveguides With Inductive Loading-Unit-length Transmission Parameters," *IEEE Trans. Microwave Theory & Tech.,* Vol. 51, pp. 2133-2138, Oct.2003

[4-7] Nicolas A.F. Jaeger, Farnoosh Rahmatian, Hiroshi Kato, Robert James, Ezio Berolo, and Zachary K.F. Lee, "Velocity-Matched Electrodes for Compound

Semiconductor Traveling-Wave Electrooptic Modulators: Experimental Results," *IEEE Microwave Guided Wave Lett.*, vol. 6, pp. 82-84, Feb.1996

[4-8] David, M, Pozar, *Microwave and Rf Desing of Wireless Systems*, John Wiley & Sons Inc, pp. 174-175, Nov. 2000

[4-9] David, M, Pozar, *Microwave and Rf Desing of Wireless Systems*, John Wiley & Sons Inc, pp. 211, Nov. 2000